Improving Selectivity in Electrochemical CO_2-to-Fuels Catalysis: the Role of Catalyst Mesostructure, Surface Structure, and Electrolyte

by

Youngmin Yoon

B.A. Chemistry
University of Pennsylvania, 2011

SUBMITTED TO THE DEPARTMENT OF CHEMISTRY IN PARTIAL FULFILLMENT OF THE REQUIREMENTS FOR THE DEGREE OF

DOCTOR OF PHILOSOPHY IN INORGANIC CHEMISTRY

AT THE

MASSACHUSETTS INSTITUTE OF TECHNOLOGY

JUNE 2018

Signature of Author: Signature redacted

Department of Chemistry
April 09, 2018

Certified by: Signature redacted

Yogesh Surendranath
Paul M. Cook Career Development Assistant Professor of Chemistry
Thesis Supervisor

Accepted by: Signature redacted

Robert W. Field
Haslam and Dewey Professor of Chemistry
Chairman, Departmental Committee for Graduate Students

This doctoral thesis has been examined by a committee of the Department of Chemistry as follows:

Signature redacted

Mircea Dincă
Associate Professor of Chemistry
Committee Chairman

Signature redacted

Yogesh Surendranath
Paul M. Cook Career Development Assistant Professor of Chemistry
Thesis Supervisor

Signature redacted

Daniel G. Nocera
Patterson Rockwood Professor of Energy, Harvard University

To my Family and Friends

Improving Selectivity in Electrochemical CO_2-to-Fuels Catalysis: the Role of Catalyst Mesostructure, Surface Structure, and Electrolyte

by

Youngmin Yoon

Submitted to the Department of Chemistry
on May 11, 2018 in Partial Fulfillment of the
Requirements for the Degree of Doctor of Philosophy in
Inorganic Chemistry

ABSTRACT

Mitigating atmospheric CO_2 levels is an important challenge in curbing anthropogenic climate change. To this end, the storage of intermittently generated renewable energy in the chemical bonds of electro-reduced CO_2 is considered an attractive carbon-neutral route to storing CO_2. However, the selectivity of this reaction, particularly in aqueous electrolytes, remains open to improvement due to both the generation of large quantities of H_2 from solvent reduction and the multitude of CO_2 reduction products. This thesis will discuss strategies to improve product selectivity.

The first section of this thesis focuses on methods to measure a basic property of electrocatalysts that enables studies on the origin of catalyst activity and that allow for systematic comparisons of catalyst activity: the electrochemical surface area. Using double layer capacitance measurements in aprotic electrolytes and atomic force microscopy to independently determine surface areas, it is possible to obtain a general value of specific capacitance (~11 μF/real cm^2) across multiple materials relevant for electrochemical catalysis by minimizing strong ion interactions with the electrode surface.

The knowledge of electrode surface areas and the kinetics of CO_2 vs H^+ activation during CO_2 electroreduction enables the discovery that electrode mesostructure can have significant impacts on CO_2 reduction selectivity. As the electrode structure becomes rougher, diffusion gradients of the HCO_3^- proton donor formed at the double layer suppresses H_2 evolution activity. On both Au and Ag electrodes, this leads to a suppression of H_2 evolution, while CO_2 reduction current density is enhanced on Ag electrodes on a surface area normalized basis.

The last part of this thesis focuses on exploring the kinetics of CO intermediates that gate hydrocarbon selectivity on Cu electrodes. The data indicate a Langmuir-Hinshelwood type mechanism in play for both the production of CH_4 and C_2H_4, whereby surface adsorbed CO_{ads} react with other surface adsorbed species in a rate limiting fashion. Using this insight, pulsed electrodeposition in an aqueous citrate electrolyte is used to make nanocrystalline Cu electrocatalysts with a high density of grain boundary sites, which have been suggested to have strong CO affinity, and can thus suppress CH_4 and H_2 formation.

Thesis Supervisor: Yogesh Surendranath

Title: Paul M. Cook Career Development Assistant Professor of Chemistry

Table of Contents

List of Figures

List of Tables

List of Abbreviations and Symbols

AFM	Atomic Force Microscopy
CA	Chronoamperometry
CCS	Carbon Capture and Storage
CCU	Carbon Capture and Utilization
CP	Chronopotentiometry
CV	Cyclic Voltammetry
DLC	Double Layer Capacitance
ECSA	Electrochemical Surface Area
η	Overpotential
FCC	Face Centered Cubic
FE	Faradaic Efficiency
FTO	F-doped Tin Oxide
GC	Gas Chromatograph
HER	Hydrogen Evolution Reaction
IO	Inverse Opal
OCP	Open Circuit Potential
OD	Oxide-Derived
OER	Oxygen Evolution Reaction
PED	Pulsed Electrodeposition
PZC	Potential of Zero Charge
RHE	Reversible Hydrogen Electrode
RF	Roughness Factor
SEM	Scanning Electron Microscopy
UPD	Underpotential Deposition
XPS	X-Ray Photoelectron Spectroscopy
XRD	X-Ray Diffraction

Chapter 1 – Introduction

This chapter contains text from the following articles:

(1) Yoon, Y.; Hall, A. S.; Surendranath, Y. Tuning of Silver Catalyst Mesostructure Promotes Selective Carbon Dioxide Conversion into Fuels. Angew. Chemie Int. Ed. **2016**, 55 (49), 15282.

(2) Wuttig, A.; Yoon, Y.; Ryu, J.; Surendranath, Y. Bicarbonate Is Not a General Acid in Au-Catalyzed CO_2 Electroreduction. J. Am. Chem. Soc. **2017**, 139 (47), 17109.

Publication contribution notes:

In the paper, "Bicarbonate Is Not a General Acid in Au-Catalyzed CO_2 Electroreduction", the author contributed to the electrochemical measurements regarding the irreversible binding of CO on Au, to the discussion on kinetics pathways, and to the diffusion modeling.

1.1 CO_2 storage and mitigation

With rising greenhouse gas emissions leading to unprecedented levels of CO_2 levels in the atmosphere, there is a large body of evidence for anthropogenic climate change, which will have significant disrupting global impact with humanitarian, geopolitical, and economic ramifications that we may not fully predict.[1–5] This has led to a large effort from governments, industries, and academia to explore alternative routes to energy generation, storage, and industrial processing that aim to be carbon-neutral or even carbon-negative in their footprints.

While electricity generation can largely be replaced with renewable and carbon neutral energy sources such as wind, solar, hydro, and nuclear, there remain numerous challenges impeding full conversion. For key intermittent energy sources such as wind and solar, challenges include overcoming the electrical grid instability and the lack of efficient energy storage,[6,7] which do not hamper combustion based energy generation. Additionally,

geographical and political challenges can impede the deployment of carbon-neutral energy generation.[7] Beyond the energy sector, the transportation sector generates a large fraction of CO_2 as well from combustion engines, while CO_2 is a common byproduct in industrial processing, demonstrating how deeply the generation of CO_2 is integrated into modern technology.[1,5] Together, these challenges make it difficult to avoid CO_2 generation altogether, and suggest the need for technologies that can readily store and mitigate CO_2.[1]

Several routes are being considered for CO_2 storage. One such method is the geo-storage of CO_2 by carbon capture and storage processes (CCS), whereby CO_2 is pressurized and stored in aquifers and mineral veins underground.[8] This method aims to semi-permanently store CO_2 in underground deposits, but faces questions of geological stability, gas leakage, high energy input, and finite geological supply that need to be addressed.[8] Another promising method of storage is to utilize biological specimens to capture and convert CO_2 to fuels and value added molecules (carbon capture and usage, CCU) by coupling with photosynthesis or feedstocks generated from renewable energy[9,10]. However, large scale specialized facilities requirements, as well as challenging product separations may be problematic. While recognizing the importance of utilizing multiple strategies for CO_2 mitigation, this thesis will focus on the challenges of direct CO_2 electroreduction to fuels, whereby intermittently generated renewable energy can be used to drive the direct reduction of CO_2 to fuels such as CO, C_2H_4, CH_4, and others. In this process, intermittently generated electrical energy can be stored in chemical bonds, which can be used for carbon storage as well as for fuel in a carbon-neutral process.

1.2 Challenges in electrochemical CO_2 reduction

Intermittent renewable electricity can be stored in the energy dense bonds of chemical fuels via the electrochemical reduction of CO_2.[11–14] However, the low efficiencies and high costs of current CO_2-to-fuels technologies have impeded their widespread commercial deployment.[14] In fact, to convert 500 g of CO_2 into CO, which is the approximate amount generated by a gas turbine to produce 1 kWh of energy, 0.8 to 1.5 kWh of renewable energy is estimated to be required to be carbon neutral through a highly efficient electrolyzer.[15] While this energy requirement may not be inherently problematic from an energy storage point of view, higher renewable energy requirements will inevitably drive up costs for new renewable energy deployment. Therefore, high product selectivity is critical for efficient CO_2 reduction, as well as for minimizing additional energy inputs required in product separation. Unfortunately, a principle impediment to the development of practical CO_2-to-fuels devices is the lack of efficient and selective catalysts for the multi-electron, multi-proton reduction of CO_2. The multiple interfacial electron and proton steps involved in CO_2 electroreduction make achieving high selectivity a challenging chemical problem.[13] Furthermore, CO_2 reduction selectivity is most often limited by the parasitic H_2 evolution. As CO_2 reduction is most practically carried out in aqueous and protic electrolytes, the reduction of protons to H_2 often outcompetes CO_2-to-fuels conversion, eroding reaction selectivity. Thus, a key requirement for any viable catalyst is the ability to preferentially activate CO_2 over H^+ despite the relative kinetic difficulty of the former. The importance of this initial selectivity-determining step is highlighted on Ag and Au surfaces[13,16] which principally generate CO (Eq. 1.1) and H_2 (Eq. 1.2) via the following electrochemical half reactions:

$$CO_2 + 2H^+ + 2e^- \rightarrow CO + H_2O \qquad \text{(Eq. 1.1)}$$

$$2H^+ + 2e^- \rightarrow H_2 \qquad \text{(Eq. 1.2)}$$

While the CO produced via Eq. 1.1 can be further reduced to a wide array of higher order carbonaceous products on Cu metal surfaces, the initial kinetic branching ratio between CO and H_2 production places an upper limit on overall CO_2-to-fuels selectivity.[13,16–19] Despite the central role of this initial kinetic branch point, there remains a scarcity of general materials design principles for realizing selective CO_2 over H^+ conversion, impeding the systematic development of CO_2-to-fuels catalysts.[13]

Herein, a holistic approach to improving CO_2 reduction selectivity will be explored, beginning with methodologies to measure electrocatalyst surface areas to enable intrinsic activity comparisons of CO_2 reduction catalysts, which is essential for deconvoluting the origin of catalyst selectivity (Chapter 2). Knowledge of accurate surface areas enabled the studies shown in Chapters 3 and 4, which demonstrate that catalyst roughness (mesostructure) can impact CO_2 reduction selectivity. In Chapter 5, the kinetics dictating CO_2 reduction selectivity on Cu is explored, followed by a discussion of attempts to directly engineer electrocatalyst active sites by electrodeposition for selective CO_2 reduction informed by CO intermediate kinetics and thermodynamics on Cu.

1.3 Mechansism of CO_2 electroreduction

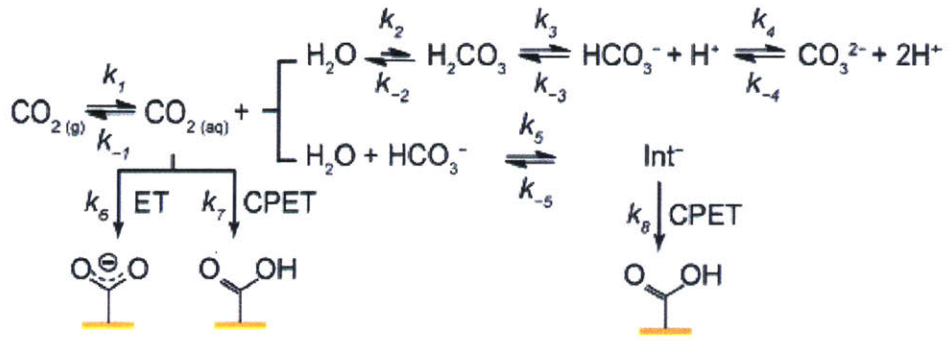

Figure 1.1. Possible pathways for involvement of bicarbonate anion for CO_2 electroreduction on an electrode surface up to the first electron transfer (ET) or concerted proton electron transfer (CPET) step. A recently proposed new equilibrium which forms an anionic adduct (Int^-) of water, CO_2, and bicarbonate, is also included.

The mechanism of CO_2 electroreduction is a widely studied topic, and several pathways to various products have been proposed.[18,20–26] We focus on the relatively simple but critical case of CO_2 reduction on Au surfaces in aqueous bicarbonate electrolytes that produce CO or H_2 from water reduction, which is the first branching point between H_2 and other more reduced hydrocarbons in CO_2 electroreduction. As there is little thermodynamic selectivity between CO_2 reduction to CO and other products and H_2 evolution, the selectivity is dictated primarily by the kinetics of CO_2 activation and the multiple proton coupled electron transfer steps.[18,27] However, multiple pathways have been proposed for this transformation.[21–26] The first step is considered to be the dissolution of CO_2 into water (k_1). This CO_2 can then react with the catalyst[22–26,28,29] (k_6 or k_7) or be slowly hydrated[30,31] (k_2 = 2.9 x 10^{-2} s^{-1}) to form predominantly bicarbonate in neutral conditions. One proposed pathway involves the concerted proton coupled reduction of a water/CO_2/bicarbonate adduct (k_5 and k_8) to form a surface carbonate species, which is further reduced to CO.[21] However, recent kinetic insights on Au catalyzed CO_2 reduction have shown that the rate of CO evolution is independent of HCO_3^- concentration, suggesting that this route is not the dominant process on the surface (Figure 1.2). Instead, Wuttig et. al. have shown that the kinetics of CO_2 reduction are dependent on the partial

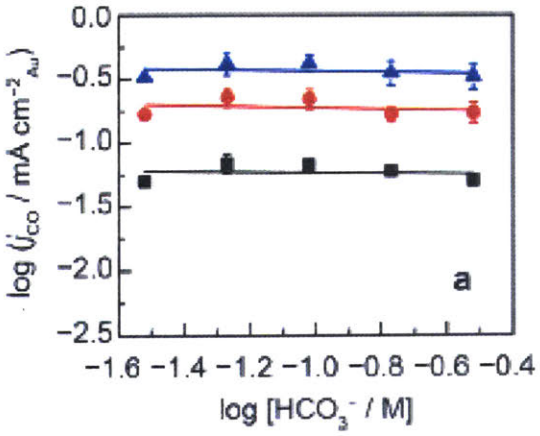

Figure 1.2. Electrokinetic data for CO evolution catalysis. Bicarbonate concentration dependence of CO partial current density at −0.80 V (black), −0.90 V (red), and −1.00 V (blue) vs SHE recorded in CO_2-saturated bicarbonate electrolyte at constant 0.3 M ionic strength balanced by sodium perchlorate.

pressure of CO_2, and likely gated by a $1e^-$ transfer in the rate limiting step.[28,29] Furthermore, deuterium isotope studies in this reaction show no impact of a deuterium isotope effect, suggesting that a proton is not involved in the rate limiting electron transfer step to CO_2 from the surface, pointing at k_6 to be the dominant kinetic pathway.[29] Meanwhile, the evolution of H_2 shows a first order dependence on HCO_3^-, suggesting that HCO_3^- is the proton donor for H_2 evolution on the surface.[29] These findings have led to improved understanding of how catalyst mesostructure induced diffusion limitations can impact CO_2 reduction selectivity in Chapters 3 and 4.

Unlike Au surfaces, Cu surfaces have a relatively strong binding strength of CO intermediates on the surface, with CO spectroscopically present on Cu sites irreversibly.[16,20,32] This allows for further reduction of CO on Cu surfaces to make fuels such as CH_4, C_2H_4, C_2H_5OH, and C_3H_7OH.[16] In Chapter 5, this thesis will outline strategies involving electrolyte composition tuning and Cu surface engineering to impact product selectivity. The strategies will be informed by studies on the kinetics of CO_2 and CO reduction on Cu surfaces, which will be discussed in this chapter.

1.4 CO_2 electroreduction selectivity as an aggregate of effects: electrode roughness, electrolyte composition, and active site activity,

As discussed above, improving the selectivity for direct CO_2 electroreduction to fuels is a critical component to the application of this technology. To this end, knowledge of the mechanisms of CO_2 reduction to fuels and of the various equilibria of substrates and intermediates can inform methods to rationally tune the selectivity of CO_2 reduction.

An important but often overlooked first step for understanding the origins of and improving CO_2 reduction activity is to have knowledge of the electrochemical surface areas of the electrocatalysts, without which accurate comparisons of catalyst activity is impossible. As catalytic CO_2 electroreduction is an interfacial phenomenon whereby active sites on the electrode surface catalyze substrate reduction, it is critical to be able to quantify the surface area of the electrode in order to determine the activity of the electrode, and to quantify the contribution of large surface area on the observed total current. In a homogenous catalysis analogue, attempting to study catalysis on heterogeneous electrochemical systems without a sense of the active area would be akin to studying catalytic activity without knowledge of the catalyst concentration, which would invalidate efforts at kinetic analysis. Unfortunately, determining the surface area of lab-scale electrocatalysts with varying composition and morphologies may not always be readily achievable.[33] To address the need for robust and general methods for lab-scale electrode surface area determination, the following chapter (Chapter 2) will first describe the development of a robust, yet simple empirical methodology for estimating the surface areas of electrodes with varying composition using double layer capacitance in suitable electrolytes.

Knowledge of the mechanism and various substrate equilibria in CO_2 reduction as well as the electrocatalyst surface area allow for the discovery of a previously overlooked strategy

for improving CO_2 reduction selectivity over the parasitic H_2 evolution reaction. CO_2 reduction selectivity can be improved by exploiting the slow rate of CO_2 hydration to form bicarbonate, which acts as the dominant proton donor gating H_2 evolution during CO_2 electroreduction.[28,29] The very act of using a porous or highly rough electrode can induce diffusion gradients of the proton donor species, impacting CO_2 selectivity. In Chapters 3 and 4, we demonstrate how this effect leads to selective CO_2 reduction on both Au and Ag electrodes, and even the promotion of CO_2 reduction activity on Ag surfaces in an unprecedented way.[34,35] To enable these studies, knowledge of electrode surface areas were crucial for measuring the degree of electrode roughness (real surface area / geometric surface area), which is required to systematically correlate the electrode roughness with catalytic activity. The observation of catalyst mesostructuring improving catalyst selectivity has broader implications as well, suggesting that the observed reaction selectivities on nanoparticulate and nanostructured catalysts reported in literature are likely to be complex convolutions of both active site effects and substrate diffusional effects that are imposed by the morphology of the electrodes.

Insight into the mechanism of CO_2 reduction can also provide clues toward tuning the selectivity of CO_2 to more reduced hydrocarbons beyond CO. To study this selectivity, we focus on Cu catalysts on which we can readily observe more reduced ($> 2e^-$) hydrocarbon products, attributed in part to long lived surface CO intermediates that can be further reduced.[16] The ability to further reduce CO to hydrocarbon products such as CH_4, C_2H_4, and C_2H_5OH have made Cu catalysts an attractive platform to study CO_2 and CO reduction in aqueous electrolytes. Unfortunately, not much is known about the pathways that lead to product selectivity, due in part to experimental challenges in studying the kinetics of CO_2 reduction in aqueous electrolytes. To address this void, Chapter 5 describes efforts to control hydrocarbon selectivity by first exploring the kinetics of H_2, CH_4, and C_2H_4 selectivity during CO reduction. The conclusions from studying the kinetics of product selectivity provide insight into methods for

improving CO_2 reduction selectivity by changing the composition of the electrolyte and engineering surface active sites. In particular, the results suggest the need to have active sites that have high CO binding affinity for selectively generating C_2H_4 and other C_2 products. To synthesize electrocatalysts with a high population of sites with enhanced CO adsorption energies, we discuss methods to electrodeposit electrodes with a high population of meta-stable grain boundary defect sites (boundaries between single crystalline domains within the electrode) that have been shown on Au and Cu have shown to be selective for CO_2 and CO activation at low overpotentials.[17,36,37] The increased activity and CO_2 reduction selectivity of these sites has been attributed to a higher binding affinity for CO intermediates generated during catalysis, enabling further reduction to hydrocarbon products.[38,39] However, as these catalysts are primarily generated by the reduction of bulk-oxidized surfaces, the precise control of grain-boundary generation is difficult. Thus, we apply a bottom-up approach to synthesize grain boundary rich nanocrystalline Cu catalysts by using electrodeposition, and test these electrodes are then tested for CO_2 reduction.

In the quest to improve direct CO_2 electroreduction selectivity, this thesis will show that the chemistry of CO_2 reduction is a complex convolution of several components, including the roughness of the electrode, the nature of the electrolyte, and the nature of the active site chemistry. Furthermore, this thesis will highlight the importance of understanding the surface area of CO_2 electrocatalysts and the kinetic pathways of CO_2 reduction that inform rational design principles for improving CO_2 reduction selectivity. The development of CO_2 reduction catalyst systems must therefore take into account the holistic impact of all of these factors.

1.5 References

(1) Pachauri, R. K.; Allen, M. R.; Barros, V. R.; Broome, J.; Cramer, W.; Christ, R.; Church, J. A.; Clarke, L.; Dahe, Q.; Dasgupta, P.; Dubash, N. K.; Edenhofer, O.; Elgizouli, I.; Field, C. B.; Forster, P.; Friedlingstein, P.; Fuglestvedt, J.; Gomez-Echeverri, L.; Hallegatte, S.; Hegerl, G.; Howden, M.; Jiang, K.; Cisneroz, B. J.; Kattsov, V.; Lee, H.; Mach, K. J.; Marotzke, J.; Mastrandrea, M. D.; Meyer, L.; Minx, J.; Mulugetta, Y.; O'Brien, K.; Oppenheimer, M.; Pereira, J. J.; Pichs-Madruga, R.; Plattner, G.-K.; Pörtner, H.-O.; Power, S. B.; Preston, B.; Ravindranath, N. H.; Reisinger, A.; Riahi, K.; Rusticucci, M.; Scholes, R.; Seyboth, K.; Sokona, Y.; Stavins, R.; Stocker, T. F.; Tschakert, P.; van Vuuren, D.; van Ypserle, J.-P. Climate Change 2014: Synthesis Report. Contribution of Working Groups I, II and III to the Fifth Assessment Report of the Intergovernmental Panel on Climate Change; Pachauri, R. K., Meyer, L., Eds.; IPCC: Geneva, Switzerland, 2014.

(2) Cook, J.; Nuccitelli, D.; Skuce, A.; Jacobs, P.; Painting, R.; Honeycutt, R.; Green, S. A.; Lewandowsky, S.; Richardson, M.; Way, R. G. Energy Policy **2014**, 73, 706.

(3) Cook, J.; Oreskes, N.; Doran, P. T.; Anderegg, W. R. L.; Verheggen, B.; Maibach, E. W.; Carlton, J. S.; Lewandowsky, S.; Skuce, A. G.; Green, S. A.; Nuccitelli, D.; Jacobs, P.; Richardson, M.; Winkler, B.; Painting, R.; Rice, K. Environ. Res. Lett. **2016**, 11 (4), 48002.

(4) NASA: Climate Change and Global Warming https://climate.nasa.gov/ (accessed Mar 1, 2018).

(5) Melillo, J. M. Climate change impacts in the United States: the third national climate assessment; Government Printing Office, 2014.

(6) Crabtree, G.; Misewich, J.; Ambrosio, R.; Clay, K.; DeMartini, P.; James, R.; Lauby, M.; Mohta, V.; Moura, J.; Sauer, P.; others. In AIP Conference Proceedings; 2011; Vol. 1401, pp 387–405.

(7) Commission, I. E.; others. IEC White Pap. Geneva Int. Electrotech. Comm. www. iec. ch/whitepaper/pdf/iecWP-gridintegrationlargecapacity-LR-en. pdf (last accessed March 2015) **2012**.

(8) Coninck, H. C. de; Loos, M. A.; Metz, B.; Davidson, O.; Meyer, L. Intergov. Panel Clim. Chang. **2005**.

(9) Liu, C.; Colón, B. C.; Ziesack, M.; Silver, P. A.; Nocera, D. G. Science (80-.). **2016**, 352 (6290), 1210.

(10) Wang, B.; Li, Y.; Wu, N.; Lan, C. Q. Appl. Microbiol. Biotechnol. **2008**, 79 (5), 707.

(11) Tang, W.; Peterson, A. A.; Varela, A. S.; Jovanov, Z. P.; Bech, L.; Durand, W. J.; Dahl, S.; Nørskov, J. K.; Chorkendorff, I. Phys. Chem. Chem. Phys. **2012**, 14 (1), 76.

(12) Kuhl, K. P.; Hatsukade, T.; Cave, E. R.; Abram, D. N.; Kibsgaard, J.; Jaramillo, T. F. J. Am. Chem. Soc. **2014**, 136 (40), 14107.

(13) Hori, Y. In Modern Aspects of Electrochemistry; Vayenas, C., White, R., Gamboa-Aldeco, M., Eds.; Modern Aspects of Electrochemistry; Springer New York: New York, NY, 2008; Vol. 42, pp 89–189.

(14) Jones, J.-P.; Prakash, G. K. S.; Olah, G. A. Isr. J. Chem. **2014**, 54 (10), 1451.

(15) Kauffman, D. R.; Thakkar, J.; Siva, R.; Matranga, C.; Ohodnicki, P. R.; Zeng, C.; Jin, R. ACS Appl. Mater. Interfaces **2015**, 7 (28), 15626.

(16) Peterson, A. A.; Nørskov, J. K. J. Phys. Chem. Lett. **2012**, 3 (2), 251.

(17) Li, C. W.; Kanan, M. W. J. Am. Chem. Soc. **2012**, 134 (17), 7231.

(18) Gattrell, M.; Gupta, N.; Co, A. J. Electroanal. Chem. **2006**, 594 (1), 1.

(19) Kuhl, K. P.; Cave, E. R.; Abram, D. N.; Jaramillo, T. F. Energy Environ. Sci. **2012**, 5 (5), 7050.

(20) Kortlever, R.; Shen, J.; Schouten, K. J. P.; Calle-Vallejo, F.; Koper, M. T. M. J. Phys. Chem. Lett. **2015**, 6 (20), 4073.

(21) Dunwell, M.; Lu, Q.; Heyes, J. M.; Rosen, J.; Chen, J. G.; Yan, Y.; Jiao, F.; Xu, B. J. Am. Chem. Soc. **2017**, 139, 3774.

(22) Hatsukade, T.; Kuhl, K. P.; Cave, E. R.; Abram, D. N.; Jaramillo, T. F. Phys. Chem. Chem. Phys. **2014**, 16 (27), 13814.

(23) Hansen, H. A.; Varley, J. B.; Peterson, A. A.; Nørskov, J. K. J. Phys. Chem. Lett. **2013**, 4 (3), 388.

(24) Peterson, A. A.; Abild-Pedersen, F.; Studt, F.; Rossmeisl, J.; Nørskov, J. K. Energy Environ. Sci. **2010**, 3 (9), 1311.

(25) Zhu, W.; Zhang, Y.-J.; Zhang, H.; Lv, H.; Li, Q.; Michalsky, R.; Peterson, A. A.; Sun, S. J. Am. Chem. Soc. **2014**, 136 (46), 16132.

(26) Zhu, W.; Michalsky, R.; Metin, Ö.; Lv, H.; Guo, S.; Wright, C. J.; Sun, X.; Peterson, A. A.; Sun, S. J. Am. Chem. Soc. **2013**, 135 (45), 16833.

(27) Koper, M. T. M. Chem. Sci. **2013**, 4 (7), 2710.

(28) Wuttig, A.; Yoon, Y.; Ryu, J.; Surendranath, Y. J. Am. Chem. Soc. **2017**, 139 (47), 17109.

(29) Wuttig, A.; Yaguchi, M.; Motobayashi, K.; Osawa, M.; Surendranath, Y. Proc. Natl. Acad. Sci. **2016**, 113 (32), E4585.

(30) Pocker, Y.; Bjorkquist, D. W. J. Am. Chem. Soc. **1977**, 99 (20), 6537.

(31) Adamczyk, K.; Premont-Schwarz, M.; Pines, D.; Pines, E.; Nibbering, E. T. J. Science (80-.). **2009**, 326 (5960), 1690.

(32) Wuttig, A.; Liu, C.; Peng, Q.; Yaguchi, M.; Hendon, C. H.; Motobayashi, K.; Ye, S.; Osawa, M.; Surendranath, Y. ACS Cent. Sci. **2016**, 2 (8), 522.

(33) Yoon, Y.; Yan, B.; Surendranath, Y. J. Am. Chem. Soc. **2018**, 140 (7), 2397.

(34) Yoon, Y.; Hall, A. S.; Surendranath, Y. Angew. Chemie Int. Ed. **2016**, 55 (49), 15282.

(35) Hall, A. S.; Yoon, Y.; Wuttig, A.; Surendranath, Y. J. Am. Chem. Soc. **2015**, 137 (47), 14834.

(36) Chen, Y.; Li, C. W.; Kanan, M. W. J. Am. Chem. Soc. **2012**, 134 (49), 19969.

(37) Feng, X.; Jiang, K.; Fan, S.; Kanan, M. W. J. Am. Chem. Soc. **2015**, 137 (14), 4606.

(38) Feng, X.; Jiang, K.; Fan, S.; Kanan, M. W. ACS Cent. Sci. **2016**, 2 (3), 169.

(39) Mariano, R. G.; McKelvey, K.; White, H. S.; Kanan, M. W. Science (80-.). **2017**, 358 (6367), 1187.

Chapter 2 – Non-aqueous double layer capacitance for the estimation of electrochemical surface area

This chapter contains text from the following article:

(1) Yoon, Y.; Yan, B.; Surendranath, Y. Suppressing Ion Transfer Enables Versatile Measurements of Electrochemical Surface Area for Intrinsic Activity Comparisons. J. Am. Chem. Soc. **2018**, 140 (7), 2397.

2.1 Introduction

Conductive electrodes are central to a wide variety of devices including batteries, fuel cells, electrolyzers, capacitors, and sensors. In each case, the performance of the electrode is a summation of the intrinsic properties of the electroactive material and a key extrinsic factor, the surface area of the electrode. Thus, a careful account of the electrochemically active surface area (ECSA) is essential for correlating the aggregate performance of an electrode to the intrinsic properties of the material under investigation. This is particularly true for highly nanostructured electrodes, for which dramatic variations in ECSA between different electrode preparations[1,2] can obscure the underlying intrinsic performance metrics that are required for accurate structure-function correlations, comparisons to theoretical models, and rational materials design. Unfortunately, many studies on electrochemical CO_2 reduction, and indeed electrochemical catalysis overall, overlook the characterization of surface area while making strong structure-activity correlations.

Numerous complementary methods exist for measuring ECSA, but with significant limitations. Gas adsorption analysis typically requires a minimum real surface area of ~1000 cm^2, far greater than the 0.1-100 cm^2 values typical of common laboratory scale electrodes.[3] This sensitivity challenge can be overcome using electrochemical adsorption probes such as underpotential deposition (UPD), CO stripping, and surface monolayer oxidation.[4,5]

Unfortunately, since these probes rely on chemisorption, they can only be applied to a limited subset of surface structures (e.g., appropriate facets of noble metals) that display the necessary adsorption thermochemistry and kinetics. Additionally, these adsorption methods often utilize acutely toxic chemical probes including Tl, Cd, Pb, Hg, and CO, that impede routine use.[4–6] Moreover, these methods often destroy the surface by inducing restructuring and/or irreversible alloying that prevents repeated measurements of the same electrode.[7–9] Electrochemical adsorption probes are also prone to error stemming from the nonsystematic integration of surface waves that are convoluted by adjacent bulk redox features and variable capacitive baselines.[4,5,10] Clearly, more general electrochemical methods for measuring ECSA across diverse materials are desired.

For the vast majority of materials for which well-characterized adsorption probes are not available, double layer capacitance (DLC) measurements offer a versatile and nondestructive alternative for estimating ECSA. The DLC reports directly on the amount of charge accumulated at the electrode surface, and is thus directly correlated to the ECSA.[2,5,10,11] Therefore, DLC measurements could be used as a general tool for estimating ECSA across diverse materials provided that each material displays a similar capacitance per real surface area (specific capacitance). Unfortunately, ion transfer reactions at the interface,

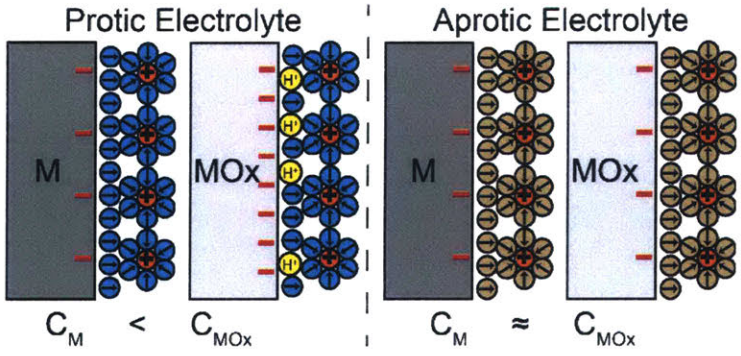

Figure 2.1. Comparison of capacitive electrode response for metals (C_M) and oxides (C_{MOx}). H+ adsorption in protic electrolytes (left, blue) leads to higher capacitance for oxides (C_{MOx}) than for metals (C_M). This work postulates similar capacitance for disparate materials in a weakly adsorbing aprotic electrolyte (right, brown).

including corrosion, intercalation, and specific adsorption, can lead to additional current that convolutes the DLC measurement, introducing large variability in specific capacitance values[5,10–12] across materials. These convoluting reactions are particularly pronounced for metal oxide and chalcogenide surfaces, for which H^+/OH^- adsorption can inflate specific capacitance values by as much as an order of magnitude.[11] Given the central role of surface proton transfer in these chemisorption processes, we postulated that DLC data collected in polar aprotic electrolytes would permit the observation of more uniform specific capacitance values across diverse materials (Figure 2.).

In this chapter, we use atomic force microscopy (AFM) surface area measurements to calculate specific capacitance values across 19 materials spanning metals, metal oxides, and metal chalcogenides. Using these data, we establish simple DLC measurement protocols in CH_3CN electrolytes, which are readily prepared with low water content, display high conductivity, and are relatively chemically inert. We find that diverse materials exhibit similar specific capacitance values in this aprotic electrolyte, establishing a powerful empirical methodology for estimating ECSA, thereby allowing for systematic comparisons of intrinsic electrode activity.

2.2 Results and Discussion

2.2.1 Synthesis and AFM surface area measurements of planar electrodes

To quantify specific capacitance values (measured in μF/real cm^2) across various materials and measurement conditions, we measured the real surface area of each electrode using AFM, an established method for determining the surface areas of nominally planar thin film electrodes.[5,10,13] AFM measurements are independent of the surface chemistry of the material but are limited to characterizing nonporous substrates. Thus, we synthesized dense thin film electrodes of various compositions using metal evaporation techniques and electrodeposition. Using these methods, we examined 19 planar, nonporous, thin-film electrodes spanning noble metals (Ag, Au, Pd, Pt), oxide-passivated base metals (Al, Cr, Fe, Mo, Ni, $Ni_{0.8}Fe_{0.2}$, Ta, Ti), conductive carbon (graphite), bulk conductive oxides (F-doped SnO (FTO), NiFeOx, RuO_2), and metal chalcogenides ($CoSe_x$, $NiSe_x$, NiS_x). In all cases, AFM measurements revealed highly planar films with roughness factors of 1.0−1.1 (see Section 2.4 for AFM height profiles for all materials). The AFM-derived roughness of each electrode was then used to calculate the surface area of each sample and its specific capacitance.

2.2.2 Determination of specific capacitance from DLC and AFM measurements

The ECSA's of the planar electrode films were determined by analysis of the DLC of each electrode. DLC measurements in both aqueous and non-aqueous electrolytes were performed at the OCP unless otherwise specified. In non-aqueous aprotic electrolyte, the OCP

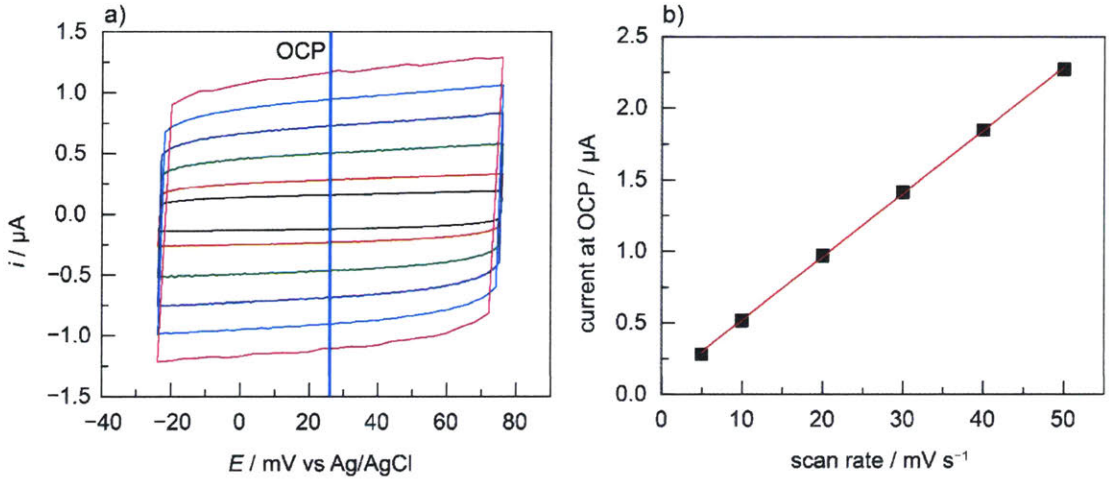

Figure 2.2. Representative CV traces (a) centered at the OCP (blue vertical line) were used to measure electrode capacitive currents. Representative plot of capacitive current at OCP vs scan rate (b). Red line is a linear fit to the data and the slopes of these lines were used to calculate the electrode capacitance as described above for each sample. The particular data set shown here was recorded on a polycrystalline Au electrode.

values were observed to drift slightly (~50 mV) due to the absence of a dominant solution redox process. Thus, the OCP values used for DLC measurements were typically taken as those recorded after ~100 s of double layer equilibration. For each DLC measurement, CV scans spanning ±50 mV of the OCP were recorded at scan rates of 5, 10, 20, 30, 40, and 50 mV/s. The resulting capacitive CV traces (Figure 2.a) were used to calculate the capacitive current as the difference between the cathodic and anodic currents, $(i_a - i_c)$, at the OCP. These aggregate capacitive currents were then plotted vs scan rate (Figure 2.b) and the slope of this plot was divided by 2 to obtain the electrode capacitance at the OCP (Eq. 2.1):

$$\text{elecrode capacitance} = \frac{1}{2}\frac{\partial(i_a - i_c)}{\partial(\text{scan rate})} \qquad \text{(Eq. 2.1)}$$

The specific capacitance was then determined by dividing the electrode capacitance by the electrode area estimated by AFM (Eq. 2.2):

$$\text{specific capacitance} = \frac{\text{electrode capacitance}}{\text{area}_{\text{real}}} \quad \text{(Eq. 2.2)}$$

To determine whether the experimental mean value of 11 $\mu F/cm^2$ is roughly in line with the physicochemical properties of our electrochemical interfaces, we construct a simple physical parallel plate capacitor (Stern) model where solvated electrolyte is arranged at the electrode surface. K^+ and PF_6^- have solvated radii of ~4 and 2 Å, respectively[14,15] Assuming a monolayer of acetonitrile solvating the surface (3 Å), we estimate a compact double layer thicknesses (d) of ~5-7 Å. At the relatively high dielectric strengths explored here, the compact double layer capacitance is expected to dominate the overall capacitance[16]. Using a parallel plate model for the compact layer capacitance (Eq. 2.3, Eq. 2.4), our observed mean value of 11 $\mu F/cm^2$ requires an interfacial dielectric constant (k) of 6-9. These values are suppressed relative to the bulk dielectric of CH_3CN, $\varepsilon = 36$, but are reasonable given the strong solvent ordering at a polarized interface.

$$\frac{\text{capacitance}}{A} = \frac{k\varepsilon_0}{d} \quad \text{(Eq. 2.3)}$$

$$k = \frac{k\varepsilon_0 A}{\text{capacitance} \times d} \quad \text{(Eq. 2.4)}$$

Capacitance = 11 $\mu F/cm^2$

k = interfacial dielectric constant of CH_3CN (relative permittivity) = 6 ~ 9

ε_0 = permittivity constant = 8.854×10^{-8} $\mu F/cm$

A = area of plate (cm^2)

d = compact double layer thickness = $5 \times 10^{-8} \sim 7 \times 10^{-8}$ cm

2.2.3 Specific capacitance of planar electrodes in aqueous electrolyte

To investigate the impact of protic electrolytes on DLC measurements, we compared specific capacitance values recorded in 0.15 M $NaClO_4$ aqueous electrolyte with those measured in 0.15 M KPF_6 with CH_3CN electrolyte. In all cases, DLC measurements were performed by recording cyclic voltammetry (CV) cycles over a narrow range (±50 mV) centered around the open circuit potential (OCP). CV cycling was repeated using a range of scan rates from 5 to 50 mV/s. The capacitive current at the OCP was plotted vs scan rate, and the DLC values were extracted from slopes of these plots (Figure 2.). DLC values were then divided by the AFM-derived surface area of each electrode to determine the specific capacitance of the material under investigation. Specific capacitance values measured in aqueous media display a wide variability across the materials explored, despite precautions taken to minimize specific adsorption of electrolyte ions. All aqueous DLC data were recorded in 0.15 M $NaClO_4$ (Figure 2.), and this electrolyte was chosen because both the Na^+ cation and the ClO_4^- anions are known to be well-hydrated and weakly coordinating to metal surfaces.[17,18] Under these conditions, noble metals such as Au and Pd display specific capacitance values of ~8 $\mu F/cm^2$, at the low end of the values typically assumed for a metal surface. [16,19,20] This suggests that for these materials, DLC measurements are not dramatically convoluted by specific adsorption contributions and accurately reflect the true surface areas of the materials. Ag and Pt display larger specific capacitance values of 40 and 35 $\mu F/cm^2$ in aqueous electrolyte, perhaps due to the impact of strongly adsorbed OH_x species at the OCP values of 0.8 and 0.85 V vs the reversible hydrogen electrode (RHE), respectively. In contrast, metallic electrodes with oxidic surface chemistry exhibit specific capacitance values 2−6 times greater than that of these noble metal surfaces. This increase has been well documented and is attributed, in part, to H^+/OH^- adsorption at the amphoteric oxide surface.[8,20] Interestingly, FTO electrodes display an 8-fold lower specific capacitance than oxide-terminated Fe electrodes, highlighting the

extreme sensitivity of these adsorption processes on surface composition and structure. Likewise, metal chalcogenides display specific capacitance values that vary by a factor of 3 between Ni and Co. In aggregate, across 17 of the 19 materials explored (see Section 2.2.9 for a detailed discussion of MoO_x and RuO_2 outlier materials), we observe an average specific capacitance of 26 $\mu F/cm^2$ with a large standard deviation of ± 16 $\mu F/cm^2$ and a total range of 7–63 $\mu F/cm^2$. Together, these data suggest that aqueous electrolytes are prone to a large variability in specific DLC across materials due to a diversity of surface adsorption equilibria.

2.2.4 Specific capacitance of planar electrodes in aprotic CH_3CN electrolyte

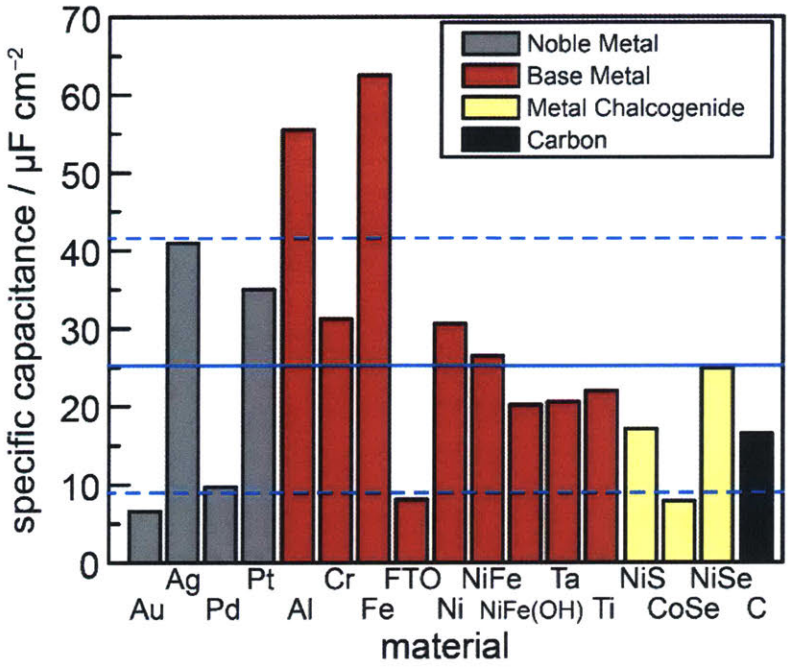

Figure 2.3. Comparison of specific capacitance values of noble metals (gray), surface oxide passivated base metals (red), metal chalcogenides (yellow), and carbon (black) measured by double layer capacitance at ±50 mV of the open circuit potential in 0.15 M $NaClO_4$ aqueous electrolyte. The solid and dotted blue lines denote the average and standard deviations of the specific capacitance values across the tested materials.

DLC data collected in polar, aprotic CH_3CN media display significantly less variability (Figure 2.). Nonaqueous specific capacitance values were recorded in CH_3CN electrolyte containing 0.15 M KPF_6, using the protocol described above. In contrast to the DLC values in H_2O, specific capacitance values in CH_3CN display a range of 3.4−17 μF/cm^2, with an average of 11 and a standard deviation of 4.7. Whereas metal electrodes display a slight rise in capacitance relative to measurements in water, most metal oxides display a significantly lower capacitance. For example, oxide passivated Al and Fe electrodes display values of 6 and 17 μF/cm^2 in CH_3CN electrolyte, respectively, compared to 56 and 63 μF/cm^2 in water. Included in the group of oxides is $NiFeO_x$, a potent catalyst for oxygen evolution, which shows a specific capacitance of 6.7 μF/cm^2, close to the mean value of 11 μF/cm^2.[2,21,22] Although we expect this method will underreport the internal surface area between the layers of this oxide due to

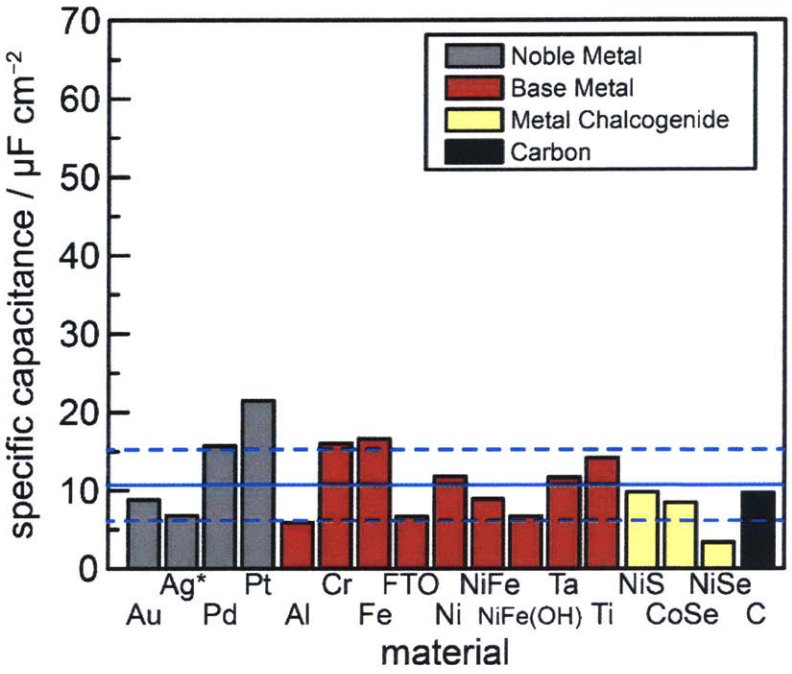

Figure 2.4. Comparison of specific capacitance values of noble metals (gray), surface oxide passivated base metals (red), metal chalcogenides (yellow), and carbon (black) measured by double layer capacitance at ±50 mV of the open circuit potential in 0.15 M KPF_6, CH_3CN electrolyte. The solid and dotted blue lines denote the average and standard deviations of the specific capacitance values across the tested materials. *Ag was measured at −600 mV vs the reference due to corrosion at the OCP.

inhibited ion intercalation, these data suggest that nonaqueous DLC may be a viable method for comparing the bulk-solvent exposed ECSA of oxidic OER catalysts. Likewise, the nonaqueous DLC values of metal chalcogenides fall relative to their aqueous values and, apart from NiSe, exist within one standard deviation of the mean value. Together, the data suggest that, remarkably, apart from the MoO_x and RuO_2 outliers discussed below, aprotic CH_3CN DLC values will generate a reasonable estimate of ECSA (within a factor of ~ 1.8) across diverse materials classes by applying the assumption of a common, empirical specific capacitance value of 11 μF/cm^2. This empirical value is reasonable considering the solvated radii of K^+, PF_6^-, and the dielectric properties of the interface (see Section 2.2.2).[16] Given that the electrochemical and, in particular, electrocatalytic performances of various materials typically differ by orders of magnitude, this level of precision, while imperfect, is well suited to

benchmarking performance across diverse high surface area materials which are not amenable to traditional adsorption probes of ECSA.[2,11]

2.2.5 Impact of DLC measurements on electrode roughness

To ensure a high degree of accuracy and repeated usage of the electrode, the surface area measurement must not significantly alter the surface, which can be a problem in particular for surface redox probes for measuring surface area. To determine the mildness of DLC measurements for determining ECSA, the AFM roughnesses of Au and Ti electrodes were measured before and after DLC measurements under aprotic conditions (Table 2.1. AFM roughness of Au and Ti electrodes before and after non-aqueous DLC measurements in 0.15 M KPF6 / CH3CN electrolyte). AFM measurements reveal no significant change in the surface roughness, suggesting that the technique preserves the native surface of the electrode. The mildness of the DLC-based surface area probe allows for measuring the surface area of the electrode at multiple points during an experiment to quantify areal changes and electrode durability during use.

Electrode	AFM roughness of film pre-DLC measurements	AFM roughness of film post-DLC measurements
Au	1.01	1.01
Ti	1.00	1.00

Table 2.1. AFM roughness of Au and Ti electrodes before and after non-aqueous DLC measurements in 0.15 M KPF_6 / CH_3CN electrolyte

2.2.6 Impact of ion rearrangement kinetics on DLC measurements for ECSA determination

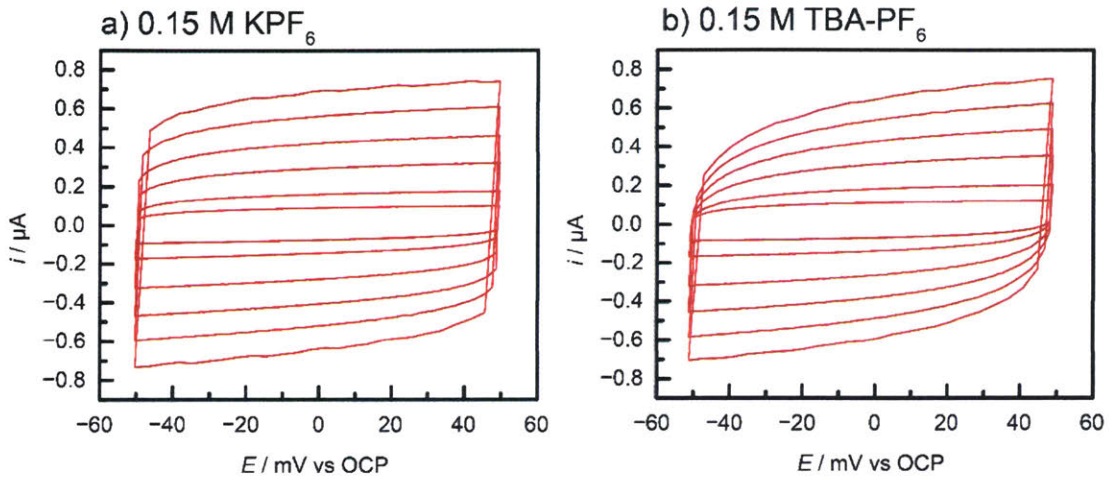

Figure 2.5. CV scans near the open circuit potential (OCP) for the same oxide-passivated Ti electrode in CH_3CN with 0.15 M (a) KPF_6 and (b) TBA-PF_6.

Even in the limit where specific adsorption is negligible, the structure of the electrolyte ions impacts the accuracy of the DLC measurement. To best approximate the ECSA, a rectangular CV scan with a broad current plateau across the potential range is ideal, as it maximizes the linearity in the DLC plot of capacitance current vs scan rate. As highlighted in Figure 2. for oxide passivated Ti electrodes, this ideal limiting behavior is highly sensitive to the structure of the electrolyte ions. Whereas KPF_6 electrolytes give rise to broad plateaus, CV scans recorded in bulkier tetrabutylammonium hexafluorophosphate (TBA-PF_6) electrolytes display noticeable curvature, indicative of sluggish ion rearrangement. While series resistance can contribute to sloping, this has a negligible contribution for these conductive electrodes polarized in a concentrated electrolyte medium. Indeed, the degree of curvature increases with increasing scan rate, reflecting the slower kinetics of rearranging bulkier TBA^+ relative to K^+ ions.[15,23] Sluggish electrolyte rearrangement contributes to greater nonlinearity in the plots of DLC vs scan rate (Figure 2.6). While this nonlinearity contributes to a relatively small change in capacitance (13.0 vs 12.7 µF) for this planar TiO_x example, the error will be more

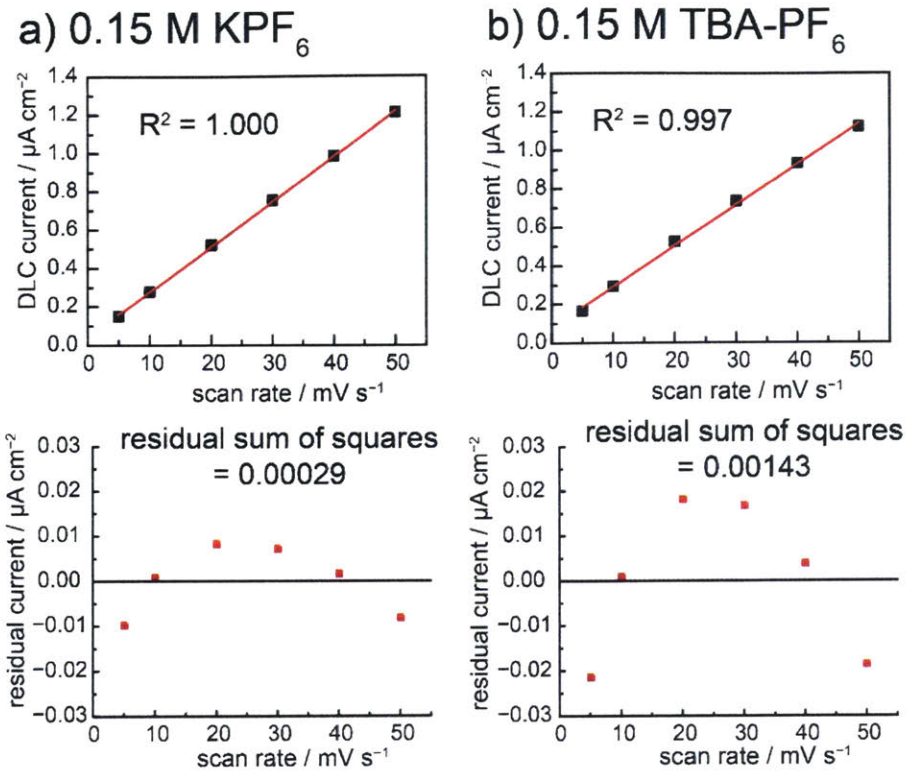

Figure 2.6. DLC current vs scan rate (DLC plot) measured in a) 0.15 M KPF_6 / CH_3CN and b) 0.15 M TBA-PF_6 / CH_3CN of the oxide passivated Ti electrode shown in Figure 2.. The corresponding linear regression error and residual sum of squares for both plots are shown below the DLC plots

pronounced for micro-/mesoporous materials that exhibit impeded ion transport. For these high surface area materials, capacitance data collected at very low scan rates are likely to be most reflective of the true surface area. We stress that for some materials (see Section 2.2.9) electrolyte ion intercalation can significantly convolute DLC data and, in these cases, larger ions may be unavoidable. Nonetheless, the data indicate that, for most materials, smaller electrolyte ions are essential for maximizing the rate of interfacial ion rearrangement, a prerequisite for accurate DLC measurements.

2.2.7 Impact of electrolyte concentration on aprotic DLC measurements for ECSA determination

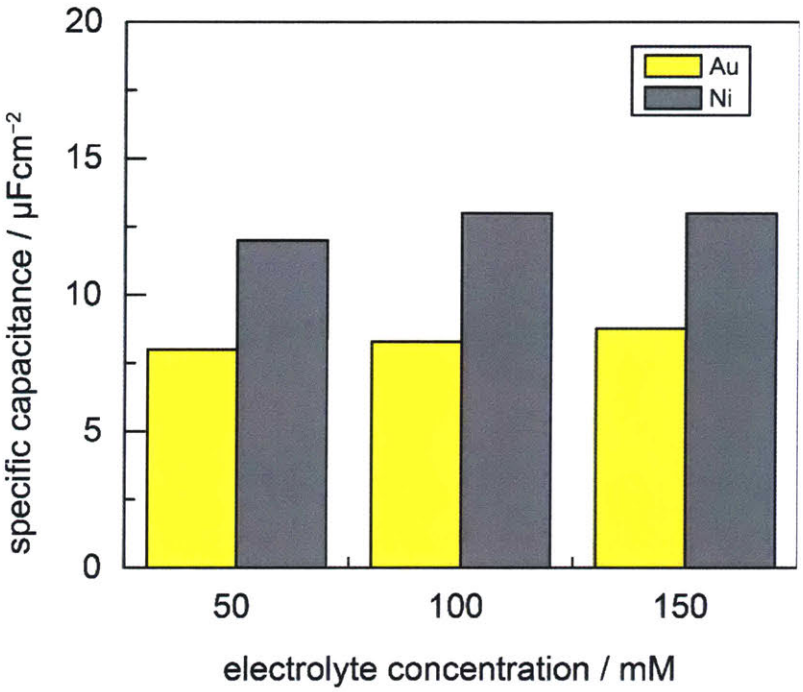

Figure 2.7. Measured specific capacitance of Au and oxide-passivated Ni electrodes at three concentrations of KPF_6 in CH_3CN electrolyte.

Unlike ion size, the concentration of the electrolyte has minimal impact on the DLC measurement (Figure 2.). For Au electrodes, very similar specific capacitance values of 8.4 ± 0.4 μF/cm^2 were obtained over a range of electrolyte concentrations from 0.05 to 0.15 M KPF_6, indicating a minimal dependence on electrolyte strength over this range. Similarly, oxide-passivated Ni electrodes display specific capacitance values of 12.7 ± 0.6 μF/cm^2 over the same range of electrolyte concentrations. While classical double layer theory predicts a strong dependence of the capacitance on electrolyte strength near the potential of zero charge (PZC), our data suggest that this effect is minimal for the samples investigated here. Indeed, PZC values are typically facet dependent and the polycrystalline nature of the samples explored here may impede clear observation of this phenomenon.[20] Furthermore, capacitance minima near the PZC are typically not observed for the relatively high electrolyte strengths examined here.[20]

We stress that high electrolyte concentrations are typically preferred for DLC measurements to ensure high solution conductivity and a high ion concentration at the double layer. In this limit, further variations in electrolyte strength do not dramatically alter the measured capacitance.

2.2.8 Using DLC to measure rough, porous electrodes

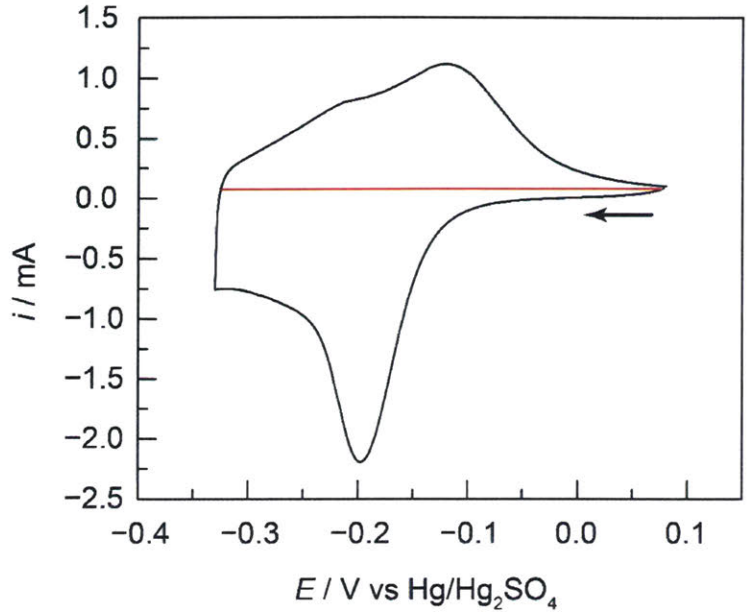

Figure 2.8. Cyclic voltammogram of Cu underpotential deposition and stripping on a high surface area Au electrode. The Au electrode film was cycled from 0.08 V to −0.33 V vs $Hg/HgSO_4$ at a scan rate of 50 mV/s in Ar-saturated 0.05 M H_2SO_4 containing 0.1 M $CuSO_4$. The broad anodic wave beginning at −0.32 V vs $Hg/HgSO_4$ was integrated to 0.00 V and the area above the red line was taken as the stripping charge value. This value was divided by the known stripping charge of Cu on Au[4], 0.46 mC/cm^2, to determine the surface area of the Au films.

Ultimately, the utility of this method depends on whether it can measure the surface areas of highly rough electrodes that one would expect to encounter during research of CO_2 reduction catalysts and other electrochemical systems. To determine the usefulness of this technique, we examined whether nonaqueous DLC measurements could be used to estimate the surface area of highly nanostructured electrodes. We synthesized a series of high surface area Au electrodes via rapid electrodeposition[1] and measured their capacitance in 0.15 M KPF_6/ CH_3CN electrolyte. Au was chosen as a model case to compare DLC-derived ECSA to the values generated using a known Cu UPD probe (Figure 2.). The Cu UPD-derived ECSA values agree well with the DLC-derived ECSA over a wide range of Au roughness factors from ~10 to ~40 (Figure 2.9), indicating that the proposed method for ECSA determination is well suited to analyzing high surface area materials.

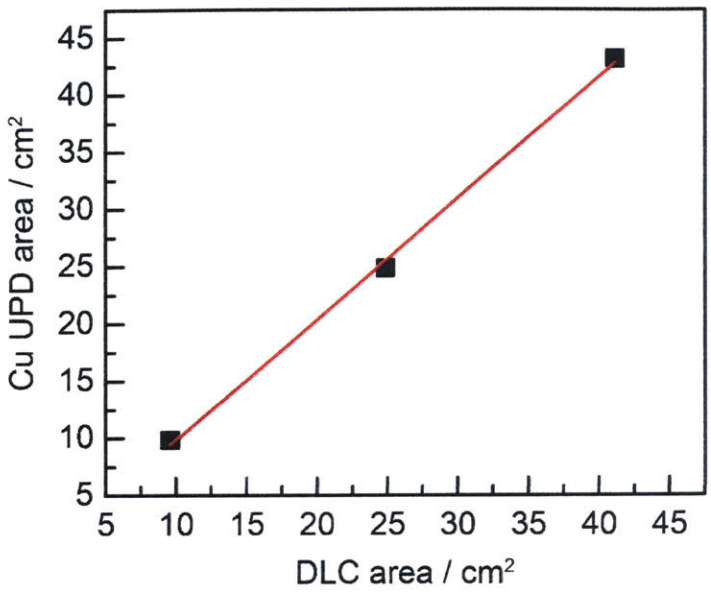

Figure 2.93. ESCA measured by Cu UPD vs ECSA measured by DLC for high surface area electrodeposited Au.

2.2.9 Limitations of aprotic DLC based ECSA determination

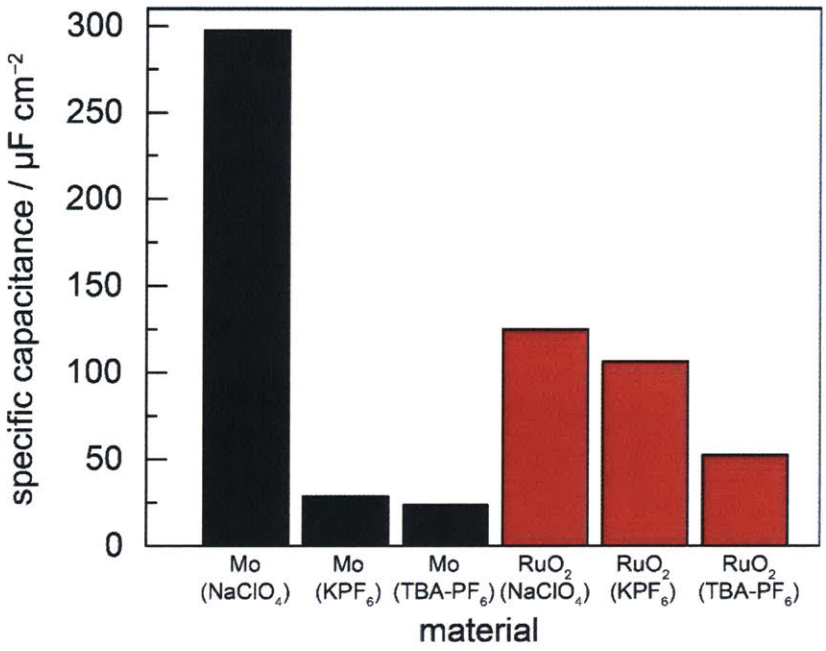

Figure 2.4. Measured specific capacitance of oxide-passivated Mo and RuO_2 electrodes as a function of the electrolyte composition. $NaClO_4$ electrolytes were aqueous, whereas all others were in CH_3CN. Ionic strengths were fixed at 0.15 M for all measurements.

The foregoing data indicate that DLC measurements in KPF_6/CH_3CN electrolytes provide good estimates of ECSA across diverse materials. However, the proposed approach is not well suited to all materials. In particular, known supercapacitor materials such as RuO_2 and oxide-passivated Mo (MoO_x) still display significant ion transfer currents in KPF_6/CH_3CN electrolytes, making them unsuitable for DLC-ECSA analyses using the procedure presented in this work (Figure 2.10). Planar RuO_2 and oxide-passivated Mo display elevated specific capacitance values of 125 and 297 $\mu F/cm^2$ in H_2O at the OCP, respectively, reflecting the high degree of proton and ion adsorption/intercalation in these supercapacitor materials. In aprotic CH_3CN/KPF_6 electrolyte, RuO_2 and MoO_x exhibit decreased yet large specific capacitance values of 107 and 29 $\mu F/ cm^2$. These high values may arise from specific adsorption/ intercalation of electrolyte ions or interactions with trace H_2O known to exist in CH_3CN (~5 ppm).[24] Evidence for cation adsorption/intercalation appears from the fact that the specific capacitances decrease to 53 and 24 $\mu F/cm^2$ for RuO_2 and oxide passivated Mo in the presence

of bulkier TBA-PF_6 electrolyte. These studies highlight that, for new materials in particular, DLC measurements collected across a range of nonaqueous electrolytes provide the best indication of the true ECSA.

2.3 Concluding remarks

Through careful selection of an electrolyte that minimizes interfacial ion transfer reactions while maximizing the kinetics of electrolyte rearrangement, we have demonstrated that aprotic DLC measurements in CH_3CN yield similar (~11 $\mu F/cm^2$) specific capacitance values for a wide range of noble metals, oxide-passivated base metals, graphitic carbon, bulk conductive oxides, and metal chalcogenides. Given that the vast majority of known and emerging electroactive materials do not yield to traditional ECSA measurements, the strategy established and validated here provides a simple and powerful tool for translating the current/voltage parameters of nanostructured electrodes into intrinsic materials performance metrics that will enable systematic comparisons and guide rational materials design. In the context of electrochemical catalysis and CO_2 reduction, knowledge of the ECSA is crucial to understanding the origin and kinetics of electrode activity and to compare the performance of highly rough electrocatalysts in a systematic and accurate manner.

2.4 Experimental methods

Materials. For DLC measurements, the following materials were used without additional purification: gold-coated (100 nm thick) glass slides (EMF corporation, 5 nm Ti adhesion layer), titanium-coated (100 nm thick) glass slides (as main substrate, EMF corporation), titanium wire (99.99%, 1 mm dia., Alfa Aesar), TEC-7 F-doped tin oxide (FTO) slides (Hartford Glass), anhydrous acetonitrile (Jackson and Burdick / Fischer DNA synthesis grade), potassium hexafluorophosphate (KPF_6, 99.5 %, Strem Chemicals), tetrabutylammonium hexafluorophosphate (TBA-PF_6, electrochemical grade, Sigma Aldrich), and sodium perchlorate (99.999%, Sigma Aldrich).

For thin films prepared by electrodeposition/surface treatment, the following materials were used without additional purification: Nickel (II) chloride hexahydrate (99.95 %, Alfa Aesar), D-(−)-tartaric acid (99 %, Alfa Aesar), thioacetamide (98 %, Alfa Aesar), ammonium hydroxide solution, 28 % in H_2O (≥99.99 %, Sigma-Aldrich), selenium dioxide (99.999 %, Sigma-Aldrich), sodium acetate (99.997 %, Alfa Aesar), sodium perchlorate (99.99 %, Sigma-Aldrich), cobalt (II) sulfate heptahydrate (99.999 %, Strem Chemicals), nickel (II) sulfate hexahydrate (99.99 %, Strem Chemicals), sodium tetraborate, anhydrous (99.998 %, Strem Chemicals), perchloric acid (99.999 %, Sigma-Aldrich), sodium hydroxide (99.99 %, Sigma-Aldrich), gold (III) chloride trihydrate (99.9%, Sigma-Aldrich), hydrochloric acid (conc., AR Select Plus grade, Macron Fine Chemicals), copper (II) sulfate pentahydrate (99.999 %, Strem), sulfuric acid (Omnipur Grade, EMD Millipore), and potassium hydroxide (99.99 % semiconductor grade, Sigma Aldrich).

All aqueous electrolyte solutions and water washings were performed with reagent grade deionized water (Millipore Type 1, 18MΩ-cm resistivity).

The following materials were fabricated via E-beam evaporation to generate planar thin films. From Kurt J. Lesker: Al (99.999 %), Pd (99.95 %), Pt (99.99 %), Cr (99.998 %), Mo (99.95 %), Fe (99.95 %), Ni (99.995 %), $Ni_{0.8}Fe_{0.2}$ (permalloy), Ta (99.95 %), Ti (99.995 %). From R. D. Mathis Company: Ag (99.999 %). From Ted Pella Inc.: Graphite rods, Grade 1 (3/16" x 12").

RuO_2 thin films were prepared by reactive oxygen sputtering using a Ru (99.95 %, 2" diameter and 1/8" thick (Kurt J. Lesker)) sputter target.

General electrochemical methods for DLC measurements. Experiments were conducted using a Gamry Reference 600 potentiostat. Unless otherwise specified, all electrochemical measurements were performed in a 3-electrode setup with a high surface area Pt-mesh counter electrode (Alfa Aesar, 99.997%) separated from the working compartment by a porous glass frit. Non-aqueous electrochemical double layer capacitance measurements were conducted using a pseudo-reference electrode consisting of Ag/AgCl wire bathed in 0.15 M TBA-PF_6 / CH_3CN solution and separated from solution by a Vycor frit (non-aqueous Ag reference, CH Instruments). The Ag/AgCl wire was fabricated by treating Ag wires with bleach and rinsing with copious amounts of deionized H_2O. All non-aqueous potentials are reported versus this pseudo-reference electrode. Aqueous electrochemical measurements for measuring double layer capacitance were conducted using a double junction Hg/Hg_2SO_4 reference (saturated KCl solution, CH151, CH Instruments), and potentials are reported in V vs RHE using the following conversion: $E(RHE) = E(Hg/Hg_2SO_4) + 0.654\ V + 0.059(pH)$. All experiments were performed at ambient temperature, (21 ± 1 °C). Working electrodes were prepared by contacting the films with Ti wire current collectors affixed to the electrodes by wrapping with Parafilm. The geometric areas of the exposed portion of the films were measured to convert AFM roughness measurements into real electrode surface areas. For the aqueous

electrodeposition of NiS_x, $NiSe_x$, and $CoSe_x$ films, Ag/AgCl (sat. NaCl, CH Instruments) reference electrodes were used.

Non-aqueous DLC measurements were performed in a 5-neck glass cell inside a N_2 glovebox to minimize the effects of moisture and O_2 on the measurements. Aqueous DLC measurements were also performed in a 5 neck glass cell with electrolyte solutions sparged with inert N_2 or Ar prior to each measurement to prevent convolution from O_2 reduction.

When measuring the DLC, it is critical to ensure that the CV sampling mode accurately measures the total capacitive current. CVs are implemented in modern, digital potentiostats as a series of incremental potential steps, rather than as a true analog linear sweep. Thus, current sampling modes that record the current at a single point during a potential step will not accurately reflect the true DLC, since the capacitive current decays over time during each potential step. Instead, currents should be sampled and integrated throughout the entire duration of each potential step during the CV scan in order to capture the entire capacitive response. On the Gamry potentiostat used in this study, the appropriate CV sampling mode corresponds to the "surface" mode, which was used to record all capacitance measurements in this work.

Synthesis of evaporated metal films. Pd, Pt, Cr, Mo, Fe, Ni, $Ni_{0.8}Fe_{0.2}$, Ta, Ti, and graphite films were synthesized by electron beam evaporation using an AJA ATC-2036 e-beam evaporator. 150-200 nm films were deposited (1-2 Å/s) on Ti-coated glass substrates which were cleaned thoroughly with ethanol and water prior to insertion into the deposition chamber. RuO_2 films were deposited by reactive O_2 RF sputter deposition using a Ru target. Sputter deposition was performed using an AJA ATC Orion 5 Sputtering System with a chamber pressure of 3 mtorr, Ar flow rate of 8 sccm, O_2 flow rate of 2 sccm, substrate temperature of 300 °C, and 125 W of power. These conditions led to a deposition rate of 127 Å/s, which was used to generate 300 nm thick RuO_2 films.

Layer by layer nickel selenide film preparation.[25,26] Nickel selenide thin films were prepared by sequential underpotential deposition of selenium and nickel adlayers in a flow cell configuration using an automated system (Electrochemical ALD Inc). Gold coated glass slide substrates were initially cleaned by electrochemical cycling in 0.5 M $HClO_4$ between −0.25 and 1.85 V vs RHE at 50 mV s^{-1}. The electrodes were then rinsed with MilliQ water. Selenium was initially deposited by flowing an electrolyte solution consisting of 5 mM SeO_2, 50 mM sodium acetate, 0.1 M $NaClO_4$ (pH 5.0) over the working electrode for 15 seconds. Subsequently, solution flow was paused and the working electrode was polarized at −0.3 V vs Ag/AgCl (0.2 V vs RHE) for 1 min. This served to produce a sub-monolayer of selenium on the gold surface. Immediately following electrodeposition, milliQ water was flowed over the electrode for 20 seconds. A Ni adlayer was then deposited on the selenidized gold electrode by flowing an electrolyte solution consisting of 5 mM $NiSO_4$, 10 mM $Na_2B_4O_7$, 0.1 M $NaClO_4$ (pH 6.7) over the working electrode for 10 seconds. Subsequently, solution flow was paused and the working electrode was polarized at −0.6 V vs Ag/AgCl (0.0 V vs RHE) for 1 min. Immediately following electrodeposition, milliQ water was flowed over the electrode for 20 seconds. The process was repeated for 50 cycles in order to build up films of desired thickness. In all cases, the sequence of layer-by-layer depositions concluded with deposition of a Ni adlayer.

Layer by layer cobalt selenide film preparation.[27] Cobalt selenide thin films were prepared by sequential underpotential deposition of selenium and cobalt adlayers in a flow cell configuration using an automated system (Electrochemical ALD Inc), similar to the nickel selenide layer preparation. Gold coated glass slide substrates were initially cleaned by electrochemical cycling in 0.5 M $HClO_4$ between −0.25 and 1.85 V vs RHE at 50 mV s^{-1}. The electrodes were then rinsed with MilliQ water. Selenium was initially deposited by flowing an

electrolyte solution consisting of 5 mM SeO_2, 50 mM sodium acetate, 0.1 M $NaClO_4$ (pH 5.0) over the working electrode for 15 seconds. Subsequently, solution flow was paused and the working electrode was polarized at −0.3 V vs Ag/AgCl (0.2 V vs RHE) for 1 min. This served to produce a sub-monolayer of selenium on the gold surface. Immediately following electrodeposition, milliQ water was flowed over the electrode for 20 seconds. A Co adlayer was then deposited on the selenidized gold electrode by flowing an electrolyte solution consisting of 5 mM $CoSO_4$, 10 mM $Na_2B_4O_7$, 0.1 M $NaClO_4$ (pH 6.7) over the working electrode for 10 seconds. Subsequently, solution flow was paused and the working electrode was polarized at −0.6 V vs Ag/AgCl (0.0 V vs RHE) for 1 min. Immediately following electrodeposition, milliQ water was flowed over the electrode for 20 seconds. The process was repeated for 50 cycles in order to build up films of the desired thickness. In all cases, the sequence of layer-by-layer depositions concluded with deposition of a Co adlayer.

Electrodeposition to prepare NiS films[28]. 50 ml of 0.1 M $NiCl_2 \cdot 6H_2O$ solution was mixed with 10 ml of 0.1 M aqueous solution of D-(-)-tartaric acid and stirred for 20 minutes. Then, 25 mL of 0.1 M thioacetamide solution was added and stirred for 10 minutes. The final volume of the solution was adjusted to 100 mL with water. The pH of this working solution was maintained at 5.5 by adding 28% ammonium hydroxide solution. A polished Au RDE was used as the substrate and working electrode. The counter electrode was a Pt mesh and the reference electrode was Ag/AgCl. Consecutive cyclic voltammetry scans from −0.38 to 0.72 V vs RHE were performed at a scan rate of 5 mV/s. During the deposition, the working electrode was rotated at 600 rpm and the solution was continuously bubbled with N_2. After 10 cycles, the Au RDE working electrode was removed from the deposition bath, gently washed with copious water, and dried in air.

Scanning electron microscopy (SEM). Following synthesis, the films were imaged

top down using a Zeiss Merlin field emission-SEM with acceleration voltages of 2-5 keV, and using the in-lens mode to produce the images shown in the SI.

Atomic force microscopy (AFM). The surface roughnesses of all fabricated planar electrodes were determined using AFM measurements recorded in tapping mode using a Dimension 3100 AFM with a Nanoscope V controller. Typically, a 2×2 μm^2 area for each electrode was sampled for roughness factor (RF) determination. The surface areas of the electrodes were taken directly from the software output, which are calculated as the sum of the areas of "triangles" formed by sets of 3 consecutive AFM height measurement points. This surface area is divided by the projected area (geometric area) of the electrode to derive RFs. Sigma-Aldrich BudgetSensors Si tipped, Al reflex-coated, AFM tips were used for all AFM measurements. These measurements were used to estimate the real surface area for each electrode using the following equation.

$$\text{area}_{\text{real}} = \text{RF} \times \text{area}_{\text{geometric}} \qquad \text{(Eq. S1)}$$

X-ray photoelectron spectroscopy (XPS). XPS spectra were recorded using a PHI Versaprobe II XPS with a monochromated Al (1486.6 eV at 45.6 W) X-ray source and a beam diameter of 200.0 μm. The pass energy of the measurement was 187.85 eV. These parameters were used to generate the survey spectra in the SI.

Synthesis and electrochemical characterization of $NiFeO_x$. $Ni_{0.8}Fe_{0.2}$ (permalloy) films prepared by e-beam evaporation (see above) were oxidized and activated following modified literature preparation steps[21,22]. First, samples were electrochemically cycled between 1.2 to 1.6 V vs RHE in 1 M KOH solution using a Pt mesh counter electrode and a Hg/HgO/1M KOH reference electrode to track changes in electrode activity upon forming a layered $Ni_xFe_{(1-x)}OOH$ oxygen evolution catalyst surface (Figure 2.11). Following CV cycling, the films were

soaked in 1 M aqueous KOH at 40 °C for 8 minutes, then washed copiously with DI water and dried prior to an additional CV sweep to establish the final activity. The surface areas of these activated electrodes were determined by AFM as described above (raw AFM traces are shown below). Subsequently, DLC values were measured in both aqueous and non-aqueous electrolyte using the procedures described above, and these values, taken together with the AFM derived real surface areas, were used to calculate the specific capacitance values reported in Figure 2. and Figure 2..

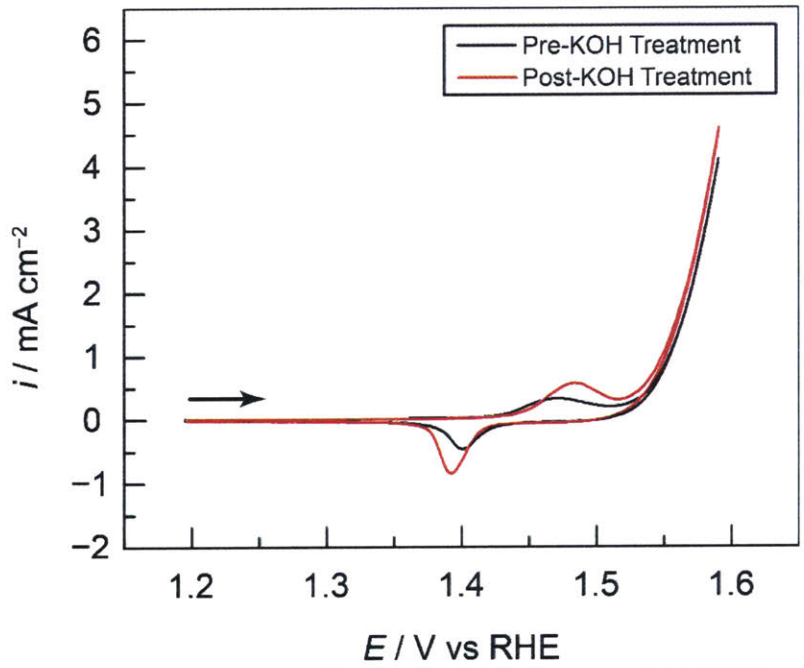

Figure 2.5. CV traces of $Ni_xFe_{1-x}OOH$ films recorded in aqueous 1 M KOH solution before (black) and after (red) activation in 1 M KOH at 40 °C. O_2 evolution catalysis onsets at ~1.5 V (~0.3 V overpotential).

Electrolyte concentration dependence of specific capacitance. The specific capacitance of Au and Ni planar films were measured at the OCP in KPF_6 / CH_3CN electrolyte at electrolyte concentrations of 0.05, 0.1, and 0.15 M to produce the data in Figure 2..

Electrolyte dependent specific capacitance of "supercapacitor" materials. The specific capacitance of planar oxide-passivated Mo and RuO_2 films were measured in various electrolytes according to the procedures described above. Aqueous DLC measurements were

conducted in 0.15 M $NaClO_4$ electrolyte, whereas non-aqueous measurements were conducted in CH_3CN electrolyte baths containing either 0.15 M KPF_6 or 0.15 M $TBAPF_6$ (Figure 2.10).

AFM roughness of Au and Ti electrodes before and after non-aqueous DLC measurements in 0.15 M KPF_6 / CH_3CN electrolyte. AFM roughness measurements before and after non-aqueous DLC measurements of Au and Ti electrodes show little change in roughness as a result of the DLC measurement. This suggests that non-aqueous DLC does not significantly alter the surface roughness of both metal and oxide-passivated electrodes (Table 2.1).

Electrodeposition of rough Au films and characterization by Cu underpotential deposition (UPD). Experiments were conducted using a Gamry Reference 600 potentiostat. Rough Au films were synthesized following a modified literature preparation[1]. Au coated glass slides were used as substrates for Au deposition, and were contacted to Ti wires with Parafilm wrap to secure the connections. A Ag/AgCl (Edaq) electrode was used as the reference electrode and Au mesh was used as the counter electrode. Au electrodeposition was performed in solutions containing either 13, 26, or 40 mM $AuCl_3 \cdot 3H_2O$ in 0.5 M HCl aqueous electrolytes. The low roughness factor electrode was prepared by polarizing the planar Au substrate at −0.4 V vs Ag/AgCl for 160 s in the 13 mM Au electrolyte solution. The resulting nanostructured film yielded a non-aqueous DLC-derived electrode capacitance of 84.2 $\mu F/cm^2$. Dividing this value by the measured non-aqueous specific capacitance value of Au, 8.8 $\mu F/cm^2$, yields a real surface area of 9.6 cm^2 which corresponds to a roughness factor of 8.2. The medium roughness factor electrode was prepared by polarizing the planar Au substrate at −0.25 V vs Ag/AgCl for 500 s in the 26 mM Au electrolyte solution. This yielded a real DLC surface area of 24.9 cm^2, which corresponds to a roughness factor of 19.9. The high roughness factor electrode was prepared by polarizing the planar Au substrate at −0.4 V vs Ag/AgCl for 500 s in the 40 mM

Au electrolyte solution. The resulting nanostructured film yielded a non-aqueous DLC-derived electrode surface area of 41.1 cm^2, which corresponds to a roughness factor of 25.8.

Electroactive surface areas of all rough electrodeposited Au films were measured by copper underpotential deposition (UPD) using a modified literature method[4]. $Hg/HgSO_4$ was used as the reference electrode, and a high surface area Pt-mesh was used as the counter electrode. The electrodeposited Au films were cycled from 0.08 V to −0.33 V vs $Hg/HgSO_4$ at a scan rate of 50 mV/s in Ar-saturated 0.05 M H_2SO_4 containing 0.1 M $CuSO_4$. The broad anodic wave (Figure 2.) beginning at −0.32 V vs $Hg/HgSO_4$ was integrated to 0.00 V to obtain a stripping charge value, which was divided by the known specific stripping charge of Cu on Au[4], 0.46 mC/cm^2, to obtain the electroactive surface area values plotted on the y-axis of Figure 2.9. This protocol was used to collect the representative data shown in Figure 2..

SEM and AFM micrographs of planar electrodes

Ag

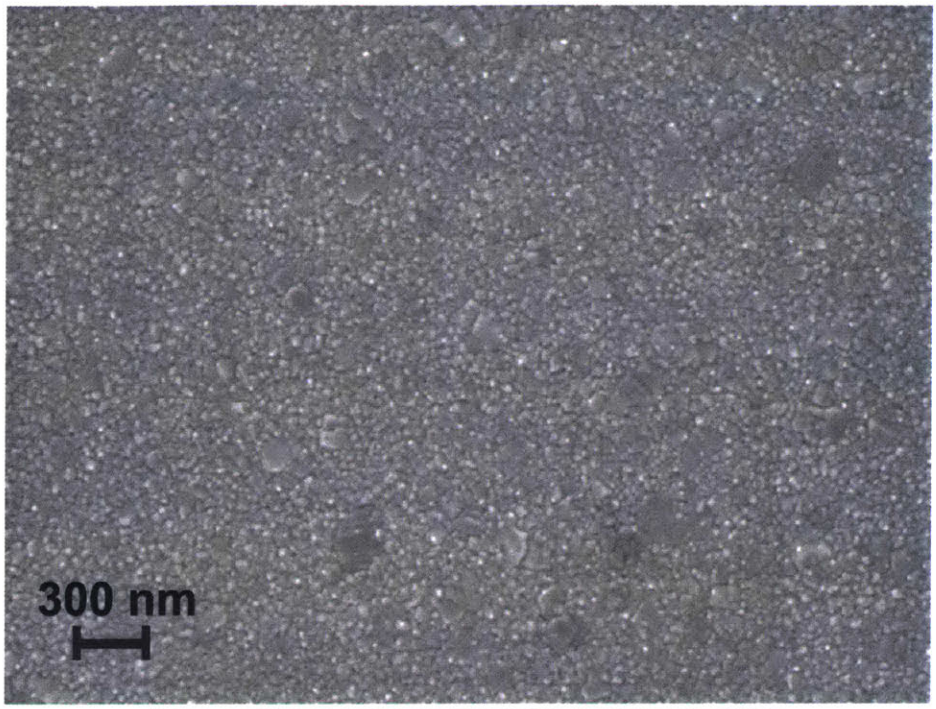

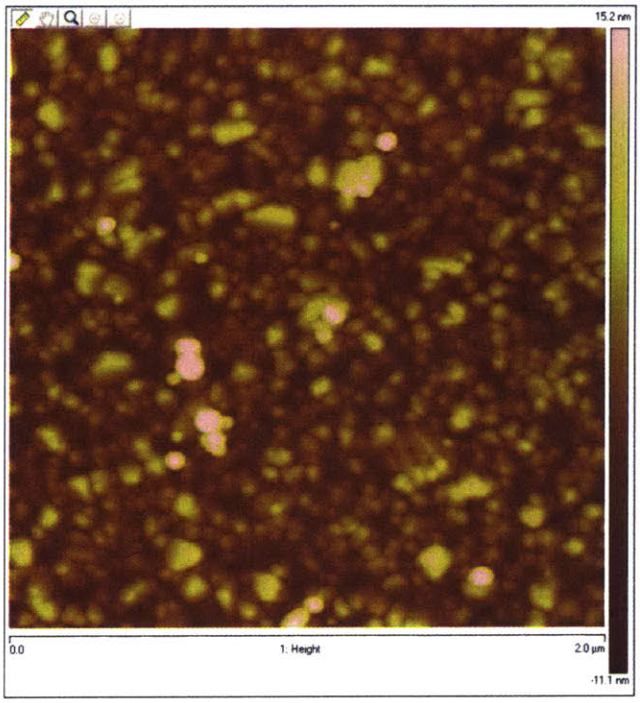

Au

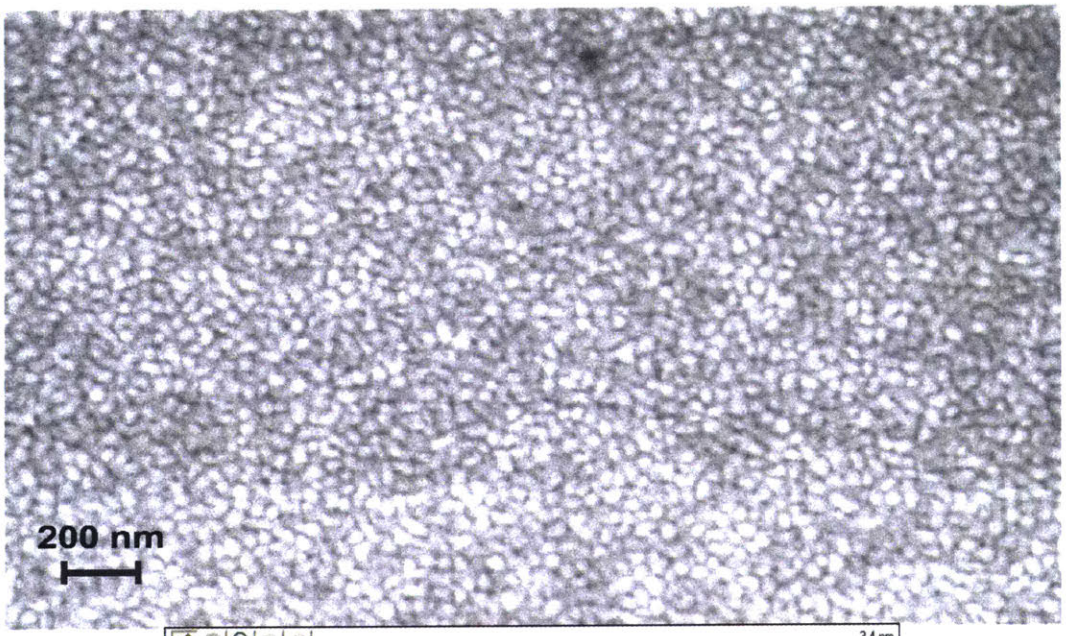

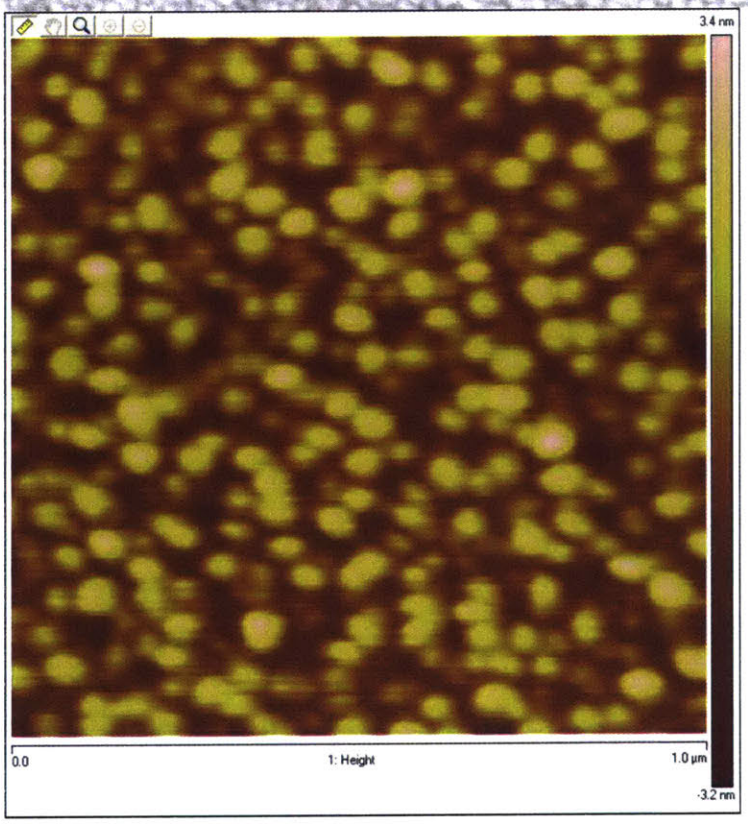

Pd

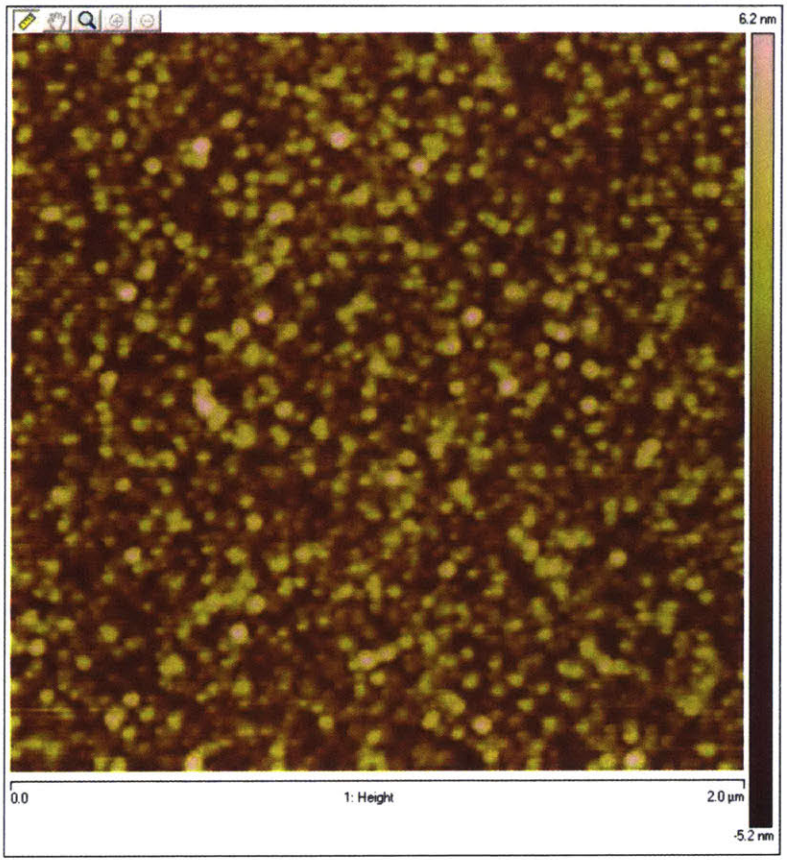

Pt

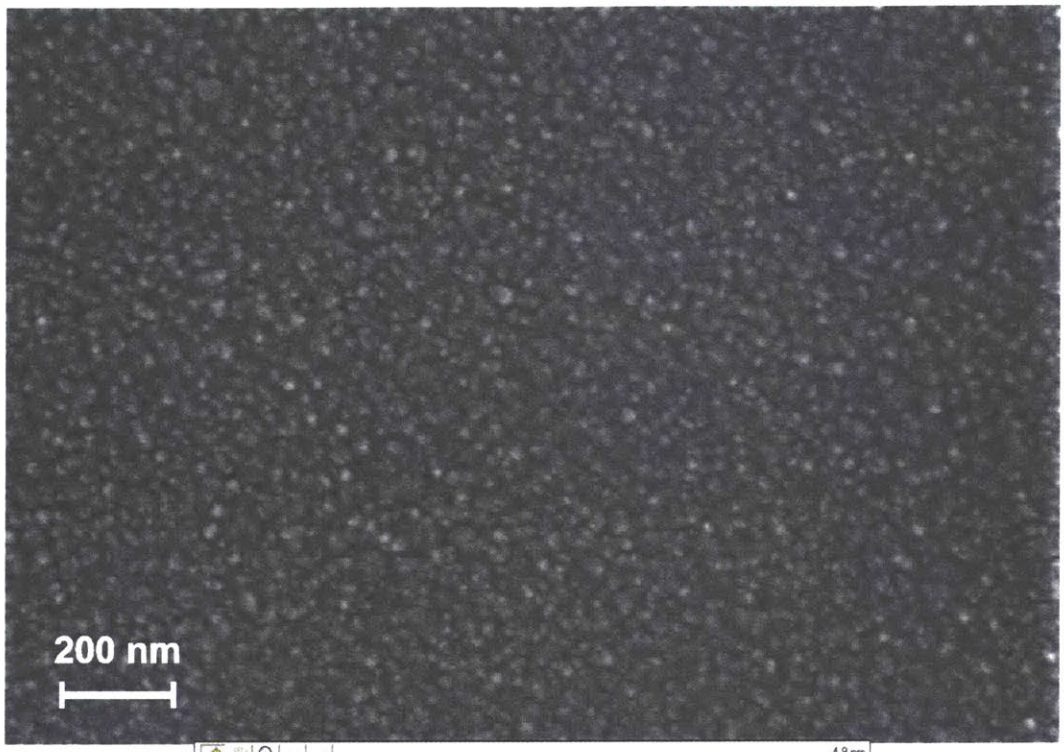

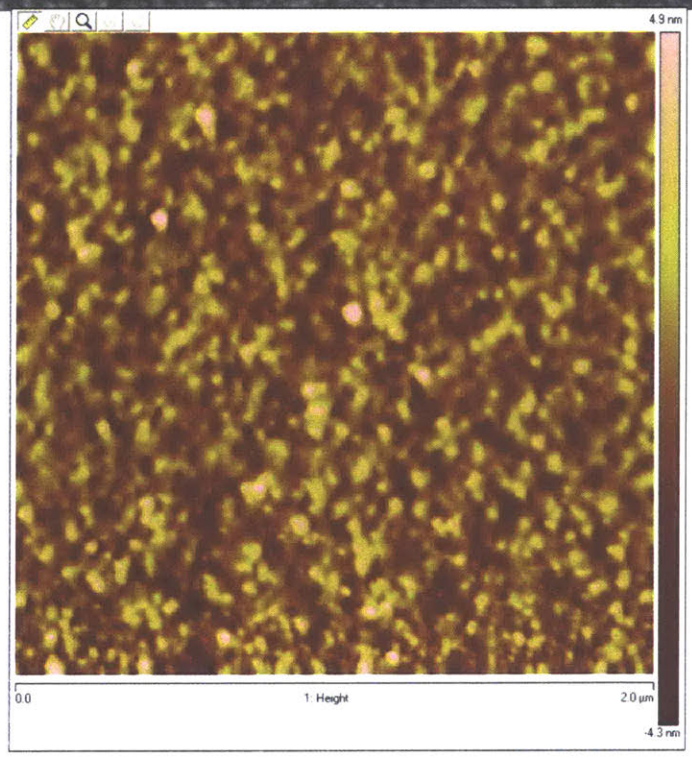

Oxide passivated Al

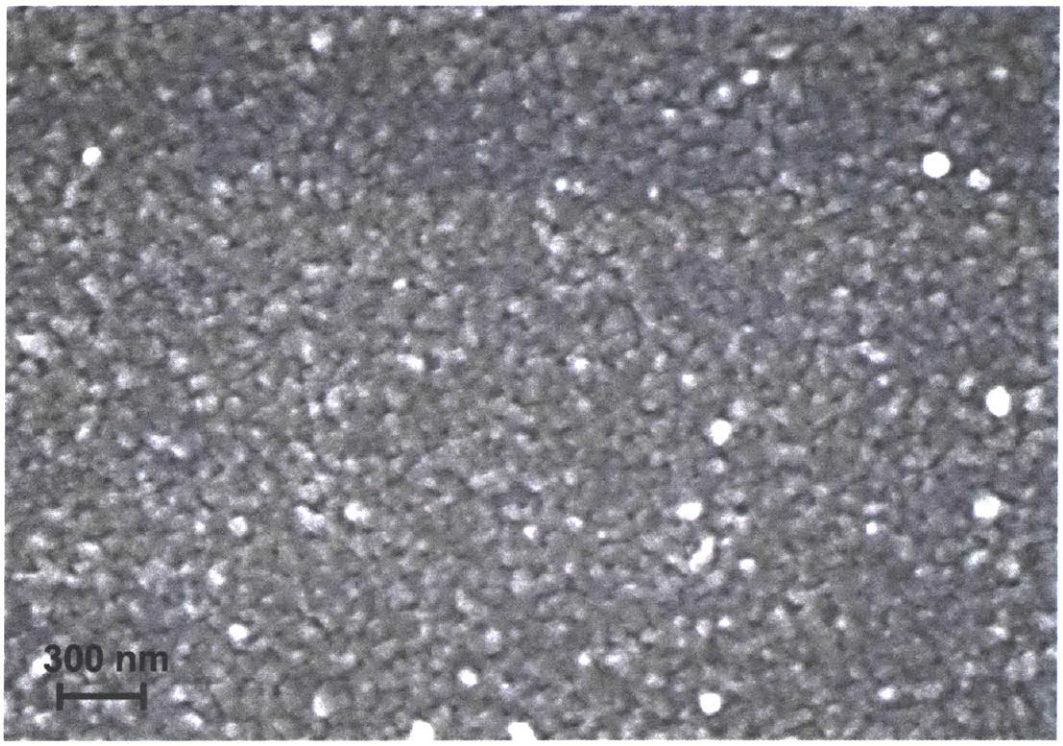

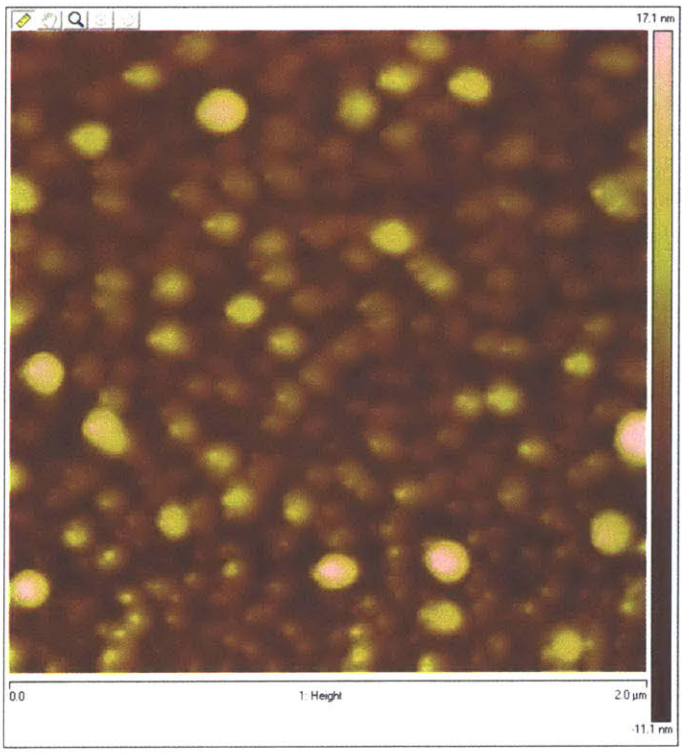

Oxide passivated Cr

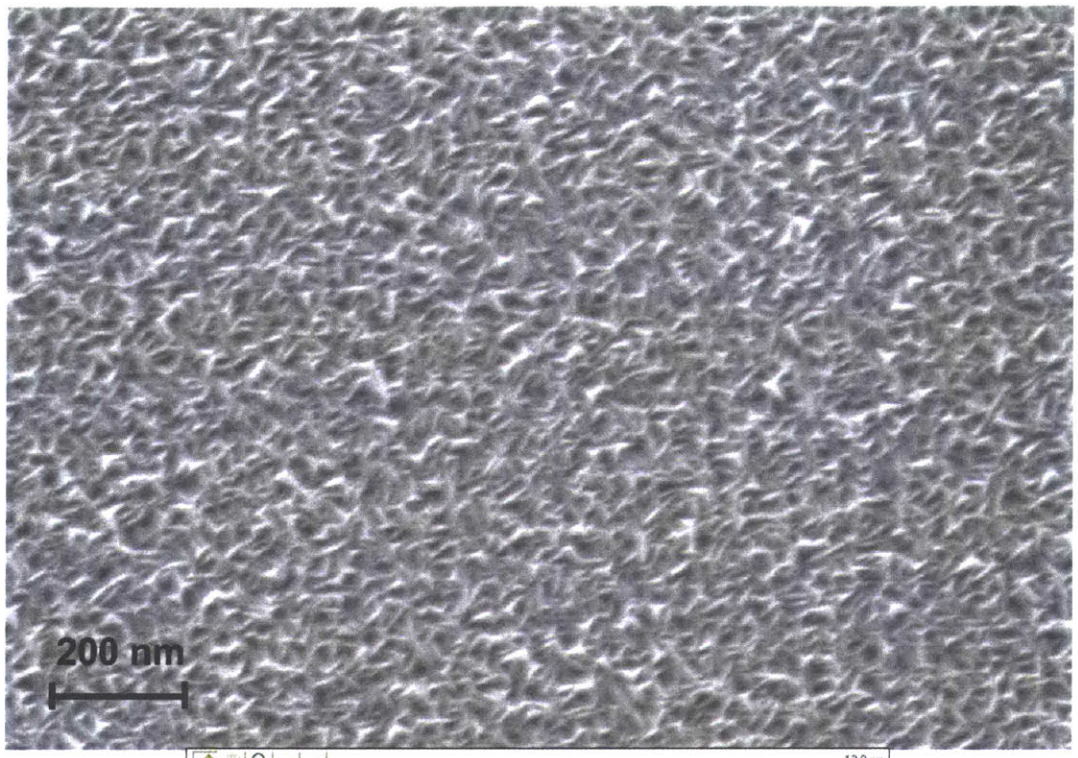

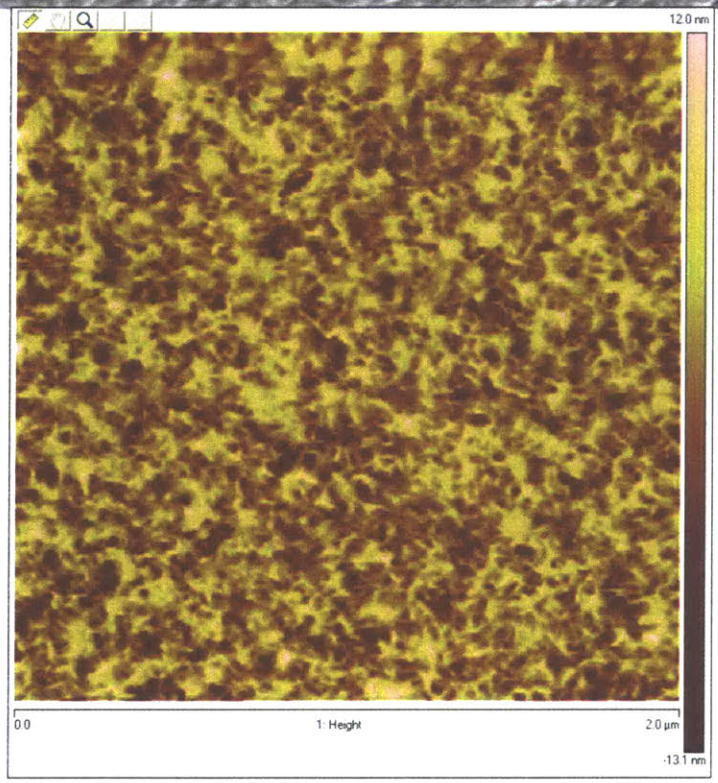

Oxide passivated Fe

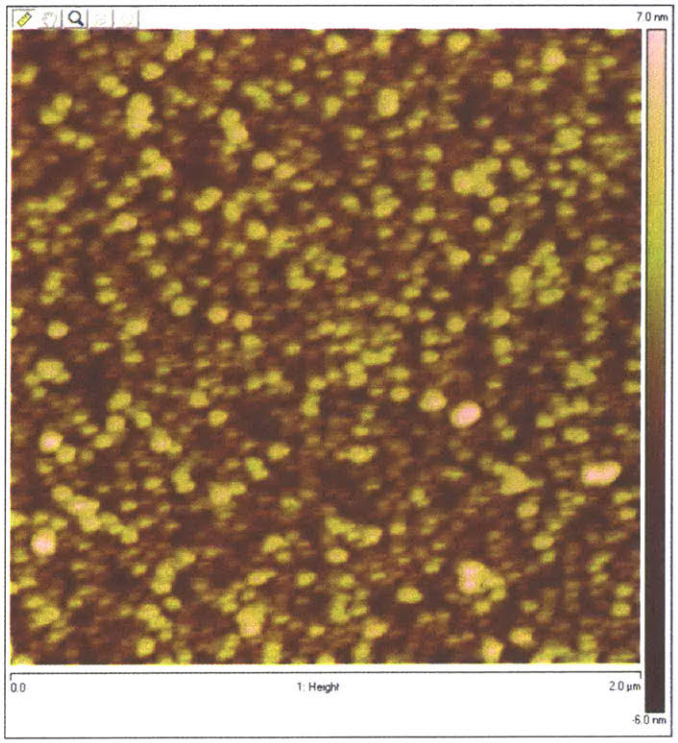

Fluorine doped tin oxide (FTO)

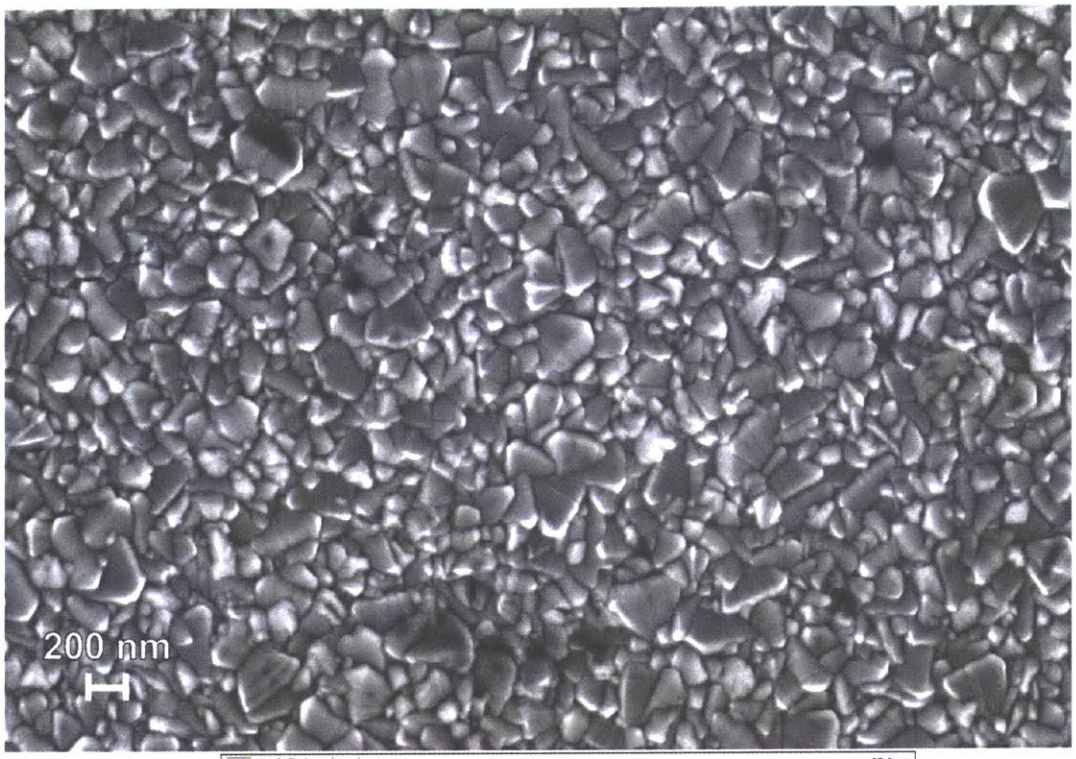

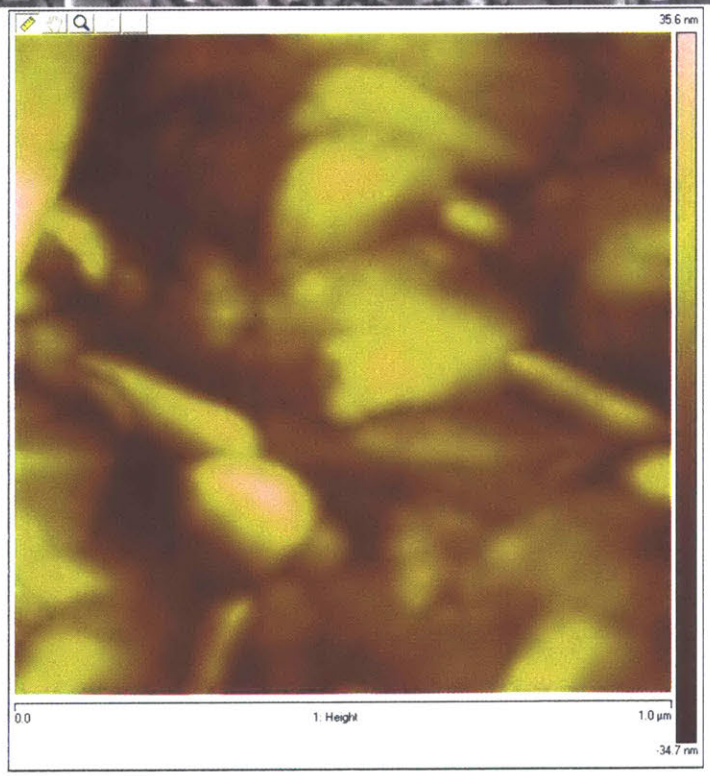

Oxide passivated Mo

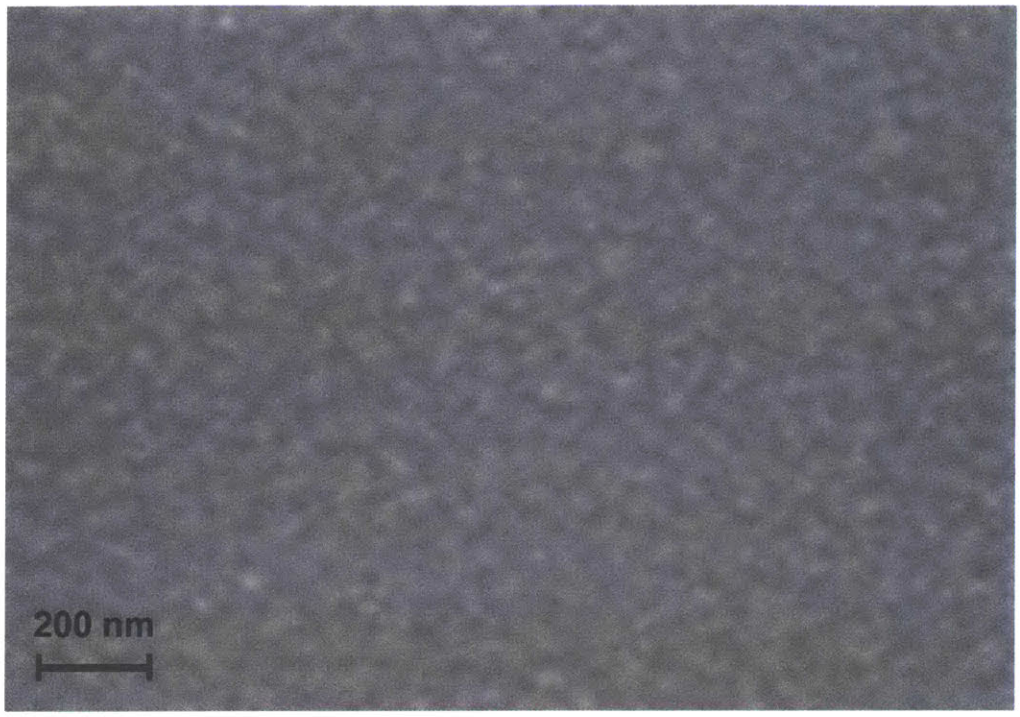

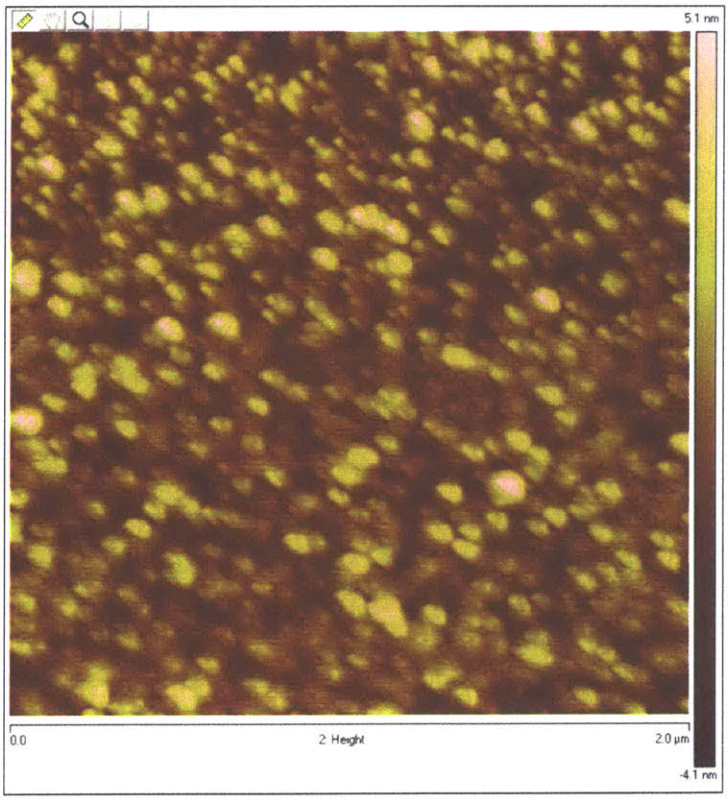

Oxide-passivated Ni

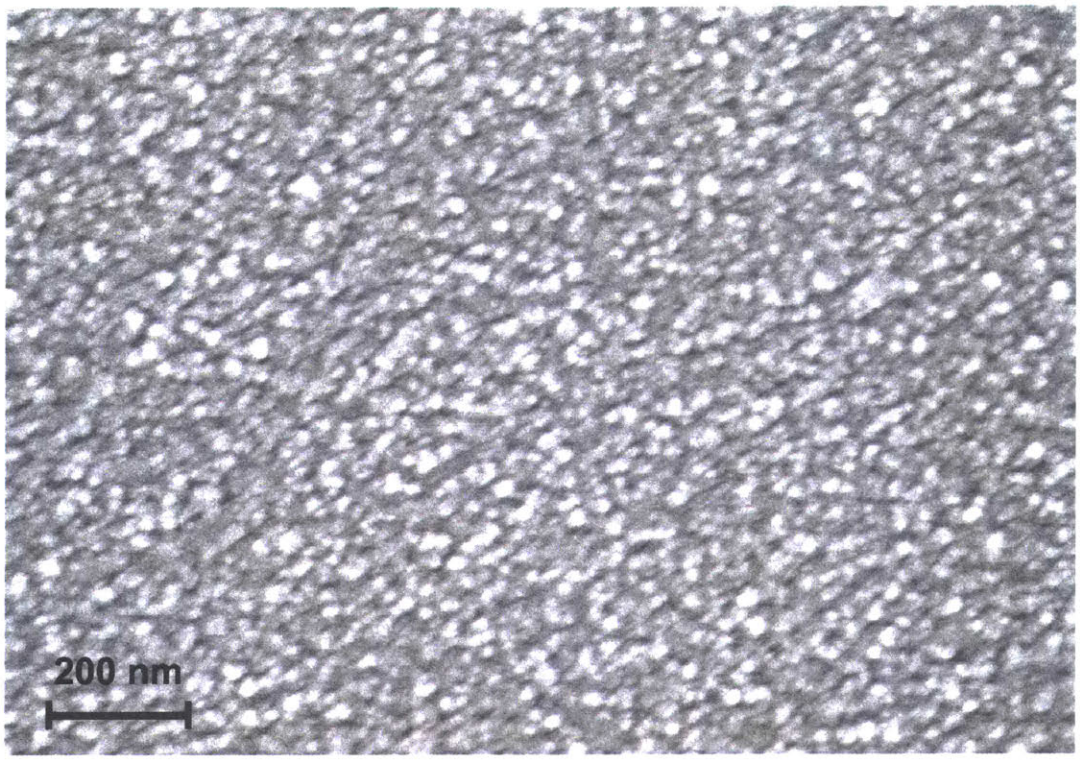

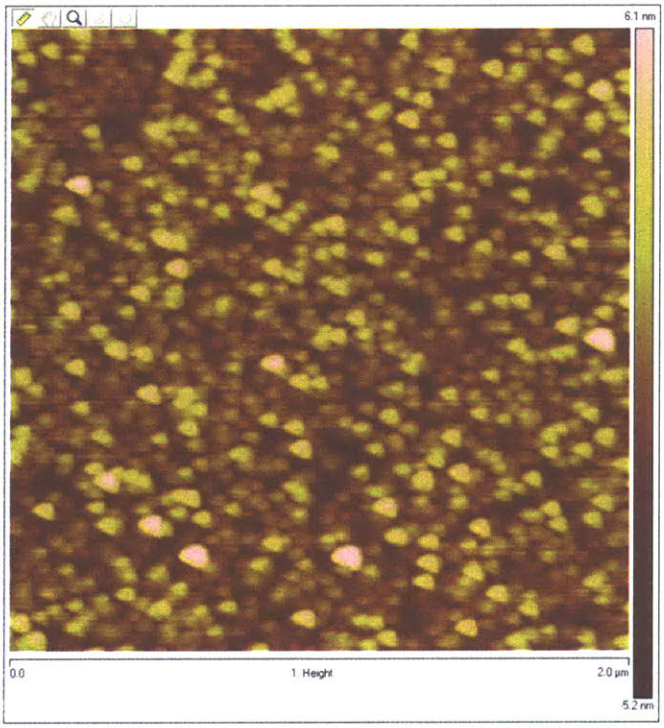

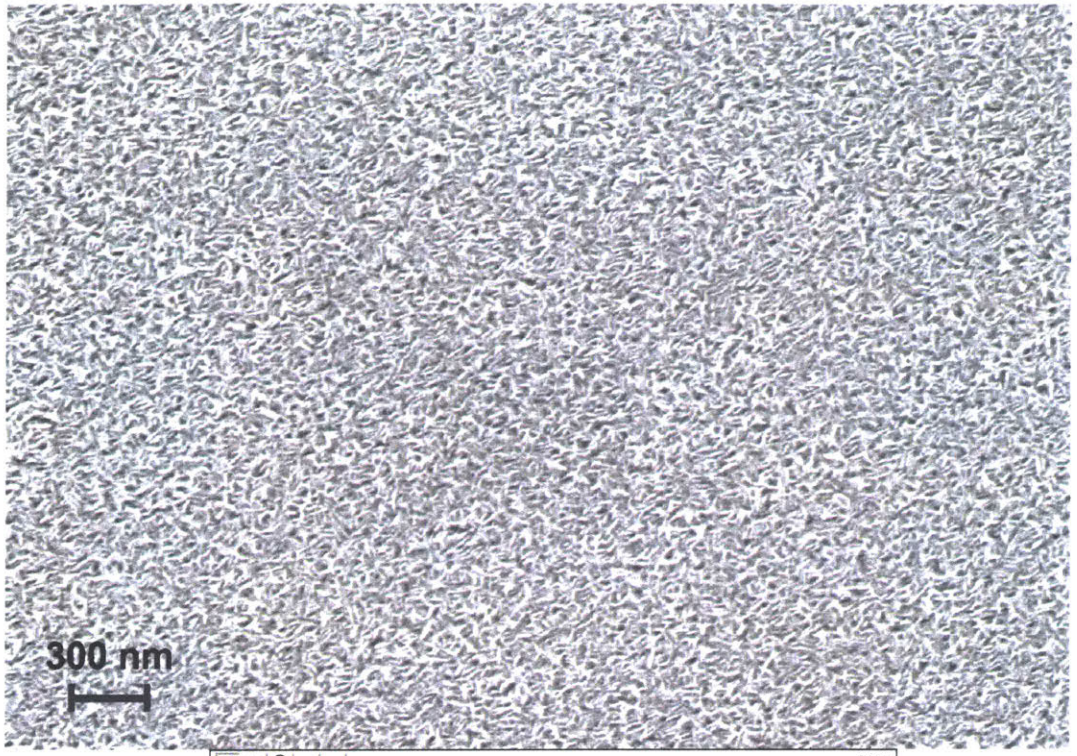
300 nm

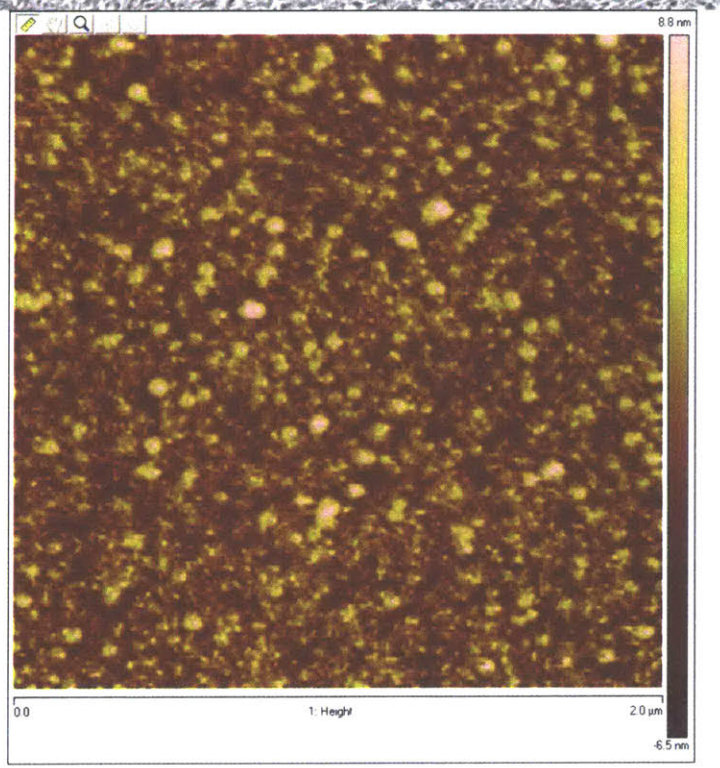
8.8 nm
0.0
1: Height
2.0 µm
-6.5 nm

$NiFeO_x$

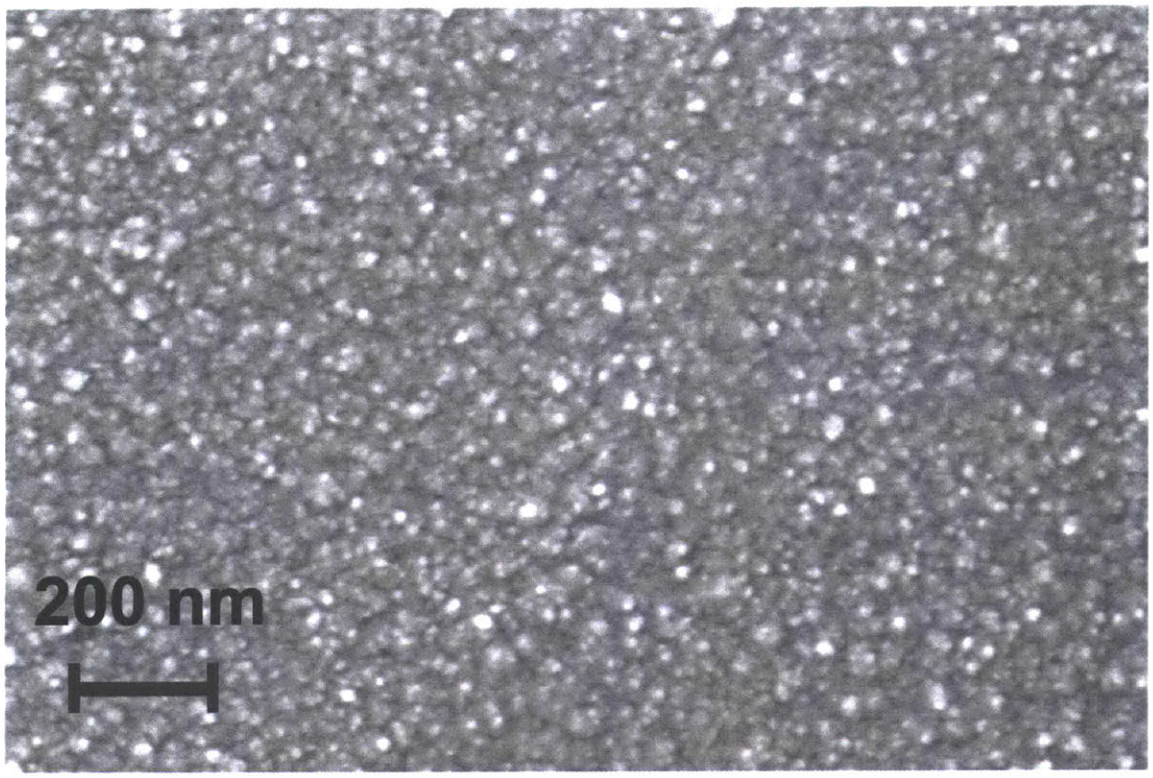

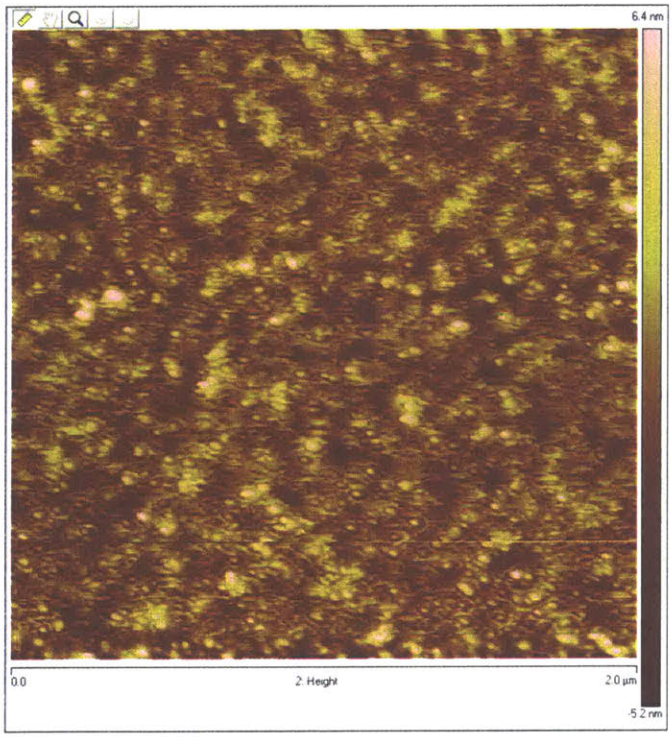

RuO_2

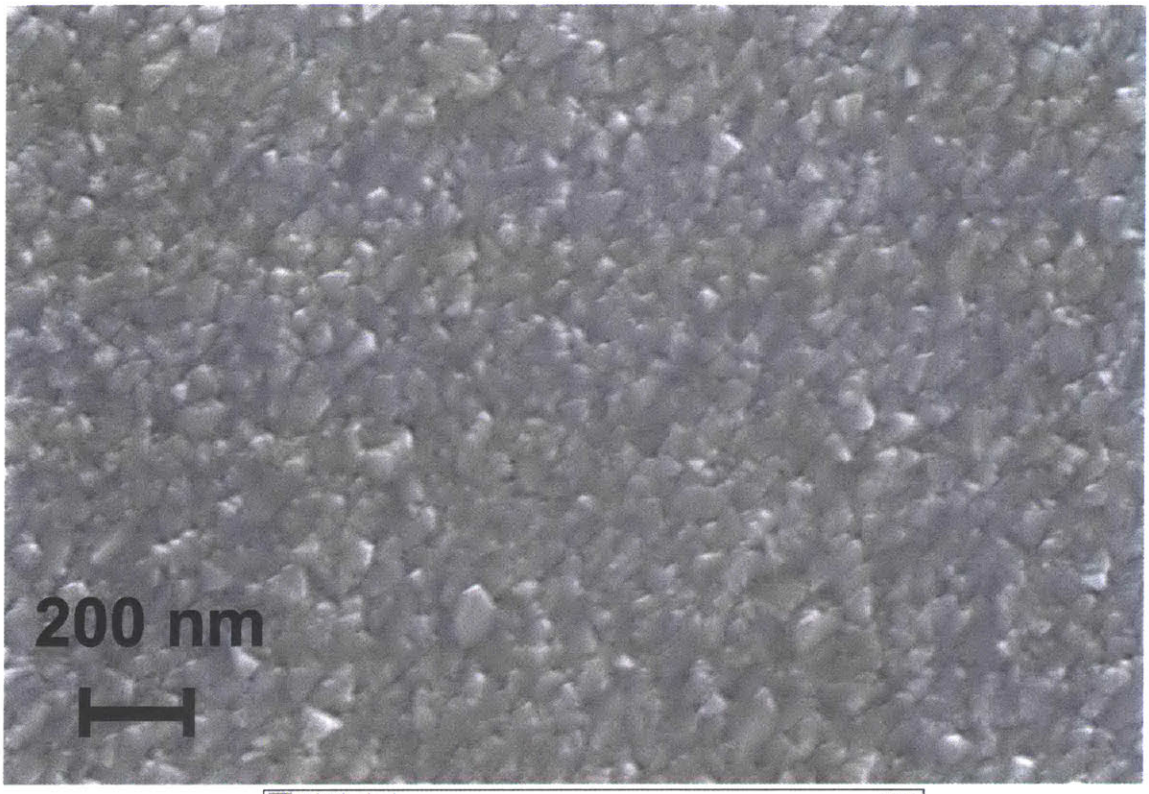

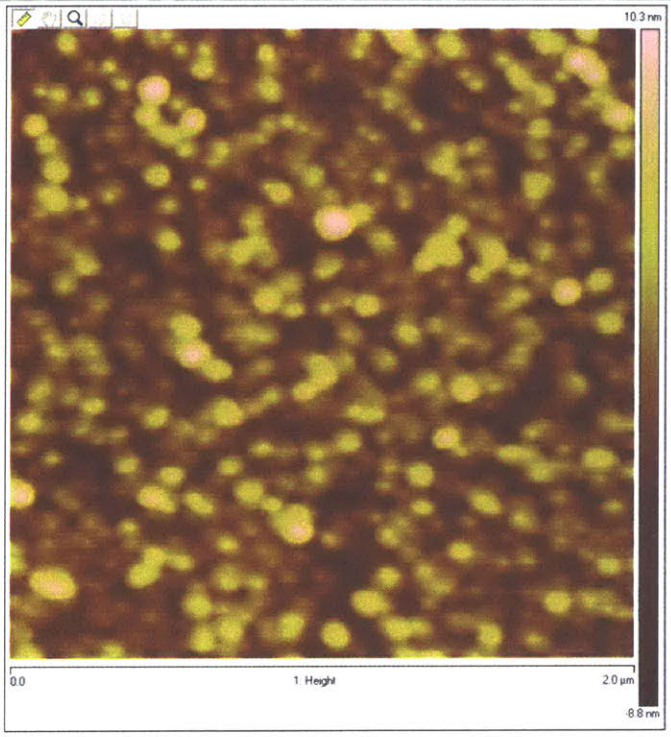

Oxide passivated Ta

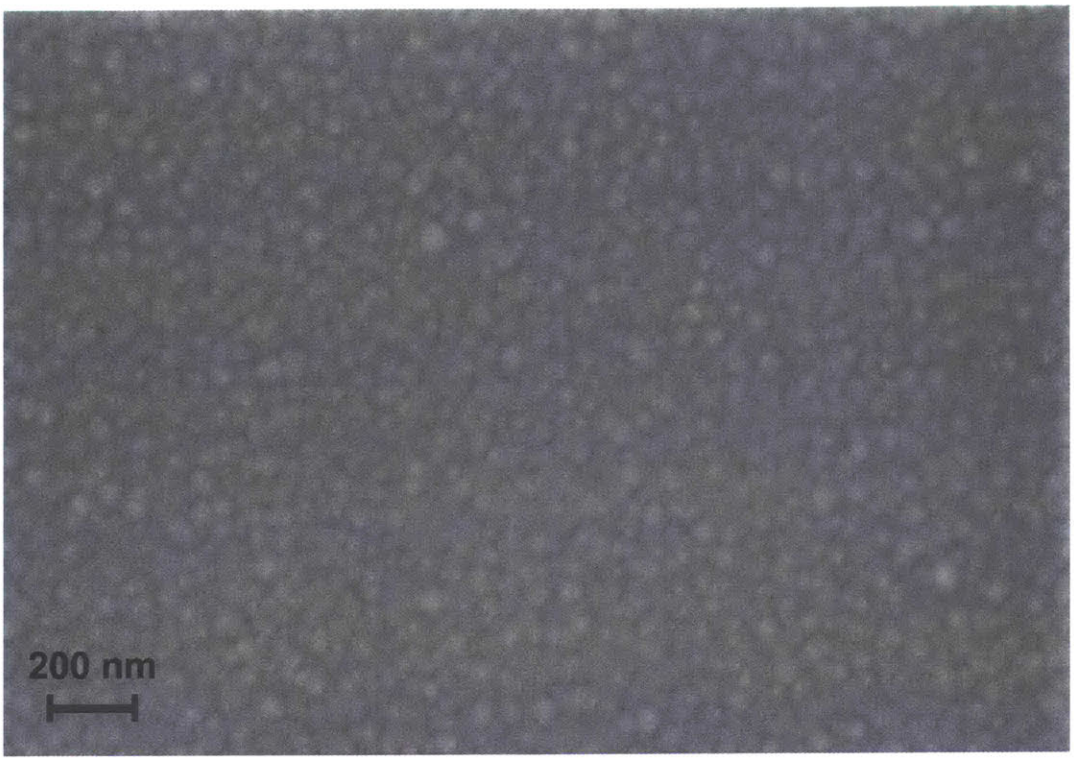

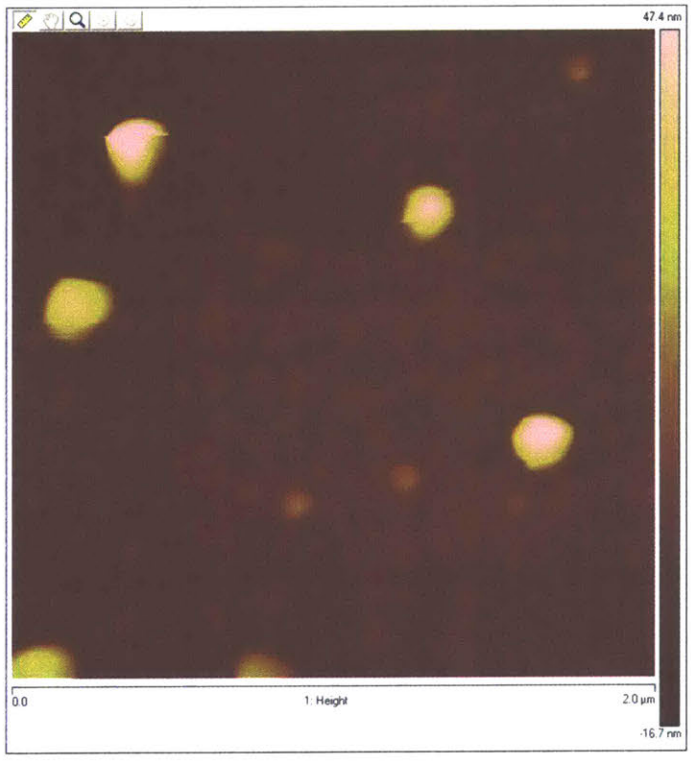

Oxide passivated Ti

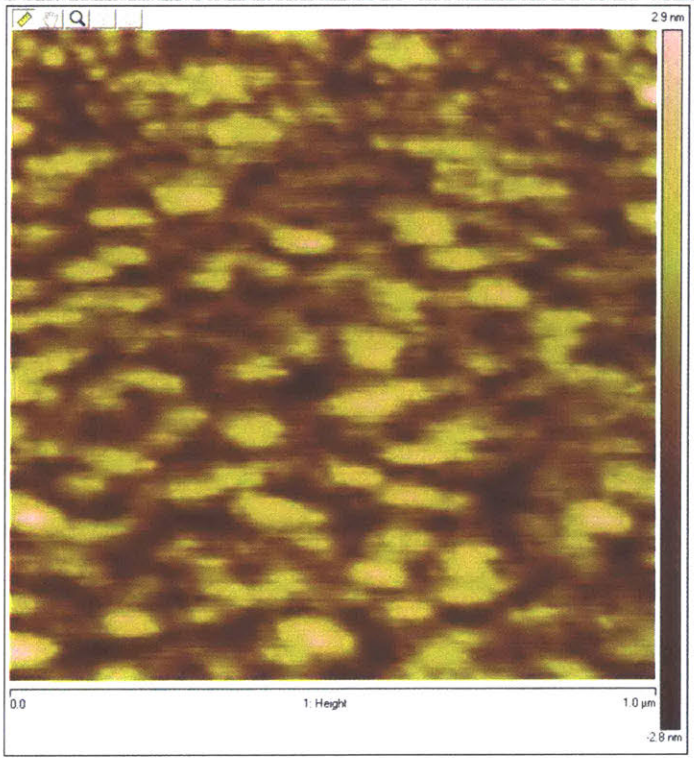

NiS_x

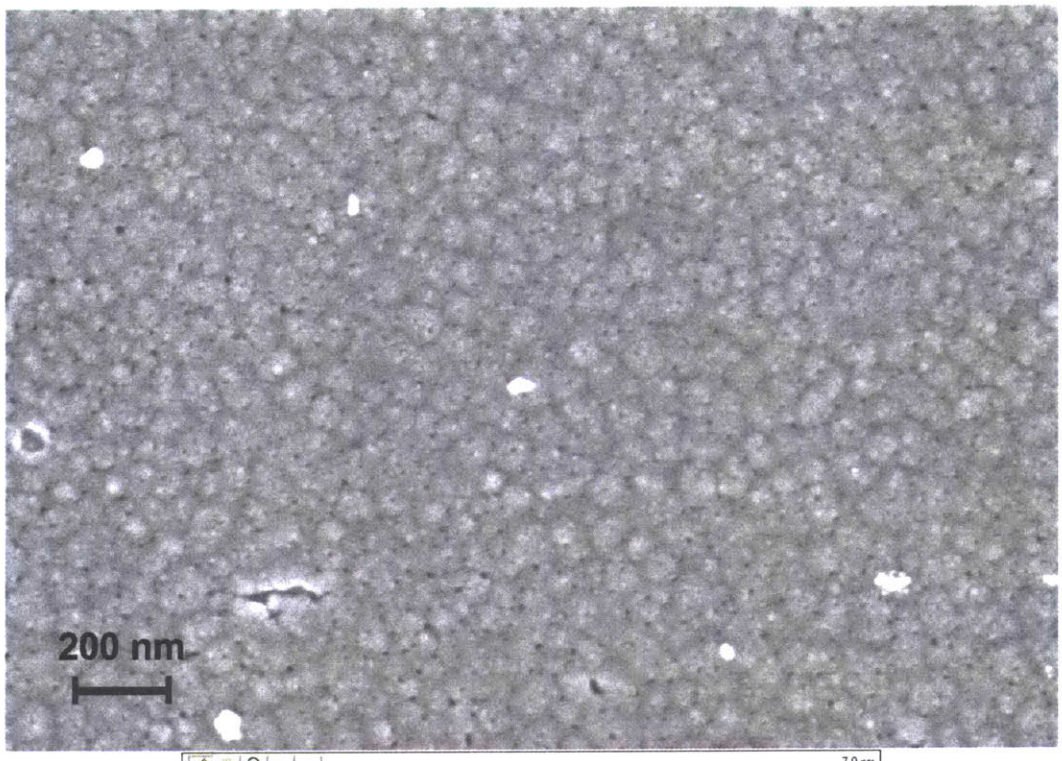

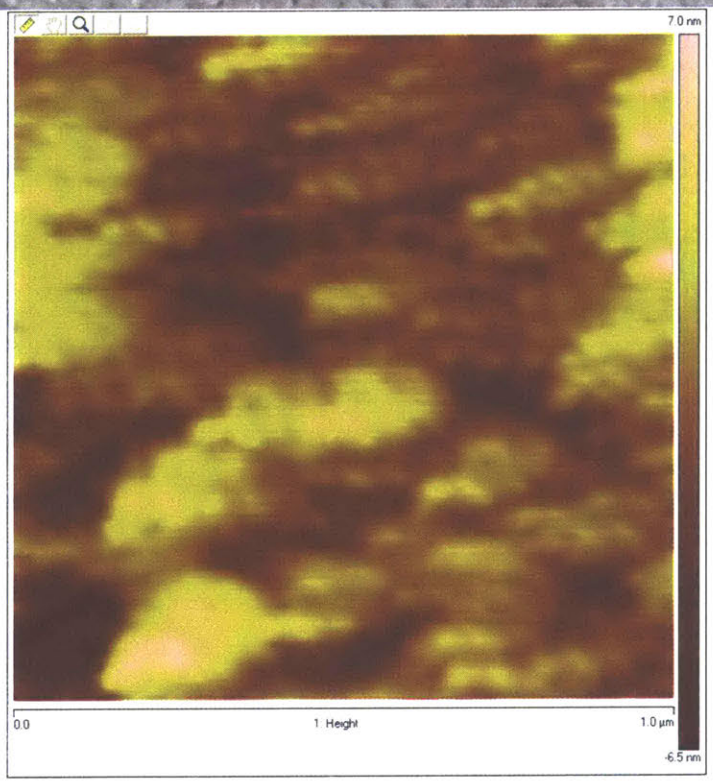

$CoSe_x$

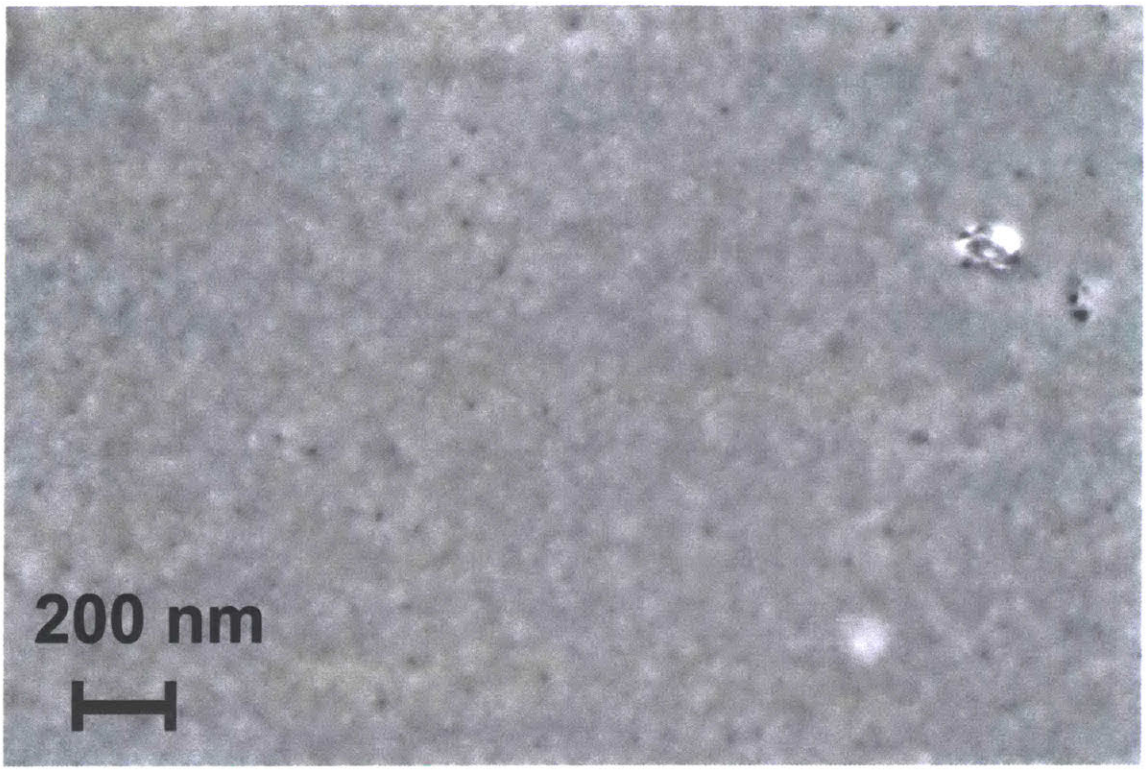

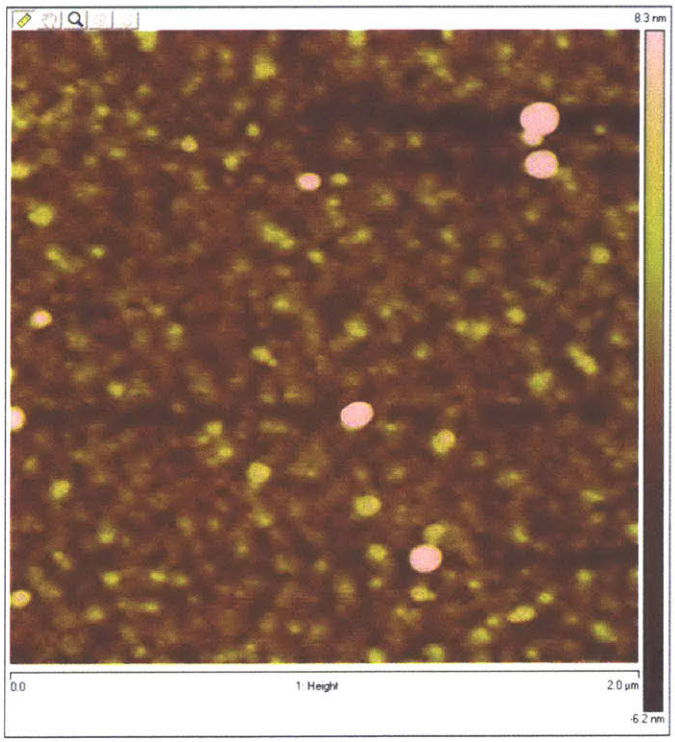

$NiSe_x$

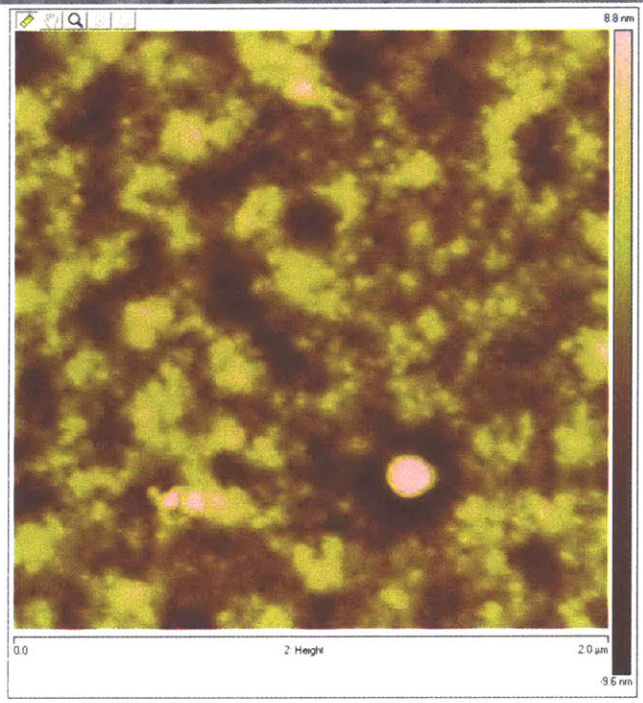

Graphitic C

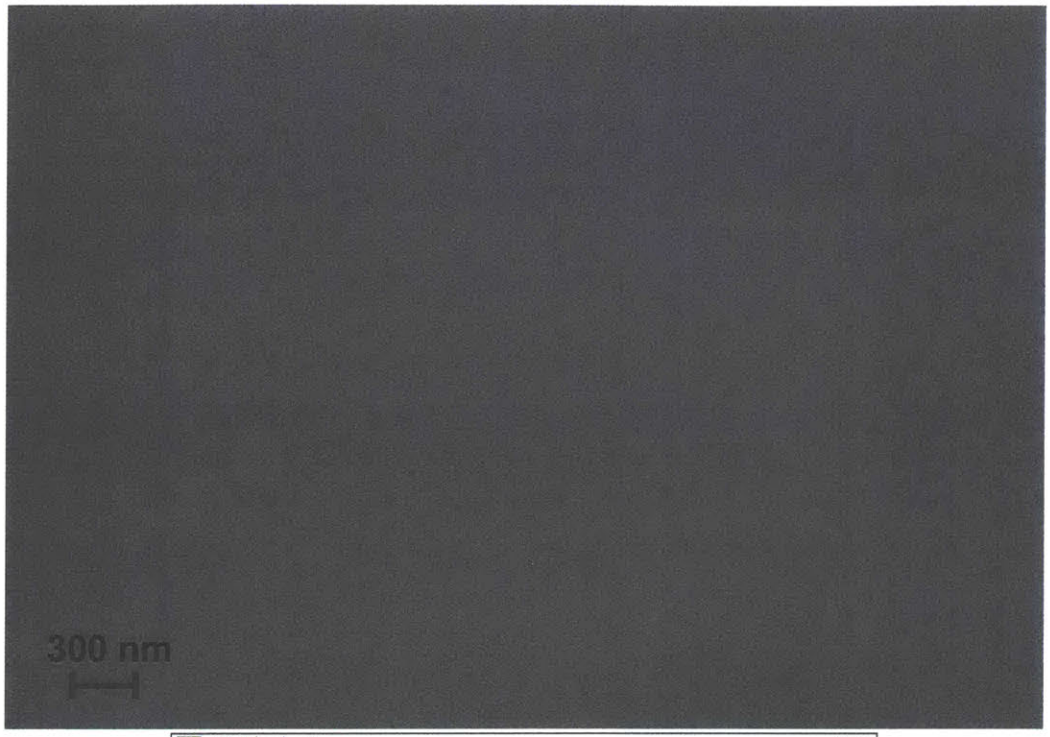

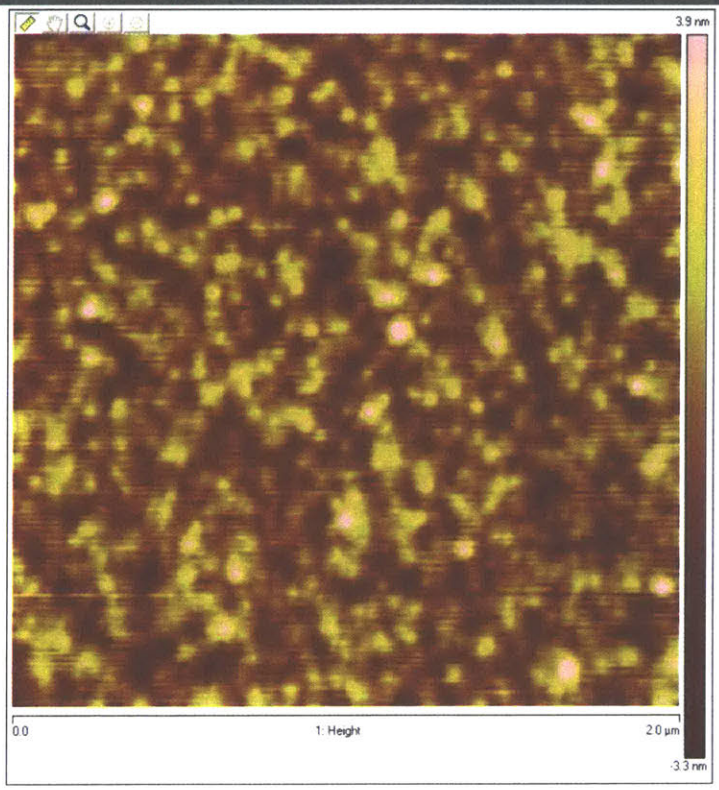

Survey XPS (Al source) spectra of as synthesized planar electrodes

Ag

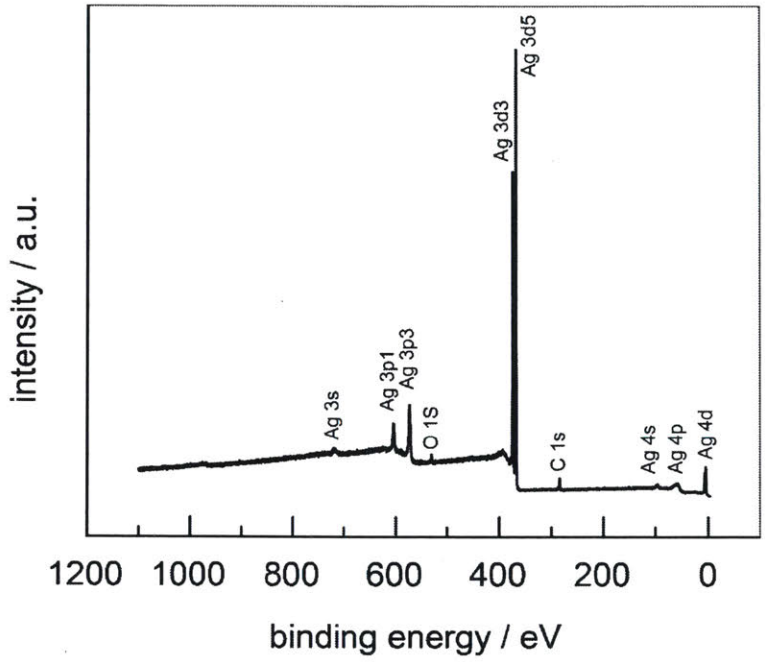

Au

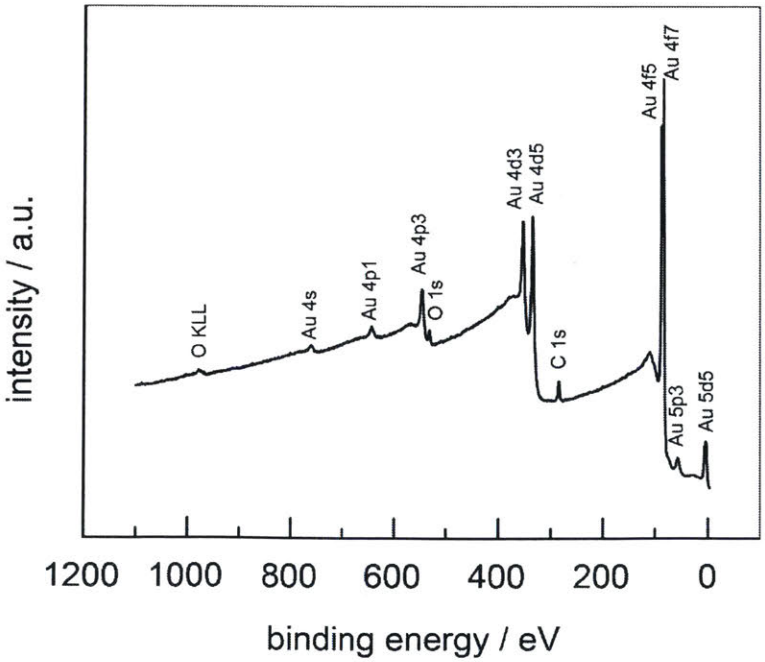

Pd

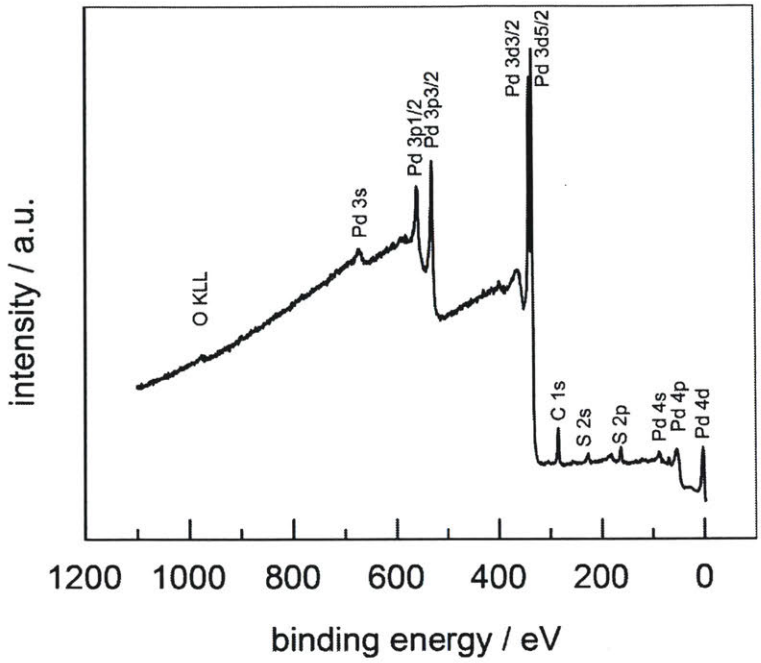
intensity / a.u.
O KLL
Pd 3s
Pd 3p1/2
Pd 3p3/2
Pd 3d3/2
Pd 3d5/2
C 1s
S 2s
S 2p
Pd 4s
Pd 4p
Pd 4d
1200 1000 800 600 400 200 0
binding energy / eV

Pt

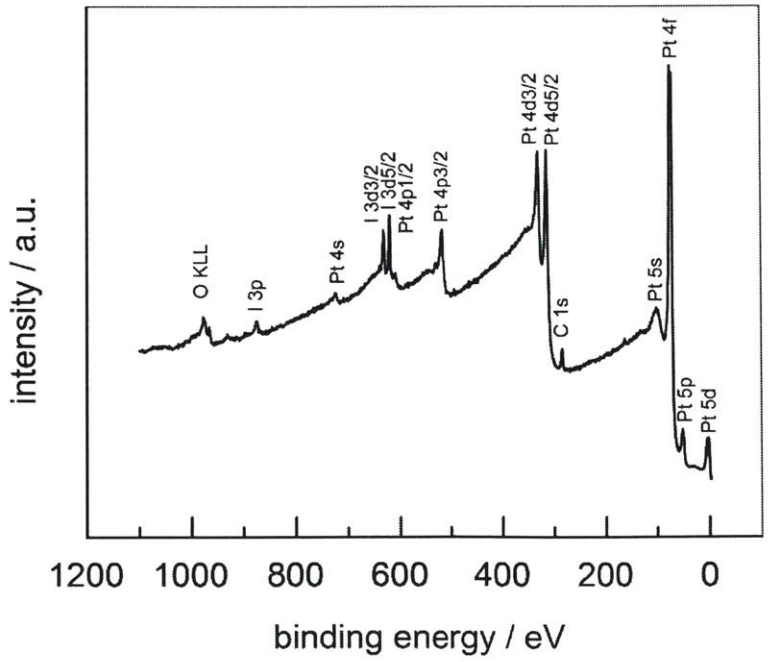
intensity / a.u.
O KLL
I 3p
Pt 4s
I 3d3/2
I 3d5/2
Pt 4p1/2
Pt 4p3/2
Pt 4d3/2
Pt 4d5/2
C 1s
Pt 5s
Pt 4f
Pt 5p
Pt 5d
1200 1000 800 600 400 200 0
binding energy / eV

Oxide-passivated Al

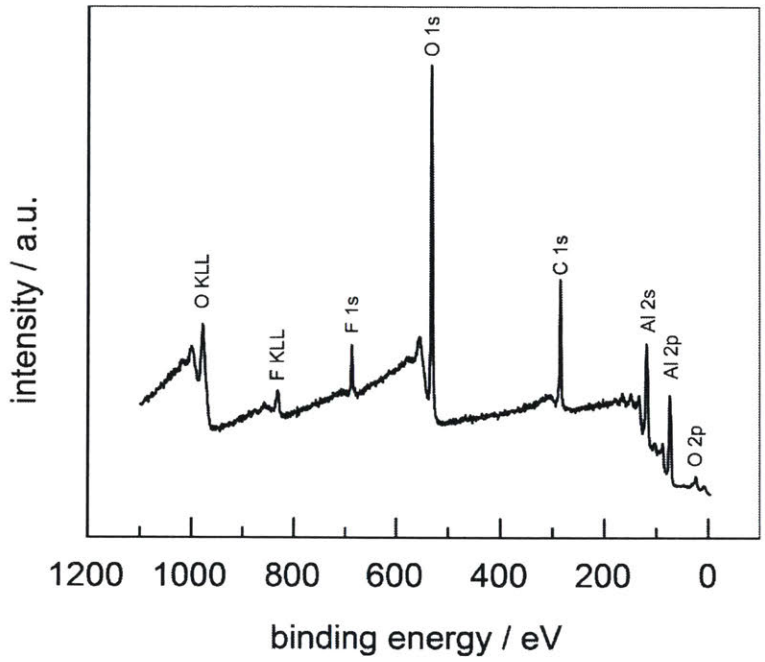

Oxide passivated Cr

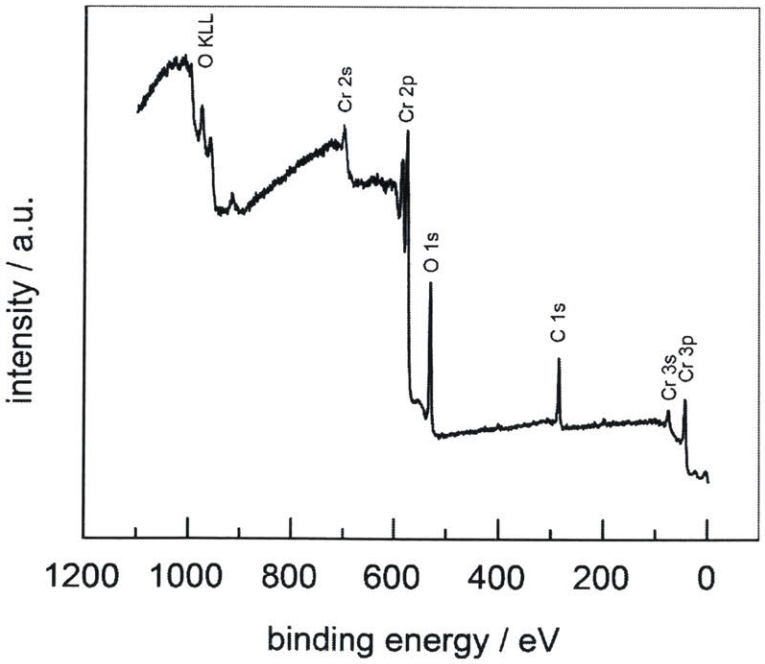

Oxide passivated Fe

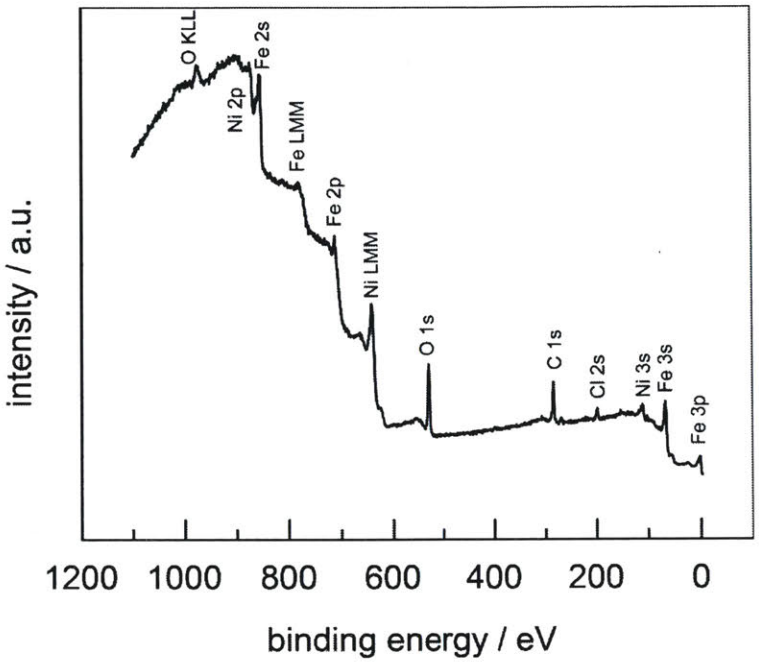

Fluorine doped tin oxide (FTO)

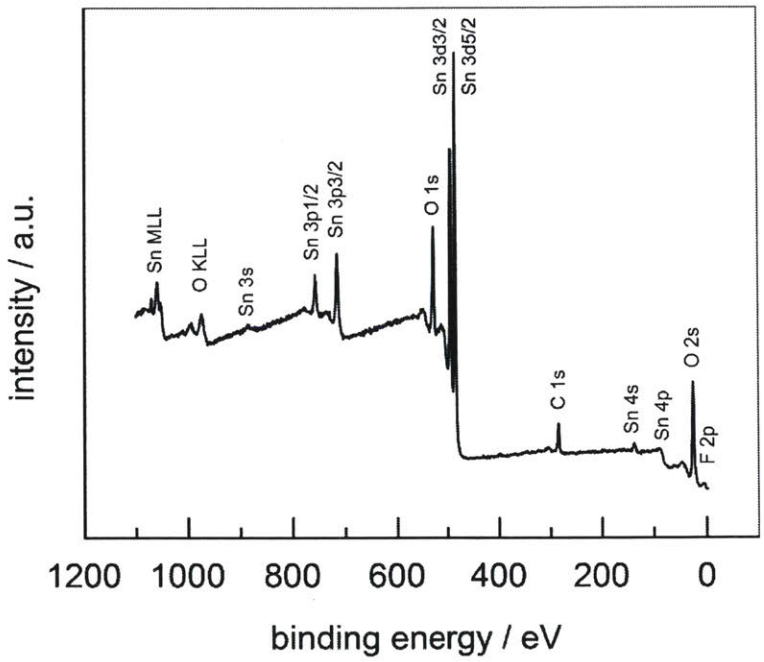

Oxide passivated Mo

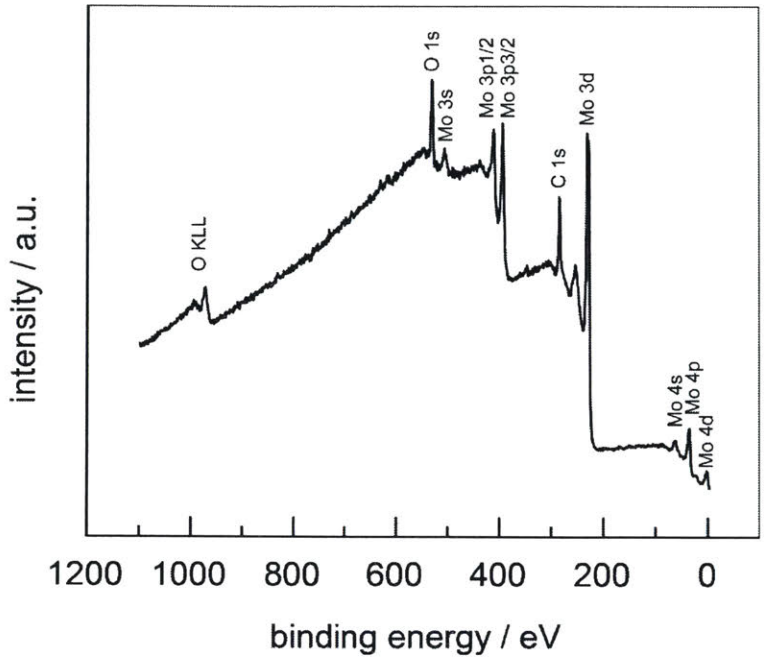

Oxide passivated Ni

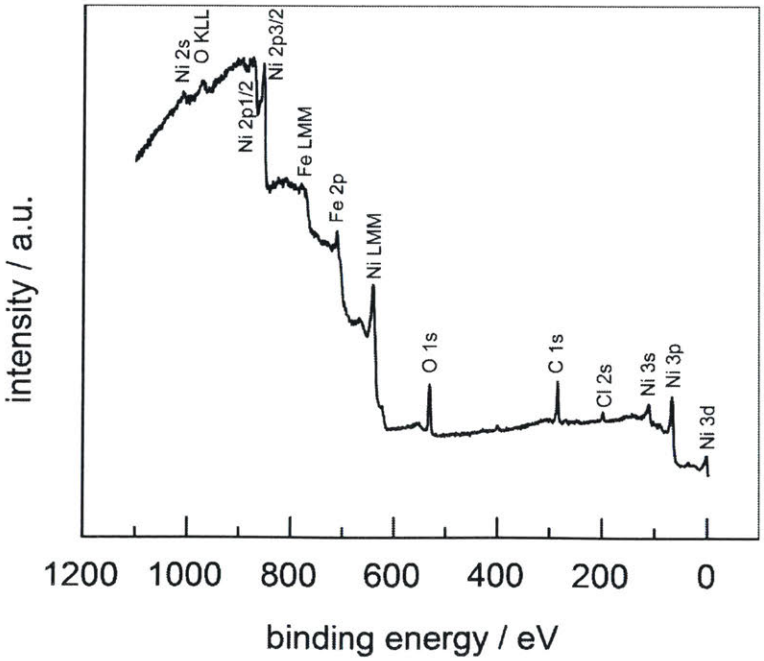

$Ni_{0.8}Fe_{0.2}$ (Permalloy)

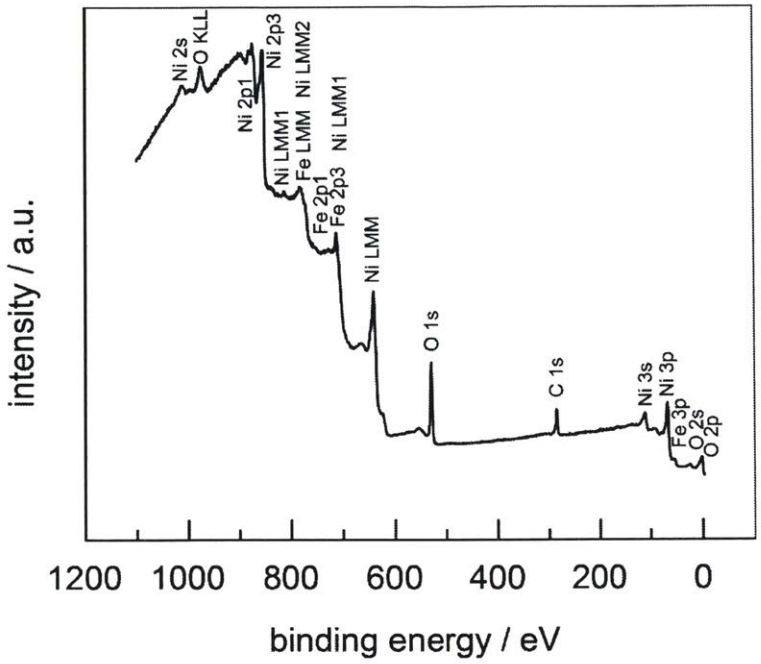

$NiFeO_x$

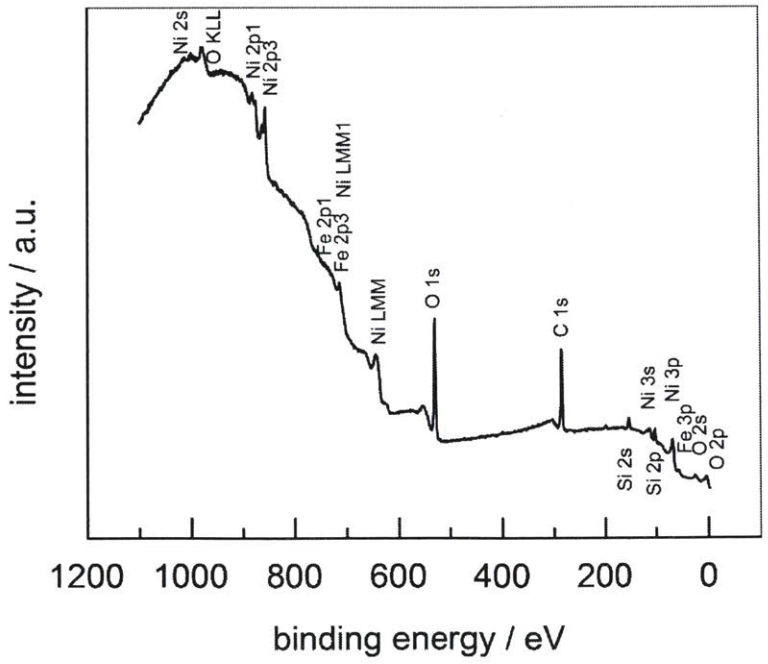

RuO_2

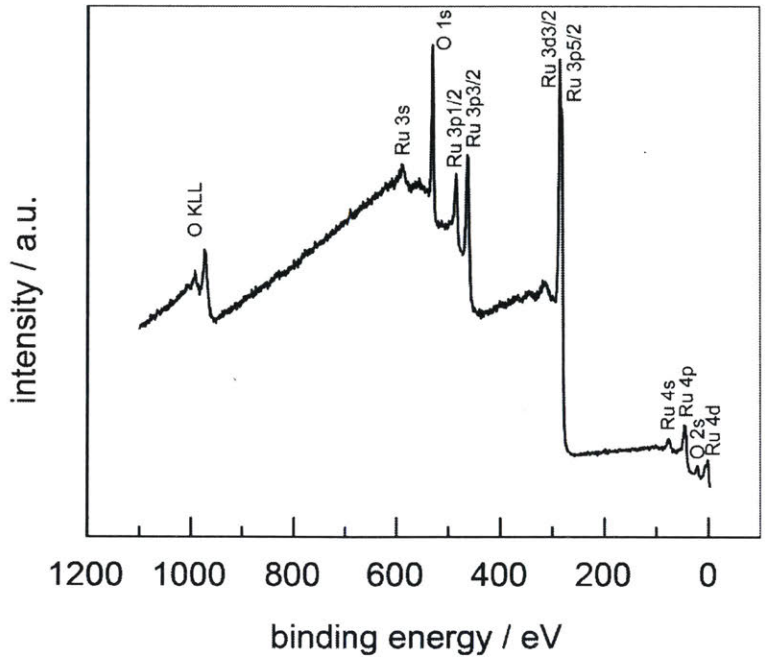

Oxide passivated Ta

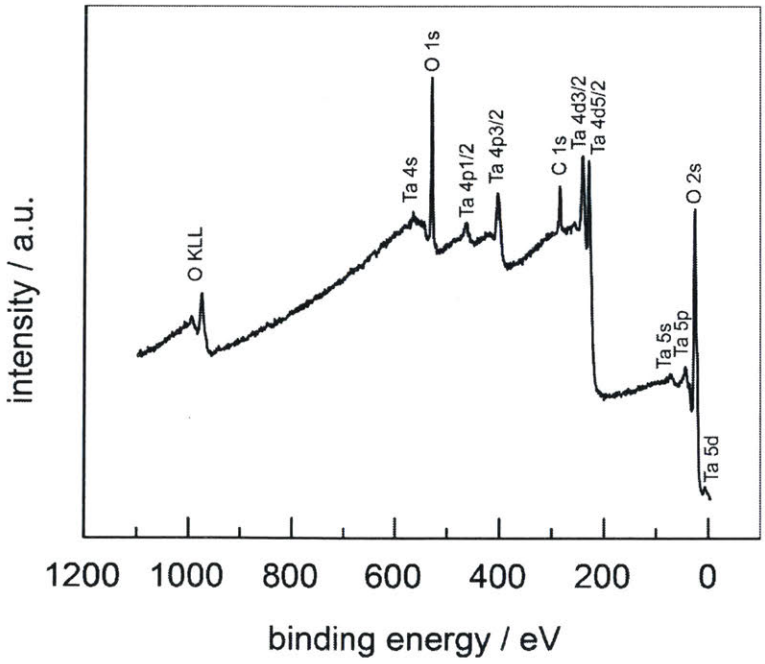

Oxide passivated Ti

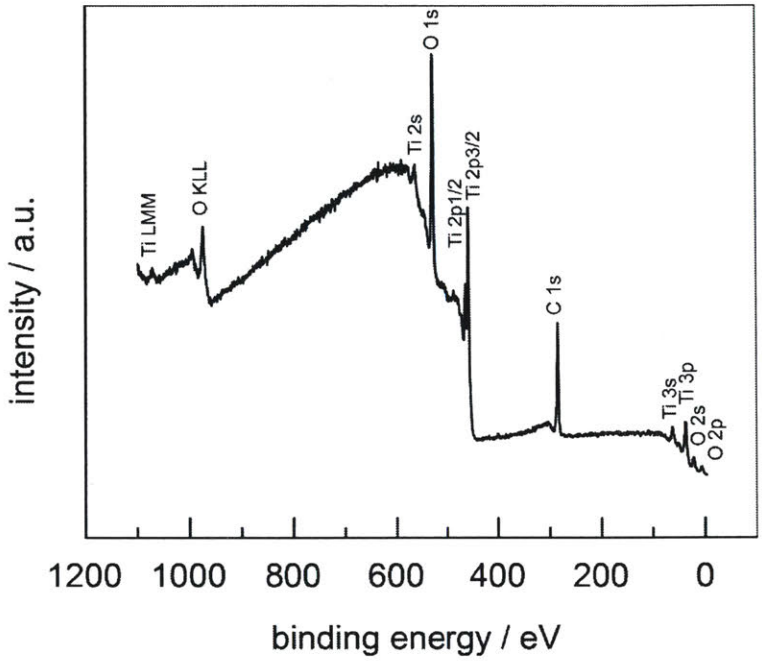

NiS_x

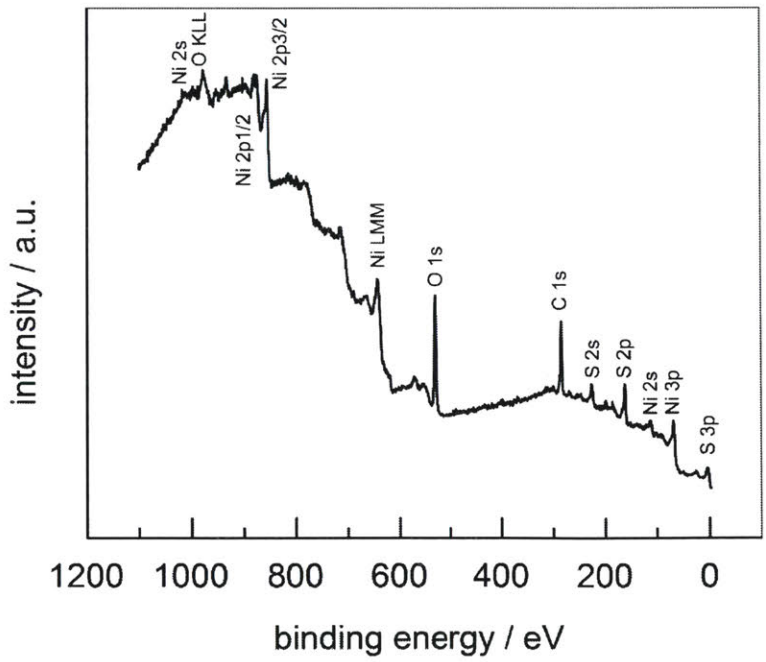

$CoSe_x$

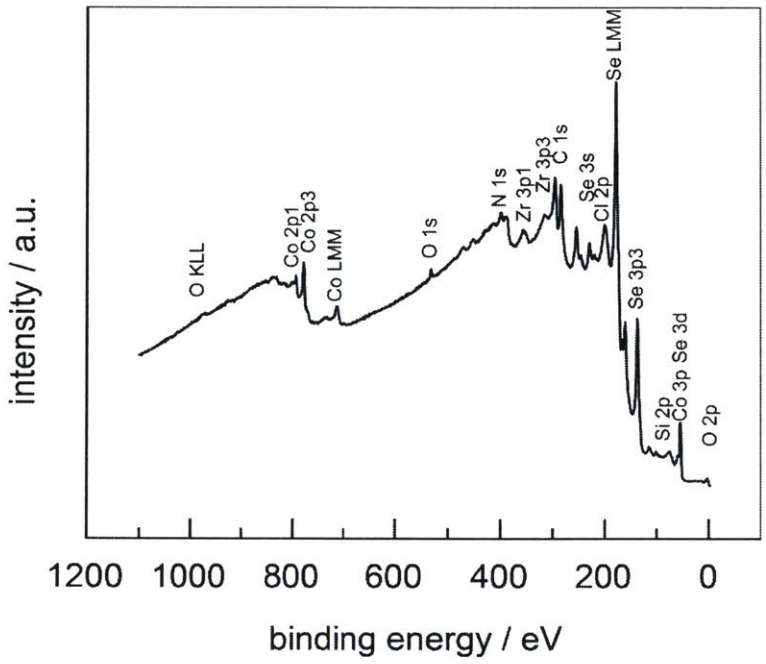
intensity / a.u.
1200
1000
800
600
400
200
0
binding energy / eV
O KLL
Co 2p1
Co 2p3
Co LMM
O 1s
N 1s
Zr 3p1
Zr 3p3
C 1s
Se 3s
Cl 2p
Se LMM
Se 3p3
Si 2p
Co 3p
Se 3d
O 2p

$NiSe_x$

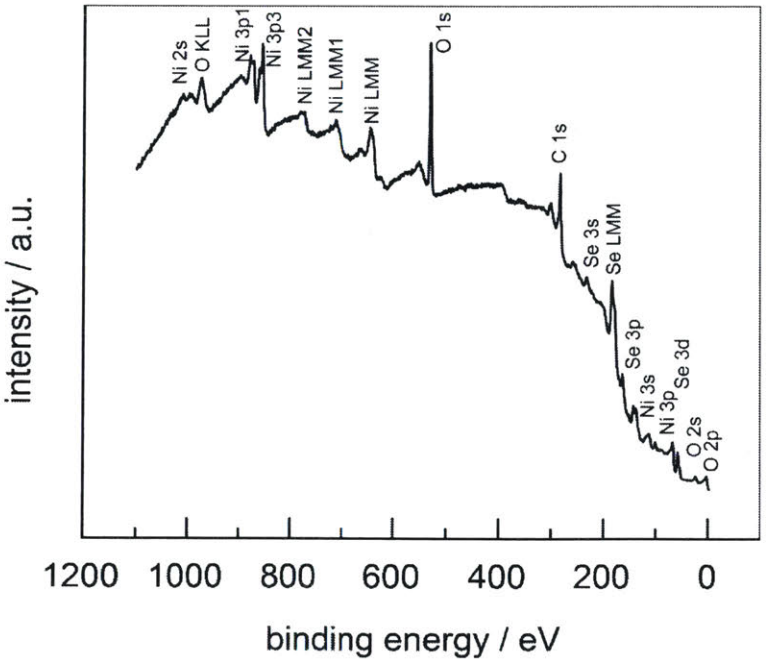
intensity / a.u.
1200
1000
800
600
400
200
0
binding energy / eV
Ni 2s
O KLL
Ni 3p1
Ni 3p3
Ni LMM2
Ni LMM1
Ni LMM
O 1s
C 1s
Se 3s
Se LMM
Se 3p
Ni 3s
Ni 3p
Se 3d
O 2s
O 2p

Graphitic C

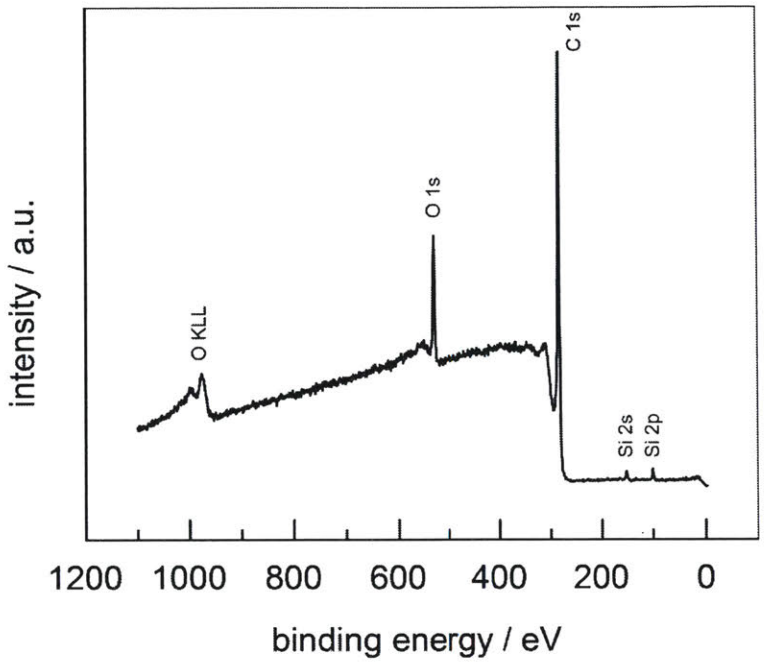
C 1s
O 1s
O KLL
Si 2s
Si 2p
intensity / a.u.
1200
1000
800
600
400
200
0
binding energy / eV

2.5 References

(1) Liu, M.; Pang, Y.; Zhang, B.; De Luna, P.; Voznyy, O.; Xu, J.; Zheng, X.; Dinh, C. T.; Fan, F.; Cao, C.; de Arquer, F. P. G.; Safaei, T. S.; Mepham, A.; Klinkova, A.; Kumacheva, E.; Filleter, T.; Sinton, D.; Kelley, S. O.; Sargent, E. H. Nature **2016**, 537 (7620), 382.

(2) McCrory, C. C. L.; Jung, S.; Ferrer, I. M.; Chatman, S. M.; Peters, J. C.; Jaramillo, T. F. J. Am. Chem. Soc. **2015**, 137 (13), 4347.

(3) Sing, K. S. W. Pure Appl. Chem. **1985**, 57 (4), 603.

(4) Herrero, E.; Buller, L. J.; Abruña, H. D. Chem. Rev. **2001**, 101 (7), 1897.

(5) Łukaszewski, M. Int. J. Electrochem. Sci. **2016**, 11 (6), 4442.

(6) Binninger, T.; Fabbri, E.; Kotz, R.; Schmidt, T. J. J. Electrochem. Soc. **2013**, 161 (3), H121.

(7) Vidu, R.; Hara, S. J. Electroanal. Chem. **1999**, 475 (2), 171.

(8) Oviedo, O. A.; Reinaudi, L.; Garcia, S.; Leiva, E. P. M. Underpotential Deposition; Monographs in Electrochemistry; Springer International Publishing: Cham, 2016.

(9) Vaskevich, a; Rosenblum, M.; Gileadi, E. J. Electroanal. Chem. **1995**, 383 (1–2), 167.

(10) Trasatti, S.; Petrii, O. A. Pure Appl. Chem. **1991**, 63 (5), 711.

(11) McCrory, C. C. L.; Jung, S.; Peters, J. C.; Jaramillo, T. F. J. Am. Chem. Soc. **2013**, 135 (45), 16977.

(12) Fang, L.; Tao, Q.; Li, M.; Liao, L.; Chen, D.; Chen, Y. Chinese J. Chem. Phys. **2010**, 23 (5), 543.

(13) Lockett, V.; Horne, M.; Sedev, R.; Rodopoulos, T.; Ralston, J. Phys. Chem. Chem. Phys. **2010**, 12 (39), 12499.

(14) Della Monica, M.; Senatore, L. J. Phys. Chem. **1970**, 74 (1), 205.

(15) Tsierkezos, N. G.; Philippopoulos, A. I. Fluid Phase Equilib. **2009**, 277 (1), 20.

(16) Gileadi, E. Physical Electrochemistry; Wiley-VCH Verlag GmbH & Co. KGaA: Weinheim, Germany, 2011.

(17) El Kadiri, F.; Faure, R.; Durand, R. J. Electroanal. Chem. **1991**, 301 (1–2), 177.

(18) Li, C. W.; Kanan, M. W. J. Am. Chem. Soc. **2012**, 134 (17), 7231.

(19) Comprehensive Treatise of Electrochemistry; Bockris, J. O., Conway, B. E., Yeager, E., Eds.; Springer US: Boston, MA, 1980.

(20) Schmickler, W.; Santos, E. Interfacial Electrochemistry; Springer Berlin Heidelberg: Berlin, Heidelberg, 2010.

(21) Trotochaud, L.; Young, S. L.; Ranney, J. K.; Boettcher, S. W. J. Am. Chem. Soc. **2014**, 136 (18), 6744.

(22) Miller, E. L. J. Electrochem. Soc. **1997**, 144 (6), 1995.

(23) Rodionova, L. S.; Filanovskii, B. K.; Petrov, M. L. Russ. J. Gen. Chem. **2001**, 71 (1), 85.

(24) Warren, J. J.; Mayer, J. M. J. Am. Chem. Soc. **2008**, 130 (24), 7546.

(25) Falkowski, J. M.; Concannon, N. M.; Yan, B.; Surendranath, Y. J. Am. Chem. Soc. **2015**, 137 (25), 7978.

(26) Banga, D.; Kim, Y.-G.; Stickney, J. J. Electrochem. Soc. **2011**, 158 (2), D99.

(27) Falkowski, J. M.; Surendranath, Y. ACS Catal. **2015**, 5 (6), 3411.

(28) Yan, B.; Krishnamurthy, D.; Hendon, C. H.; Deshpande, S.; Surendranath, Y.; Viswanathan, V. Joule **2017**, 1 (3), 600.

Chapter 3 – The role of diffusion on the selectivity of electrochemical CO_2 reduction on Au

This chapter contains text from the following article:

(1) Hall, A. S.; Yoon, Y.; Wuttig, A.; Surendranath, Y. Mesostructure-Induced Selectivity in CO 2 Reduction Catalysis. J. Am. Chem. Soc. **2015**, 137 (47), 14834.

Publication contribution notes:

The author contributed to the synthesis of Au electrodes of various morphologies, to the electrochemical testing of the catalysts, and to the design of experiments.

3.1 Introduction

As outlined in Chapter 1, the high energy cost and low selectivity of electrochemical CO_2 reduction has prevented the direct electroreduction of CO_2 from reaching economic viability.[1] One of the main challenges remains controlling the kinetically facile reduction of protons to H_2, which often outcompetes CO_2 reduction to erode reaction selectivity. Indeed, the paucity of general materials design principles for selectively inhibiting the hydrogen evolution reaction (HER) impedes the systematic development of improved CO_2 reduction catalysts.[2]

Recently, numerous nanostructured metals have been shown to catalyze CO_2 reduction with improved selectivity relative to planar polycrystalline foils. For example, Au, Cu, and Pb films prepared by electrochemical reduction of Au, Cu, and Pb oxides, respectively, display high CO_2 reduction selectivity at low overpotentials.[3–5] Likewise, dealloyed porous Ag films[6] and carbon supported Au nanoparticle[7–9] and nanowire electrodes[10] c catalyze the reduction of CO_2 to CO with high selectivity. This enhanced selectivity may arise from increases in the specific (surface area normalized) activity for CO_2 reduction and/or from a decrease in the specific activity for the H_2 evolution reaction (HER). For oxide derived Au, evidence points to both effects,[11] whereas for oxide derived Cu and Pb, specific HER activity has been shown to

diminish more dramatically than CO_2 reduction activity, giving rise to enhanced selectivity for the latter.[3,5] In general, selectivity differences have been attributed to the intrinsic selectivity of the active sites in the material. However, observations of thickness dependent product selectivity for electrodeposited porous Cu thin films[12] suggest that mass transport effects may also play a role in determining product selectivity. For example, when considering CO_2 reduction catalyzed by Au, which generates CO and H_2 predominantly, both the desired reaction (Eq 1.1) and H_2 evolution (Eq 1.2) consume protons.

This necessitates the formation of a pH gradient at the electrode surface irrespective of the product distribution.[13] However, all high surface area catalysts explored to date exhibit a high degree of disorder in pore size, length, and tortuosity, making it difficult to unambiguously deconvolute surface structure and transport effects.

Furthermore, kinetic modeling of CO_2 electroreduction and HER in aqueous bicarbonate electrolytes suggests that differentiating the availability of CO_2 and the proton donor at the electrochemical double layer during CO_2 reduction should enable enhanced CO_2 reduction selectivity. Experimental reports have shown that the reduction of CO_2 to CO on Au electrodes is gated by a single electron transfer to CO_2 to form a surface bound CO_2 anion, but not by a concerted or pre-equilibrium proton transfer.[14,15] Meanwhile, the kinetics of HER is gated by the concentration of the proton donor species, HCO_3^-, and is therefore sensitive to changes in local pH at the electrode.[14,15] Additionally, the slow hydration kinetics of CO_2 to form the proton donor species, HCO_3^-, suggests that it may be possible to maintain CO_2 reduction activity while suppressing HER.[16]

For reactions in which only a single product is possible, inhibited mass transport in a porous electrode can only serve to reduce specific activity relative to a planar surface. However, the conditions of CO_2 reduction allow for many reactions to take place simultaneously, each of

which may be gated by diffusion of different species. Thus, an appropriately designed mesostructure that takes advantage of the differential transport characteristics of each reaction should, in principle, enable enhanced selectivity. Herein, we show that this is possible by leveraging mesostructure, rather than surface structure, to modulate CO_2 reduction selectivity. We synthesized a series of ordered Au inverse opal (Au-IO) thin films of varying thickness and show that diffusional gradients formed within the porous film dramatically suppress HER specific activity relative to CO_2 reduction, leading to near quantitative selectivity for CO generation at modest overpotentials.

3.2 Results and discussion

3.2.1 Synthesis and characterization of porous Au-IO electrodes for CO_2 reduction

Gold inverse opals were synthesized by replication of ordered porous thin films.[17,18] Here, colloidal crystal templates were prepared by vertical deposition of 200 nm polystyrene spheres onto gold-coated glass slides (see section 3.4 for details).[18] Gold was then deposited into the pores by constant current electrodeposition from an aqueous electrolyte bath containing potassium tetrachloroaurate. By controlling the time duration of electrodeposition, the thicknesses of the resulting Au-IOs were systematically varied. The polystyrene spheres were then removed from the Au-IO by solvent extraction in toluene to furnish Au thin films with ordered porosity. SEM images of the resulting Au-IO replicas (Figure 3.1a) evince the formation of an ordered porous network that uniformly coats the surface. The porous network consists of 200 nm spherical voids interconnected by circular apertures of ~70 nm. Cross-sectional SEM images (Figure 3.1b) reveal that the porous network extends uniformly from the

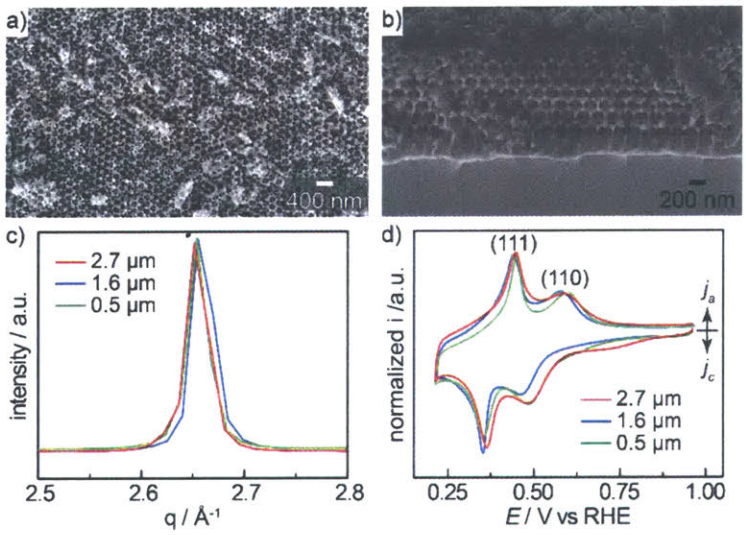

Figure 3.6. Top down (a) and cross sectional (b) SEM images of a Au-IO thin film. Grazing incidence X-ray diffraction (c) of 0.5 (green), 1.6 (blue), 2.7 (red) µm thick Au-IO samples showing the $Au_{(111)}$ Bragg diffraction peak. Cyclic voltammograms (d) of 0.5 (green), 1.6 (blue), 2.7 (red) µm thick Au-IO samples recorded in 0.1 M NaOH containing 0.01 M $Pb(OAc)_2$ (10 mV/s scan rate).

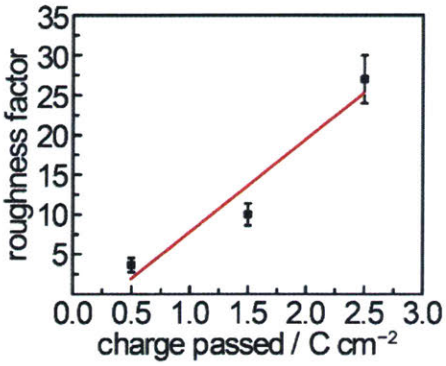

Figure 3.7. Roughness factor as a function of charge passed to deposit Au-IO films. 0.5, 1.5, and 2.5 C/cm^2 films correspond to film thicknesses of 0.5, 1.6, and 2.7 μm as determined by cross-sectional SEM. Error bars represent standard deviations of three independently synthesized Au-IO samples for each thickness. The linear fit to the data exhibits an $R^2 = 0.94$.

surface of the film to the underlying Au substrate. Consistent with this observation, electrochemical measurements of the electroactive surface area via Cu under- potential deposition[19] reveal a linear increase in the roughness factor of the electrode with increasing porous film thickness (Figure 3.2). The Au-IO samples examined here were approximately 0.5, 1.6, and 2.7 μm thick with roughness factors of 4, 10, and 27, respectively.

Au-IO films display similar grain structure and surface termination, irrespective of thickness. Grazing incidence X-ray diffraction (XRD) of the thin films (Figure 3.1c and Figure 3.) reveal similar peak widths for the Au(111) reflection, consistent with very similar grain sizes for all samples. The Scherrer equation estimates a grain size of 20 nm. To gain insight into the surface termination of Au within the pores, we examined Au-IOs by underpotential

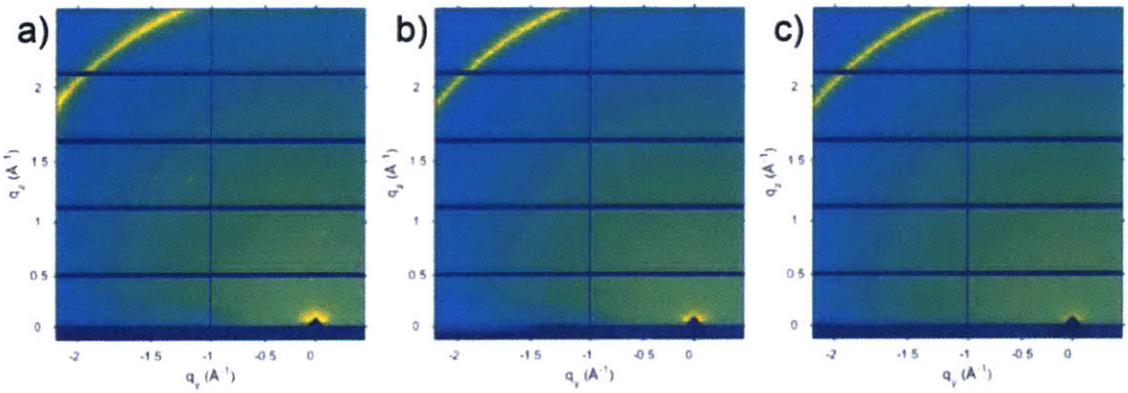

Figure 3.3. Grazing incidence XRD of 0.5 μm (a) 1.6 μm (b) and 2.7 μm (c) thick Au-IOs. Data were collected at 0.6 degrees angle of incidence.

deposition (UPD) of Pb. Unlike Cu UPD, which is diagnostic of the total electroactive surface area, Pb UPD is diagnostic of the relative population of low index facets. Irrespective of the film thickness, all Au-IO samples display two Pb deposition features at 0.35 and 0.47 V (all potentials are reported versus the reversible hydrogen electrode, RHE), and two corresponding stripping features at 0.44 and 0.50 V, respectively (Figure 3.1d). These waves correspond to Pb deposition onto and stripping from the (111) and (110) facets exposed in the Au-IO film.[20] The relative magnitude of each of these waves is similar, indicating that Au surface termination remains constant, independent of Au-IO film thickness.

3.2.2 The impact of mesostructure on CO_2 electroreduction selectivity on Au-IO electrodes

Despite displaying similar grain structure and surface termination, Au-IO catalysts exhibit thickness-dependent selectivity for CO_2 reduction catalysis. We evaluated the Au-IO samples for electrocatalytic CO_2 reduction in a two-compartment cell separated by a Selemion anion exchange membrane. Electrolysis was performed at a variety of fixed potentials in CO_2-saturated 0.1M $KHCO_3$ (pH 6.7), and the evolved gases were periodically sampled and quantified by in-line gas chromatography (see Section 3.4 for details of CO_2 reduction catalysis runs). To ensure against electrode deactivation via trace metal ion deposition, we purified all electrolytes using solid phase chelation.[21] Raw chronoamperometry traces are shown in Figure 3.. As seen in Figure 3.a, the thinnest, 0.5 μm, samples display the lowest faradaic efficiencies for CO_2 reduction at all potentials, whereas the intermediate and thickest electrodes exhibit higher efficiencies for CO_2 reduction. For example, at −0.40 V the 0.5 μm Au-IO films exhibit a faradaic efficiency (FE) for CO production of 50 %, whereas the 2.7 μm Au-IO films generate CO with 75 % FE. Interestingly, the intermediate and thickest electrodes have similar FE for CO_2 reduction. For comparison, at −0.40 V, planar polycrystalline electrodes display 50 %

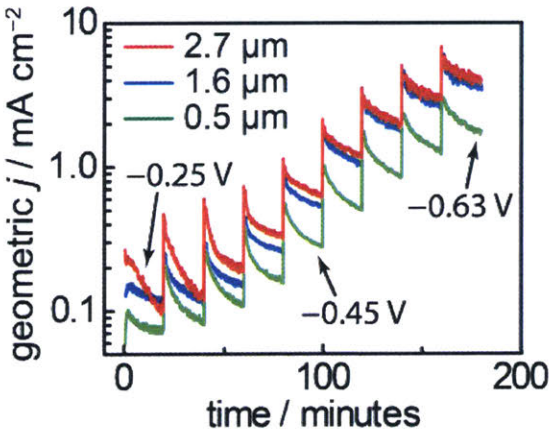

Figure 3.4. Representative stepped chronoamperometry traces of 0.5 (green), 1.6 (blue), 2.7 (red) μm thick Au-IO samples recorded in CO_2-saturated 0.1 M $KHCO_3$ electrolyte, pH 6.7, over a range of potentials spanning −0.25 to −0.63 V vs RHE. Data were normalized to the geometric area of the electrode.

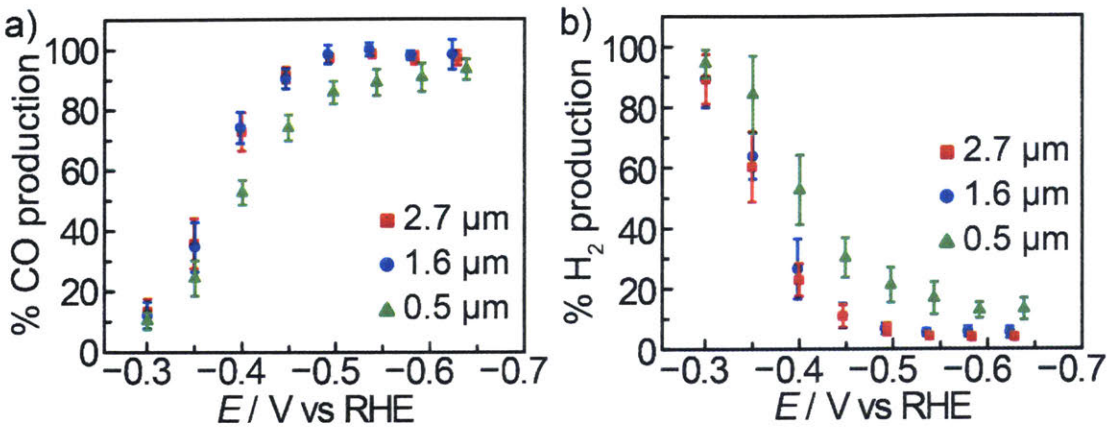

Figure 3.5. Faradaic efficiency for CO (a) and H_2 (b) evolution for 0.5 (green), 1.6 (blue), 2.7 (red) µm thick Au-IO samples evaluated in CO_2 saturated 0.1 M $KHCO_3$ electrolyte, pH 6.7. Error bars are standard deviations of three independently synthesized Au-IO samples for each thickness.

selectivity for CO production. In concert with the rise of CO FE as the porous film thickness is increased, the HER FE declines (Figure 3.b). Indeed, within experimental error, CO and H_2 account for all of the current passed in the electrolysis. Taken together, the data suggest that increased electrode porosity serves to improve electrode selectivity for CO_2 reduction relative to H_2 evolution.

To gain further insight into the origin of porosity-dependent CO_2 reduction selectivity, we compared the specific activity for CO_2 reduction and HER at various potentials (Figure 3.).

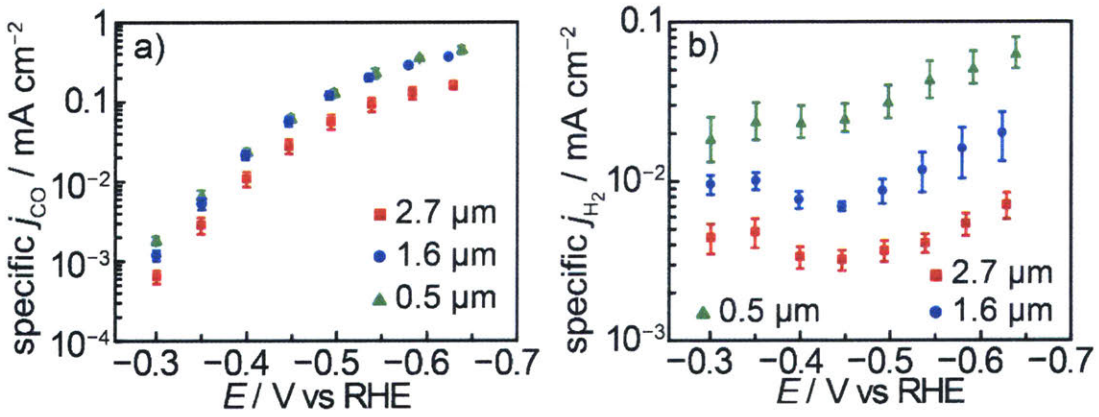

Figure 3.6. Specific activity for CO (a) and H_2 (b) evolution for 0.5 (green triangles), 1.6 (blue circles), 2.7 (red squares) µm thick Au-IO samples evaluated in CO_2 saturated 0.1 M $KHCO_3$ electrolyte, pH 6.7. Error bars represent standard deviations of three independently synthesized Au-IO samples for each thickness.

Specific activities were calculated by normalizing the observed partial current densities for CO and H_2 evolution to the electrochemically active surface area of each electrode.[19] Remarkably, despite a 3-fold increase in thickness, corresponding to a 2.5-fold increase in roughness factor, the thin and intermediate Au-IO films display identical specific activities for CO evolution over the entire potential range (Figure 3.a). The thickest Au-IO samples, in contrast, display a decrease in CO-specific activity by a factor of ~2, which we attribute to the onset of transport limitations for the thickest sample.

In comparison to the relative invariance of CO-specific activity with film thickness, H_2-specific activity is appreciably and systematically attenuated as the film thickness increases (Figure 3.b). Whereas the thinnest Au-IO films display an HER-specific activity of 22 $\mu A/cm^2$ at −0.40 V, specific activity drops to 7 and 3 $\mu A/cm^2$ for the intermediate and thick samples, respectively. Beyond −0.40 V, the thickest samples uniformly display a 10-fold decrease in HER-specific activity relative to the thinnest Au-IO films. In contrast to the polarization curves for CO production, which exhibit roughly log-linear scaling in activity between current and applied overpotential (Figure 3.a), the HER polarization curve is sigmoidal; the specific activity initially rises from −0.30 to −0.35 V, then declines or plateaus, depending on film thickness, from −0.35 to −0.45 V, before rising monotonically beyond −0.45 V (Figure 3.b). The sigmoidal behavior is observed for all thicknesses, but is most pronounced for the thickest Au-IO. The observation of declining electrocatalytic activity with increasing driving force is rare and typically indicates reaction inhibition. Notably, the decline in H_2-specific activity coincides with the generation of CO at appreciable rates. Thus, we postulate that CO adsorption and/or proton depletion caused by CO generation serves to inhibit HER catalysis.

3.2.3 The origin of CO_2 selectivity on mesostructured Au electrodes: diffusion induced pH gradients

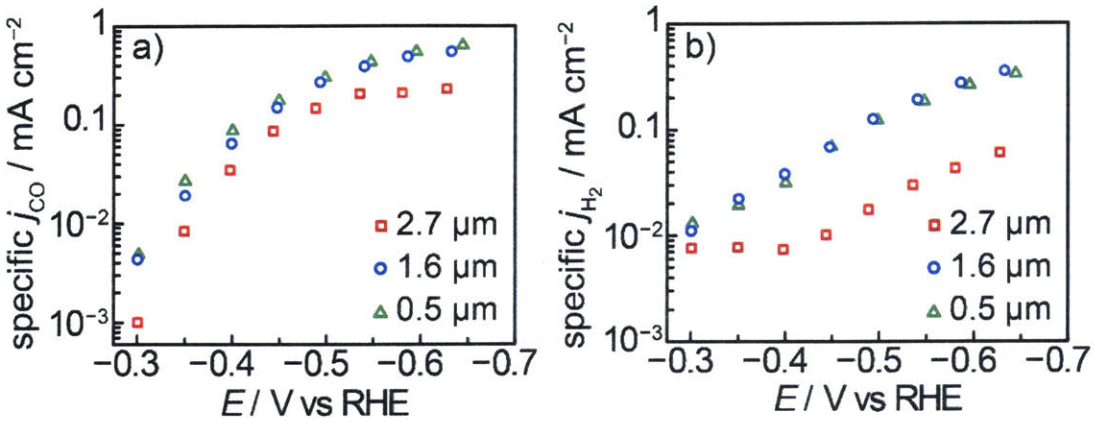

Figure 3.7. Specific activity for CO (a) and H_2 (b) evolution for 0.5 (green triangles), 1.6 (blue circles), 2.7 (red squares) μm thick Au-IO samples evaluated in CO_2 saturated 0.5 M $KHCO_3$ electrolyte, pH 7.2.

To isolate the role of local pH gradients in HER and CO_2 reduction activity, we evaluated all samples in CO_2-saturated 0.5 M $KHCO_3$, pH 7.2. The significantly higher buffer strength serves to diminish large pH gradients that are expected to form within the pores of Au-IO films. As seen in Figure 3.a, the CO-specific activities rise by a factor of between 2 and 4, depending on film thickness, but retain the general shape and trend observed in 0.1 M $KHCO_3$. In contrast, the H_2 evolution curves change dramatically. In the stronger buffering environment, the H_2 specific activity is invariant with film thickness for the thin and intermediate samples, whereas the thickest films still display suppressed H_2 evolution by ~10-fold below −0.40 V (Figure 3.b). The thickest Au-IO samples also display a plateau in H_2 specific activity at potentials ≥ −0.40 V but rise continuously at higher overpotentials. In contrast, the thinner films display monotonically rising activity over the entire potential range leading to higher HER-specific activity beyond −0.40 V relative to the lower buffer strength. Overall, the rise in HER-specific activity in 0.5 M $KHCO_3$ outpaces the modest gains in CO production, leading to lower CO_2 reduction selectivities over the entire potential range (Figure 3.). Taken together, these results suggest that HER inhibition is principally driven by increased alkalinity that develops

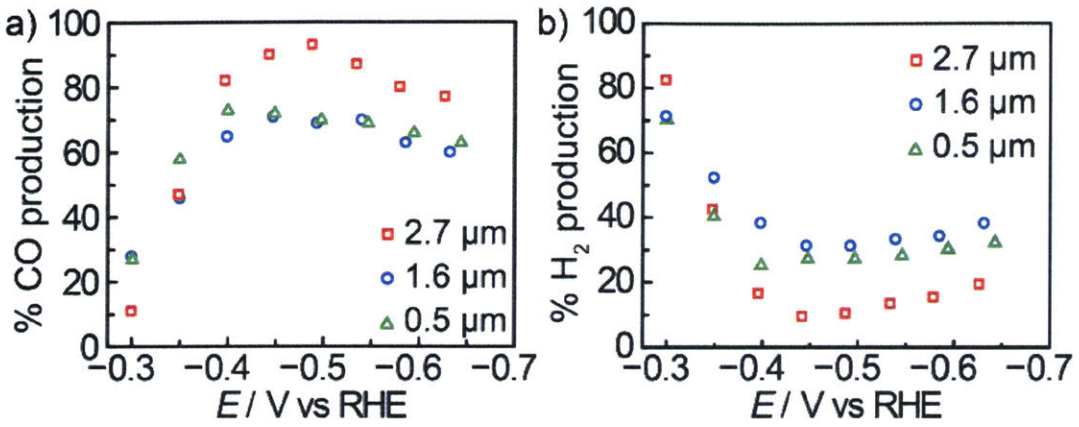

Figure 3.8. Faradaic efficiency for CO (a) and H_2 (b) evolution for 0.5 (green), 1.6 (blue), 2.7 (red) µm thick Au-IO samples evaluated in CO_2-saturated 0.5 M $KHCO_3$ electrolyte, pH 7.2.

within the porous network during catalysis. Although a comprehensive microkinetic model is still the subject of ongoing investigations, we postulate that this increased alkalinity serves to directly slow the rate of HER via local depletion of competent proton donors such as HCO_3^-. Notably, the increased alkalinity does not appear to appreciably decrease the effective CO_2 concentration in the pores, consistent with its slow hydration kinetics.[22] Additionally, computational[23] and experimental data[24,25] indicate that hydroxide adsorption promotes CO binding to Au. Thus, the increased alkalinity may also indirectly suppress HER by enhancing CO adsorption.

The differential mass transport requirements of HER and CO_2 reduction are evident even on polished polycrystalline gold electrodes. Whereas high porosity serves to amplify the influence of diffusional gradients, electrode rotation achieves the opposite effect by accelerating convective flow of reagents to the electrode surface.[26] Figure 3. shows the rotation rate dependence of HER and CO_2 reduction catalysis on a nonporous polycrystalline rotating cone electrode. The rotating cone geometry is ideally suited for the study of gas evolution reactions because it prevents bubble accumulation on the electrode surface.[27] As the rotation rate is increased from 625 to 3500 rpm, the rate of CO_2 reduction catalysis is unchanged,

whereas the rate of HER catalysis increases by ~22%. These results highlight that, irrespective of electrode morphology, CO_2 reduction catalysis is far more resistant to transport limitations than H_2 evolution.

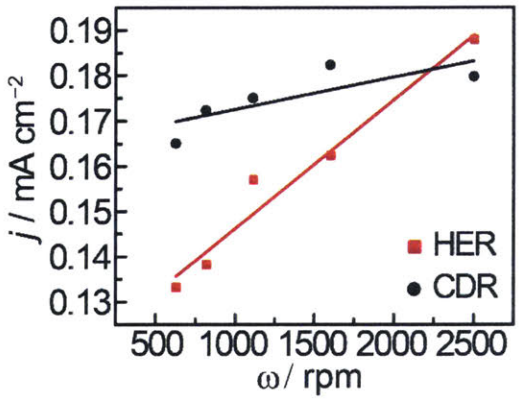

Figure 3.9. HER (red squares) and CDR (black circles) catalytic current vs rotation rate of a gold rotating cone electrode in CO_2 saturated 0.1 M $NaHCO_3$ at -0.55 V vs RHE. Lines are included as guides to the eye.

3.3 Concluding remarks

In summary, we have shown that electrode mesostructuring is a powerful tool for tuning the selectivity of CO_2 reduction catalysis. Diffusional limitations imposed by a porous electrode serve to inhibit hydrogen evolution while preserving high rates of CO_2 reduction to CO. These results highlight that changes in the observed selectivity for CO_2 reduction cannot, a priori, be exclusively attributed to changes in the intrinsic selectivity of surface active sites. Indeed, a complex interplay between surface structure, electrode mesostructure, and the electrolyte composition serve to define the experimental selectivity. The ordered porous environments provided by metal inverse opals make them an ideal platform for deconvoluting these effects, enabling accurate simulations of surface concentration profiles and systematic studies of reaction mechanism. Furthermore, the data agree with kinetic models put forth on the reduction of CO_2 to CO and HER on Au surfaces. Specifically, the data support the model that the rate limiting step for CO_2 reduction is a single electron transfer step that is decoupled from proton transfer, while HER remains proton coupled in its rate limiting step.

3.4 Experimental methods

Materials. Potassium bicarbonate (≥ 99.95 % trace metals basis, Lot # MKBT3696V, Sigma Aldrich), potassium tetrachloroaurate(III) hydrate (99.99 % Premion®, Alfa Aesar), perchloric acid (99.999 %, Sigma Aldrich), IGEPAL® CO-520 (average Mn 441, Sigma Aldrich), copper (II) sulfate pentahydrate (99.999 % PURATREM, Strem Chemicals), lead (II) acetate trihydrate (99.999 %, Strem Chemicals), sodium 3-mercapto-1-propanesulfonate (technical grade, Sigma Aldrich), sodium hydroxide (99.99 %, Sigma Aldrich), gold-coated glass slides (EMF corporation, 5 nm Ti adhesion layer, 100 nm of Au overlayer), hydrogen peroxide 30 wt % (ACS Reagent Grade, Sigma Aldrich), sulfuric acid (ACS Reagent Grade, EMD Millipore), 200 nm sulfate-modified polystyrene spheres, 8 % w/v (Product # S37491, Interfacial Dynamics Corporation) were used without modification or purification unless otherwise noted. CO_2-saturated 0.1 M $KHCO_3$, pH 6.7, and CO_2-saturated 0.5 M $KHCO_3$, pH 7.2, were prepared by sparging 0.1 M and 0.5 M $KHCO_3$, respectively, with CO_2 (Research Grade, Airgas) for 20 minutes. All electrolyte solutions were prepared with reagent grade water (Millipore Type 1, 18 MΩ-cm resistivity) and purified of trace metal ion impurities by stirring the as prepared electrolyte in regenerated Chelex resin, ~50 g Chelex for 1 L of 0.1 M electrolyte, for at least 24 hours prior to use in electrolysis runs. Chelex® 100 Resin (Bio-Rad, Catalog # 210011676) was regenerated according to the manufacturer's protocol,[28] with slight modifications. Specifically, Chelex was regenerated by stirring the as-received material for 12 hours in 1 M HCl (ACS Reagent Grade, EMD Chemicals) followed by rinsing with 5 L of reagent grade water. Subsequently, Chelex was placed in 1 M KOH (99.99 %, semiconductor grade, Sigma-Aldrich) for 24 hours at 60 °C with constant stirring. Chelex was then rinsed with 8 L of reagent grade water until the pH of the filtrate was below 10.8.

Synthesis of Gold Inverse Opals. Gold inverse opals were prepared by

electrodeposition of gold into the voids of a polystyrene colloidal crystal host template. Gold-coated glass slides were cleaned by immersion in freshly-prepared piranha solution (prepared by slowly adding one part hydrogen peroxide to two parts sulfuric acid; **caution: piranha solutions are potentially explosive if the peroxide fraction rises above 50 %**) without additional heating for one hour. After rinsing with copious amounts of water, the cleaned gold-coated glass slides were immersed in a 10 mM aqueous solution of sodium 3-Mercapto-1-propanesulfonate overnight, followed by rinsing with copious amounts of reagent grade water. The slides were then dried in a nitrogen stream and immersed vertically or at a 45° angle into an aqueous solution containing 0.008 wt % sulfate-modified polystyrene spheres and 0.003 wt % IGEPAL CO-520 surfactant. The solvent was allowed to evaporate completely by heating in a temperature-controlled oven at 55 °C until dry, yielding a white film (the quality of the crystal was judged by the observation of green diffraction which can be seen at some angles) coating the gold-coated glass slide. The colloidal crystal films were sintered at 95 °C for 2 hours to provide pore connectivity in the inverse opal replicas. The colloidal crystal films were then immersed in ethanol and 0.1 M perchloric acid in sequence for 10 seconds duration in each solution prior to transfer to the gold electroplating bath consisting of 0.1 M $HClO_4$ and 50 mM $KAuCl_4$. The aforementioned immersion sequence is necessary to prevent delamination of the polystyrene colloidal crystal from the gold substrate. Gold was electroplated galvanostatically at a constant current of 0.5 mA/cm^2 until 0.5 C/cm^2, 1.5 C/cm^2, or 2.5 C/cm^2 of charge had passed, leading to Au-IO films of approximately 0.5, 1.6, and 2.7 μm thicknesses. The polystyrene spheres were subsequently dissolved by soaking the thin films in toluene overnight. The samples were then washed with copious amounts of ethanol and water. Finally, the Au-IOs were soaked in piranha solution for 10 minutes to remove any residual organic species from the Au surface.

Scanning Electron Microscopy (SEM). Following electrodeposition, Au-IOs films

were rinsed with copious amounts of Milli-Q water and allowed to dry in air. The glass slides were then cleaved and imaged in profile and top down using a Zeiss Merlin field emission-SEM with an acceleration voltage of 5 keV to produce the image shown in Figure 3.1a and Figure 3.1b.

Grazing incidence X-ray diffraction (GIXD) data. GIXD patterns were obtained using beam line 8-ID-E at the Advanced Photon Source at Argonne National Laboratory. A beam energy of 7.35 keV and an incidence angle of 0.6° was used to obtain the reported patterns shown in Figure 3.1c and Figure 3..

Copper Underpotential Deposition. Electroactive surface areas of the Au-IO films were determined by copper underpotential deposition. Experiments were conducted using a Gamry Reference 600 potentiostat, a Hg/Hg_2SO_4 (CH Instruments) reference electrode, and a high surface area Pt-mesh counter electrode (Alfa Aesar, 99.997 %). Hg/Hg_2SO_4 reference electrodes were stored in saturated K_2SO_4 and periodically checked relative to pristine reference electrodes to ensure against potential drift. All experiments were performed at ambient temperature, (21 ± 1 °C). The Au-IO films were cycled from 0.1 V to −0.4 V vs Hg/Hg_2SO_4 at a scan rate of 50 mV/s in N_2-saturated 0.05 M H_2SO_4 containing 0.1 M $CuSO_4$. The broad anodic wave at ~ −0.1 V vs Hg/Hg_2SO_4 was integrated and divided by 92.4 C/cm^2 to obtain the electroactive surface area.[4] This protocol was used to collect the data shown in Figure 3.2, and the surface area values for each electrode were used to normalize the measured partial current densities for CO and H_2 evolution.

Lead Underpotential Deposition. Surface terminations of Au-IO films were analyzed by lead underpotential deposition. Experiments were conducted in a similar manner to above, except with use of Ag/AgCl (Pine) reference electrode. The Au-IO films were cycled from 0.1 V to −0.8 V vs Ag/AgCl at a scan rate of 10 mV/s in N_2-saturated 0.1 M NaOH electrolyte

containing 10 mM $Pb(CH_3CO_2)_2$ to collect data shown in Figure 3.1d.

Electrocatalytic CO_2 Reduction. Experiments were conducted using a Biologic VSP 16 channel potentiostat, a leakless Ag/AgCl reference electrode (EDAQ), and a high surface area Pt mesh counter electrode (Alfa Aesar, 99.997 %). Ag/AgCl reference electrodes were stored in distilled water between measurements and were periodically checked relative to pristine reference electrodes to ensure against potential drift. All experiments were performed at ambient temperature (21 ± 1 °C). Electrode potentials were converted to the reversible hydrogen electrode (RHE) scale using E(RHE) = E(Ag/AgCl) + 0.197 V + 0.059(pH) and corrected for the uncompensated Ohmic loss (iRu) in situ via the current interrupt method. Ru values were measured using the Ru test function in the Biologic software. Prior to each experiment, the uncompensated cell resistance was measured and typically ranged from 6 to 30 Ω. In situ iRu compensation levels were set to 80% of the measured Ru values and the residual 20% was accounted for mathematically during data workup. All electrolyte solutions were used as both the catholyte and the anolyte, and working electrode chamber was stirred at a constant rate of 500 rpm during all experiments. In all cases, experiments were conducted in an airtight H-cell with 25 mL catholyte and 20 mL anolyte separated by an anion exchange membrane (AGC Selemion membrane). All H-cells were cleaned by immersion in piranha without additional heating for one hour and subsequently rinsed with Milli-Q water prior to each experiment. During all experiments, the catholyte was sparged continuously with research grade CO_2 at 10 sccm, whereas the anolyte was sparged continuously with N_2. Prior to the start of each experiment, the catholyte was sparged with CO_2 at 10 sccm for 20 min to equilibrate the solution. During electrolysis, evolved gases were quantified using in-line gas chromatography as described below. All current density values are reported relative to the electrochemically active surface area of the working electrode as measured by copper under potential deposition following the electrolysis run, described below.

Product Distribution Analysis. Electrolysis product distributions were measured using an in-line gas chromatograph (SRI Instruments, Multi-Gas Analyzer #3) equipped with a thermal conductivity detector, methanizer, and flame ionization detector in series following Molsieve 13x and Hayesep D columns. Electrodes were polarized at various potentials sufficient for CO_2 reduction catalysis while CO_2 was continuously sparged at a flow rate of 10 sccm. GC traces were collected every 20 min. A 15 sec anodic pulse was applied at 0.6 V vs Ag/AgCl (1.2 V vs RHE) prior to each potential step to clean the surface of absorbed species accumulated in the pores during prior electrolyses. The pulse potential lies below the Au oxide formation potential under these conditions and does not induce significant changes in surface structure or porosity, as verified by Pb-UPD and Cu-UPD prior to and post electrolysis, respectively. The partial current density (j) for each evolved gaseous product were calculated using the following relationship: j = [p]*flow rate*nFP/RT*1/A, where [p] is the ppm value of the product measured via GC using an independent calibration standard gas mixture, A is the electroactive surface area of the electrode as determined by Cu UPD (described above), n is the number of electrons transferred per equivalent of p, P is the pressure in the electrochemical cell headspace (1.1 atm), T is the temperature, and F is Faraday's constant. The partial current density for a given product was divided by the total current density, averaged over a 30 s span immediately prior to each GC run, to determine its partial faradaic efficiency (Figure 3.). The data shown in Figure 3. and Figure 3. are the average and standard deviation of three independent measurements using three independently prepared electrodes of a given thickness.

Rotating Cone Electrode Measurements. A gold rotating cone (r = 0.25 cm, 45° cone angle, custom milled, PINE Research Instrumentation) was employed as the working electrode. Electrode rotation was controlled using a Metrohm Autolab B.V. rotator that formed an air tight seal (using copious amounts of Parafilm) with the working compartment of the H-cell. The electrodes were polished sequentially using 1 μm and 0.3 μm alumina and sonicated using a

bath sonicator for 5 min prior to each experiment. Rotation rate dependent product distributions were measured by conducting controlled potential electrolyses at −0.5 V in Chelex-treated CO_2-saturated 0.1 M $NaHCO_3$. Prior to each chronoamperometry run, the electrode was cycled in 0.1 M H_2SO_4 from 0.2 to 1.5 V vs Ag/AgCl at 50 mV/s five times without pause, subsequently rinsed with Milli-Q, then transferred into an H-Cell using a protective water droplet. For a given rotation rate, a GC trace was taken after steady state was reached and the generated gases were equilibrated in the headspace (after 19 min). The rotation rate was varied in the following order, 2063, 976, 3460, 730, 1371 rpm to ensure against systematic errors due to electrode history. The rotation sequence was performed twice, and the reported data in Figure 3. is the average of the two sequences. Partial current densities for CO and H_2 production were determined by in-line gas chromatography as described above.

3.5 References

(1) Jones, J.-P.; Prakash, G. K. S.; Olah, G. A. Isr. J. Chem. **2014**, 54 (10), 1451.

(2) Hori, Y. In Modern Aspects of Electrochemistry; Springer New York: New York, NY; pp 89–189.

(3) Li, C. W.; Kanan, M. W. J. Am. Chem. Soc. **2012**, 134 (17), 7231.

(4) Chen, Y.; Li, C. W.; Kanan, M. W. J. Am. Chem. Soc. **2012**, 134 (49), 19969.

(5) Lee, C. H.; Kanan, M. W. ACS Catal. **2015**, 5 (1), 465.

(6) Lu, Q.; Rosen, J.; Zhou, Y.; Hutchings, G. S.; Kimmel, Y. C.; Chen, J. G.; Jiao, F. Nat. Commun. **2014**, 5.

(7) Reske, R.; Mistry, H.; Behafarid, F.; Roldan Cuenya, B.; Strasser, P. J. Am. Chem. Soc. **2014**, 136 (19), 6978.

(8) Zhu, W.; Michalsky, R.; Metin, Ö.; Lv, H.; Guo, S.; Wright, C. J.; Sun, X.; Peterson, A. A.; Sun, S. J. Am. Chem. Soc. **2013**, 135 (45), 16833.

(9) Kim, D.; Resasco, J.; Yu, Y.; Asiri, A. M.; Yang, P. Nat. Commun. **2014**, 5, 4948.

(10) Zhu, W.; Zhang, Y.-J.; Zhang, H.; Lv, H.; Li, Q.; Michalsky, R.; Peterson, A. A.; Sun, S. J. Am. Chem. Soc. **2014**, 136 (46), 16132.

(11) Feng, X.; Jiang, K.; Fan, S.; Kanan, M. W. J. Am. Chem. Soc. **2015**, 137 (14), 4606.

(12) Sen, S.; Liu, D.; Palmore, G. T. R. ACS Catal. **2014**, 4 (9), 3091.

(13) Gupta, N.; Gattrell, M.; MacDougall, B. J. Appl. Electrochem. **2006**, 36 (2), 161.

(14) Wuttig, A.; Yoon, Y.; Ryu, J.; Surendranath, Y. J. Am. Chem. Soc. **2017**, 139 (47), 17109.

(15) Wuttig, A.; Yaguchi, M.; Motobayashi, K.; Osawa, M.; Surendranath, Y. Proc. Natl. Acad. Sci. **2016**, 113 (32), E4585.

(16) Pocker, Y.; Bjorkquist, D. W. J. Am. Chem. Soc. **1977**, 99 (20), 6537.

(17) Li, C.; Dag, Ö.; Dao, T. D.; Nagao, T.; Sakamoto, Y.; Kimura, T.; Terasaki, O.; Yamauchi, Y. Nat. Commun. **2015**, 6 (1), 6608.

(18) Shimmin, R. G.; DiMauro, A. J.; Braun, P. V. Langmuir **2006**, 22 (15), 6507.

(19) Rouya, E.; Cattarin, S.; Reed, M. L.; Kelly, R. G.; Zangari, G. J. Electrochem. Soc. **2012**, 159 (4), K97.

(20) Hamelin, A.; Lipkowski, J. J. Electroanal. Chem. Interfacial Electrochem. **1984**, 171 (1–2), 317.

(21) Wuttig, A.; Surendranath, Y. ACS Catal. **2015**, 5 (7), 4479.

(22) Pocker, Y.; Bjorkquist, D. W. J. Am. Chem. Soc. **1977**, 99 (20), 6537.

(23) Rodríguez, P.; Koverga, A. A.; Koper, M. T. M. Angew. Chemie Int. Ed. **2010**, 49 (7), 1241.

(24) Rodriguez, P.; Feliu, J. M.; Koper, M. T. M. Electrochem. commun. **2009**, 11 (6), 1105.

(25) Rodriguez, P.; Kwon, Y.; Koper, M. T. M. Nat. Chem. **2012**, 4 (3), 177.

(26) Bard, A. J.; Faulkner, L. R. Electrochemical Methods: Fundamentals and Applications, 2nd Edition; John Wiley & Sons, 2000.

(27) Kirowa-Eisner, E. J. Electrochem. Soc. **1976**, 123 (1), 22.

(28) Chelex® 100 Chelex 20 Chelating Ion Exch. Resin Instr. Man. 2014 http://www.bio-rad.com/ (accessed Jun 15, 2016).

Chapter 4 - The role of diffusion on the selectivity of electrochemical CO_2 reduction on Ag

This chapter contains text from the following article:

(1) Yoon, Y.; Hall, A. S.; Surendranath, Y. Tuning of Silver Catalyst Mesostructure Promotes Selective Carbon Dioxide Conversion into Fuels. Angew. Chemie Int. Ed. **2016**, 55 (49), 15282.

4.1 Introduction

In the previous chapter, the role of catalyst mesostructured-induced diffusion to suppress H_2 evolution while maintaining CO_2 reduction activity was demonstrated on Au catalysts. In this chapter, we show that mesostructure induced CO_2 reduction activity on Ag surfaces reveals more complex chemical dynamics at play, leading to the dramatic tunability of CO_2 reduction selectivity and activity on Ag surfaces.

For a simple electrochemical reaction involving a single diffusion species that converts to a single product, transport limitations at an electrode surface can only serve to decrease intrinsic catalytic performance. However, for aqueous CO_2-to-fuels catalysis in which multiple reaction partners are involved in multiple concurrent reaction paths, transport limitations can actually lead to several possible outcomes in terms of overall electrode performance. If the undesired pathway is more sensitive to transport limitations than the desired reaction, electrode selectivity will improve, but the specific activity for the desired reaction will remain unchanged. We have demonstrated this phenomenon for Au-catalyzed CO_2 reduction in the previous chapter,[1] for which mesostructuring induces transport limitations that suppress the rate of H_2 evolution but leave the rate of CO production largely unchanged.[1] Likewise, enhanced selectivity on mesostructured oxide-derived Ag surfaces has been attributed, in part, to transport-limitation-induced H_2 suppression.[2] A tantalizing alternative possibility, which is

entirely unprecedented, is one in which transport limitations serve to promote and enhance the rate of the desired reaction while simultaneously suppressing the undesired reaction. In this limit, the electrode's specific activity, selectivity, and geometric activity would all be enhanced concomitantly. Herein, we synthesize ordered mesostructured Ag-IO electrodes and demonstrate that increasing the thickness of the mesostructure, without changing the surface structure, effects simultaneous promotion of CO generation and suppression of HER, allowing for dramatic tuning of CO_2-to-fuels selectivity from <5 % to >80 %.

4.2 Results and discussion

4.2.1 Synthesis and characterization of porous Ag-IO electrodes for CO_2 reduction

Ordered mesostructured Ag inverse opals (Ag-IO) exhibiting uniform surface structure, porosity, and tortuosity were prepared by the replication of colloidal polystyrene thin films on Au coated glass slides. The details of the 200 nm polystyrene sphere deposition, sintering, and silver electrodeposition can be found in Section 4.4.[3,4] Ag was electrochemically deposited into the necked polystyrene opal using a commercial alkaline Ag plating solution containing Ag succinimide. By controlling the amount of Ag deposited, the thicknesses of the Ag-IO films were systematically altered. Following deposition, the polystyrene spheres were selectively removed by dissolution and extraction into toluene, leaving the bare Ag-IO with ordered porosity. Scanning electron microscope (SEM) images reveal the formation of smooth, ordered,

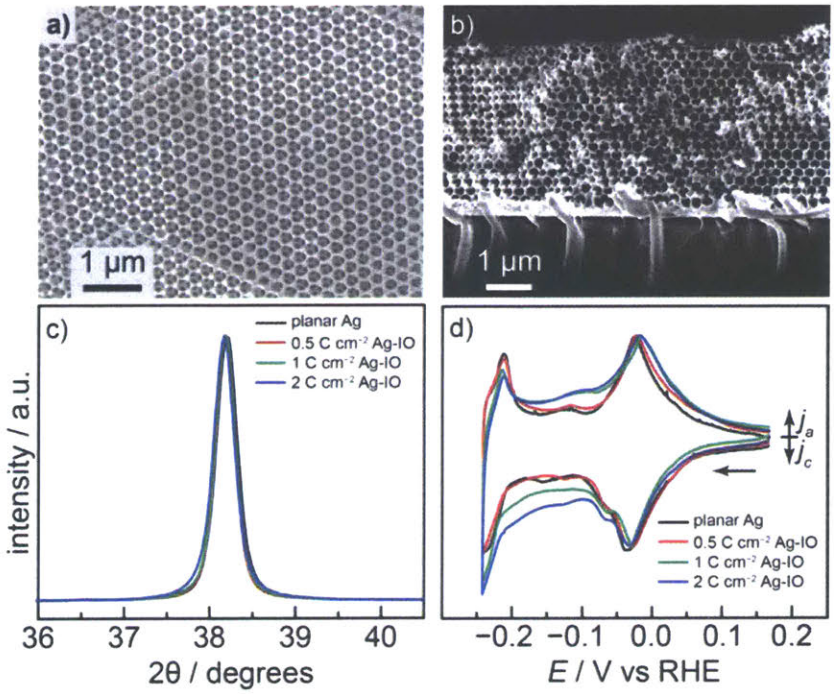

Figure 4.1. Top down (a) and cross-sectional (b) SEM micrographs of a Ag-IO film prepared by passing 1 C/cm^2 Ag deposition charge. Normalized X-ray diffraction peak for the Ag(111) reflection (c) and cyclic voltammograms (d) of thallium UPD and stripping, normalized to the −0.03 V peak, for Ag-IO samples prepared by passing 0.5 (red), 1 (green), and 2 (blue) C/cm^2 Ag deposition charge and nominally planar Ag films (black).

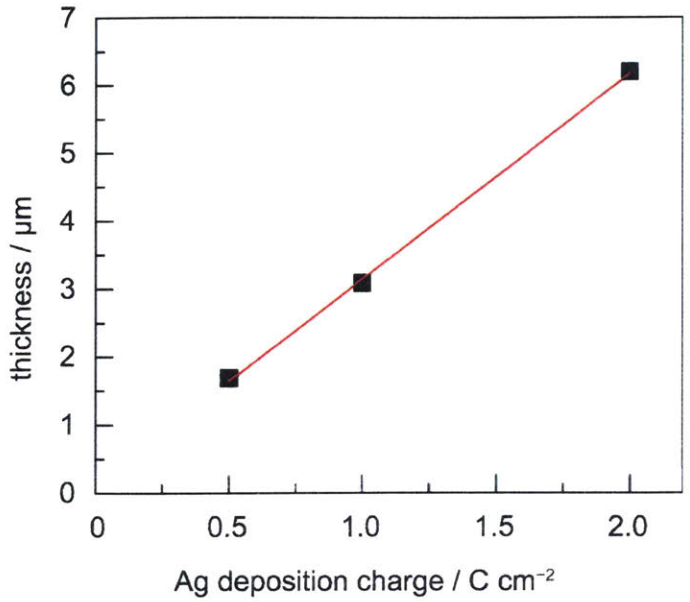

Figure 4.2. Ag-IO film thickness, determined by cross sectional SEM, as a function of electrodeposition charge.

porous Ag-IO networks with ~200 nm voids interconnected by ~50 nm channels (Figure 4.a, b). The pores generally display a hexagonal closed packed arrangement, reflecting the FCC lattice of the polystyrene host template. The porosity remains uniform over the entire thickness of the film reflecting the fidelity of this synthetic method. By varying the Ag deposition charge passed from 0.5 to 2 C/cm^2 we are able to tune the thickness of the porous film from ~1.7 to ~6.2 µm (Figure 4.). We determined the electrochemically active surface area (ECSA) of each electrode by dividing its aqueous double layer capacitance (DLC) by the 25 µF/cm^2 value for a planar Ag surface.[5] The aqueous capacitance current vs scan rate plots are linear, indicating negligible ion transport resistances within the Ag-IO film (Figure 4.). These ECSA values were normalized to the geometric area of each electrode to determine its roughness factor (RF). By varying the Ag deposition charge, we are able to tune the RF from ~43 to ~110, corresponding to a ~4.5 µm span of Ag-IO thickness (Figure 4.) Together these observations establish that electrodeposition into self-assembled opal templates generates tunable porous electrodes.

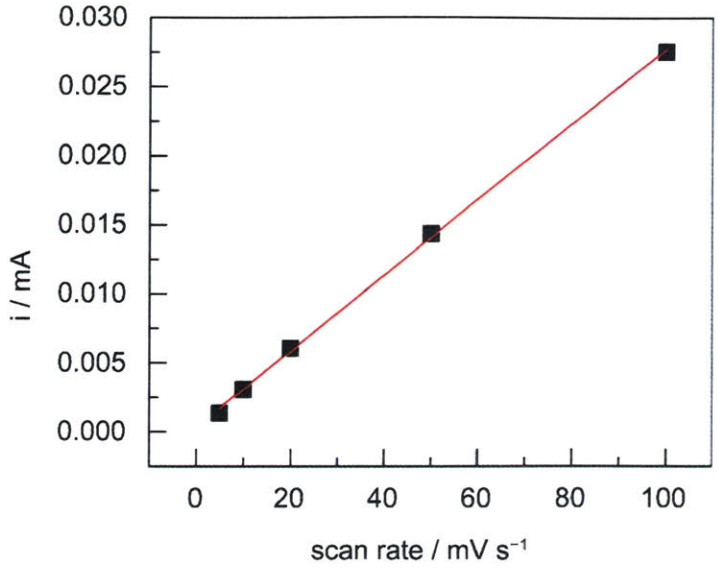

Figure 4.3. Representative double layer capacitance measurement of an Ag-IO prepared by passing 0.50 C/cm^2 of charge in the Ag electrodeposition. Double layer charging currents were sampled at 0.45 V by scanning between 0.40 and 0.50 V vs RHE.

The grain and surface structure of the Ag-IO is invariant with film thickness. X-ray photoelectron spectroscopy (XPS) confirms the presence of a pure Ag metal surface free of any detectable metal impurities (Figure 4.). Additionally, X-ray diffraction studies (Figure 4.c) reveal the presence of polycrystalline Ag with an average grain size of 35 nm, which is similar across all Ag-IO thicknesses. Thallium underpotential deposition (UPD)[6] was used to

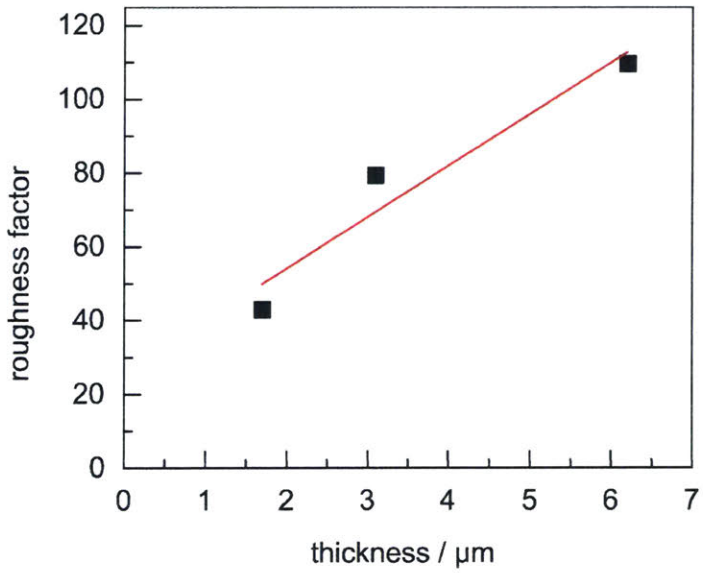

Figure 4.4. Roughness factor (RF, ECSA/Area$_{geometric}$) of Ag-IO films as a function of film thickness as determined by cross sectional SEM.

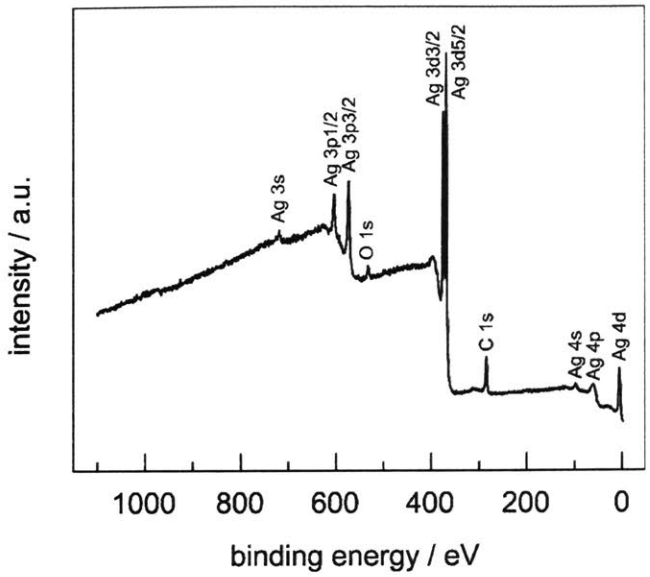

Figure 4.5. XPS (Al source) spectrum of a 1 C/cm^2 Ag deposited Ag-IO film. The survey spectrum shows metallic Ag on the surface with no metal impurities.

characterize the population of Ag surface facets present in each Ag-IO. A broad thallium UPD wave is observed in the cyclic voltammogram at −0.03 V (all potentials are reported versus the reversible hydrogen electrode, RHE) with a pronounced shoulder at −0.07 V and a subsequent small UPD wave at −0.15 V (Figure 4.d).[6] All of these features are well separated from the bulk deposition wave that onsets at −0.20 V. The UPD data is consistent with a broad distribution of surface exposed Ag facets. Importantly, the same UPD features appear with similar relative magnitudes over a range of Ag-IO thicknesses as well as nominally planar films deposited in the absence of the IO template. Together the data indicate that the bulk and surface composition and structure of these Ag films are largely invariant across a wide range of electrode thicknesses and porosities.

4.2.2 The impact of mesostructure on CO_2 electroreduction selectivity on Ag-IO electrodes

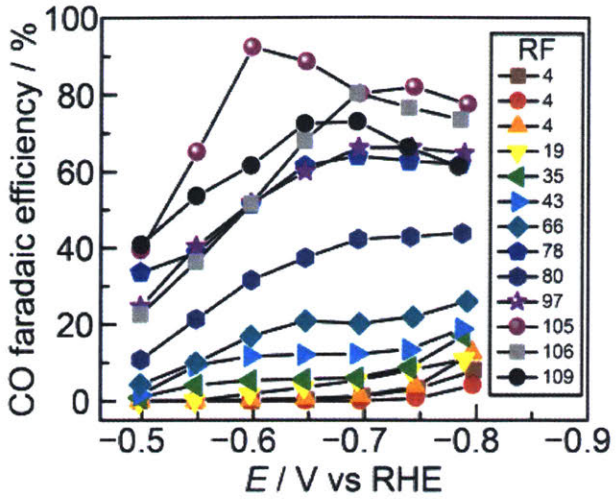

Figure 4.6. Faradaic efficiency for CO production as a function of applied potential for Ag films of varying RF. All data were collected in CO_2-saturated 0.1 M $KHCO_3$.

To probe the dependence of CO_2-to-fuels selectivity on the mesostructure of the electrode, we compared the performance of a variety of Ag-IO samples of different thickness as well as nominally planar Ag films (RF = ~4) deposited in the absence of an IO host template. Data were collected as a function of potential from −0.50 V to −0.80 V in CO_2-saturated 0.1 M $KHCO_3$ (pH 6.8) (Figure 4.). To effectively compare the data across both planar Ag films and Ag-IO films, the data are color coded by electrode RF. Planar Ag electrodes uniformly display very low selectivity for CO production over the entire range of the potentials explored (Figure 4.), with the onset of measureable CO selectivity occurring beyond −0.75 V. In contrast, we observe significantly enhanced faradaic efficiency (FE) for CO production for Ag-IO samples along with a general increase in CO selectivity as the Ag-IO thicknesses and electrode RF values increase. Indeed, for the thickest Ag-IO samples examined (~6.2 μm), which display roughness factors of >100, we observed appreciable CO selectivity at -0.50 V which rises to >80% at −0.70 V. Together the data indicate that, remarkably, increasing the electrode roughness factor via mesostructuring is sufficient to enhance the CO FE from <5% to >80 %.

We speculate that the plateauing, and in some cases down-turning, FE values for the highest roughness electrodes at potentials beyond −0.6 V may be due to the onset of CO_2 capturing to form carbonate species by increased OH^- concentrations that arise from the increased alkalinity of these highly diffusion limiting morphologies. In this scenario, CO_2 concentrations would also be lowered, leading to diminished FE for CO_2 reduction.

To determine the nature of the enhanced CO selectivity as a function of RF, we compared the specific activity for CO and H_2 production at a variety of potentials for Ag electrodes of varying porosities and thicknesses (Figure 4.). Specific current densities (j) were obtained by normalizing the partial currents of H_2 and CO production to the ECSA of each electrode. In CO_2-saturated 0.1 $KHCO_3$ electrolyte, the low RF planar Ag electrodes display

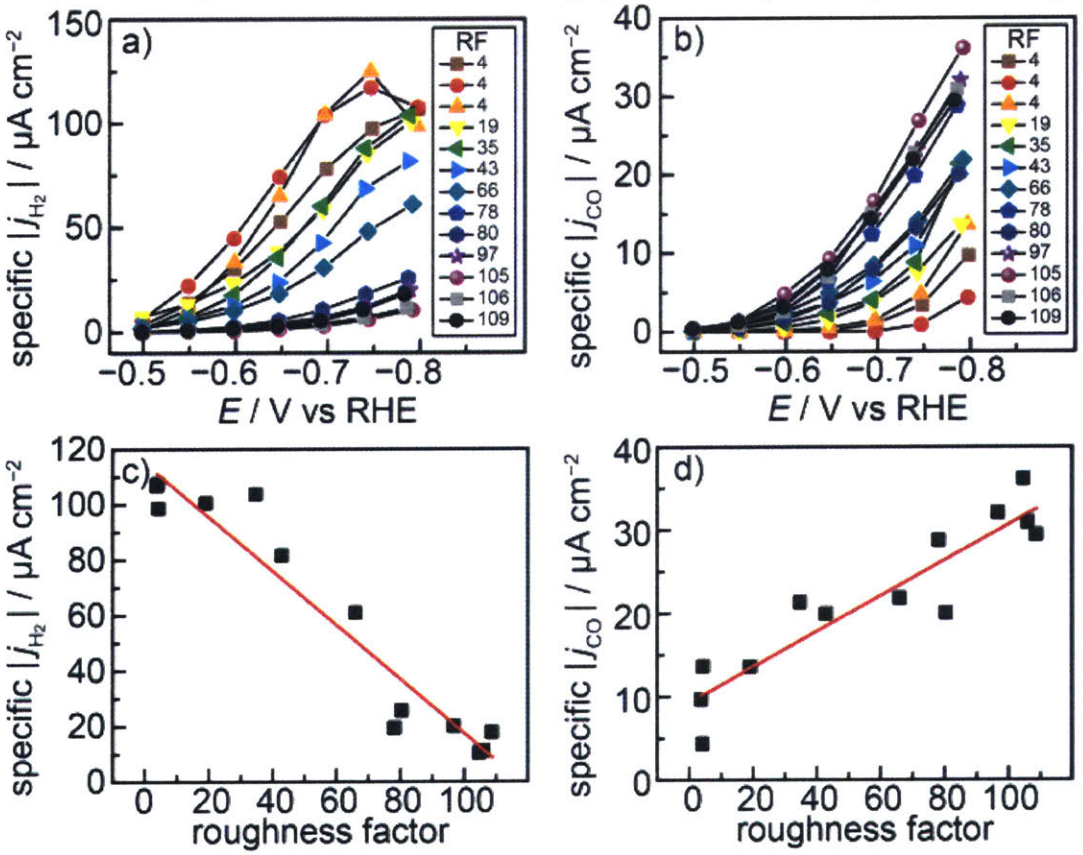

Figure 4.7. Specific current density for H_2 (a) and CO (b) evolution as a function of applied potential for Ag films of varying roughness factor (RF). Specific current density at −0.80 V for H_2 (c) and CO (d) evolution as a function of electrode RF. All data were collected in CO_2-saturated 0.1 M $KHCO_3$.

the highest specific activities for H_2 production over the entire potential range, whereas the thickest Ag-IO samples display the lowest j_{H2} values (Figure 4.a). Indeed, at −0.8 V, the specific activity for H_2 production declines systematically as a function of electrode RF with an ~10 fold decline over the range of electrode RF values explored here (Figure 4.c). These data are in line with our previous observations on Au-IO electrodes suggesting that H_2 suppression is a general phenomenon that arises intrinsically as a consequence of increased electrode mesostructure.

Remarkably, the suppression of H_2 production is not the only source of enhanced overall selectivity. In contrast to the behavior observed for H_2 production, the low RF Ag electrodes display the lowest specific activities for CO production over the entire potential range, whereas the thickest Ag-IO samples display the highest j_{CO} values (Figure 4.b). Indeed, at −0.8 V, the specific activity for CO production rises systematically as a function of electrode RF with a ~3 fold increase over the range of electrode RF values explored here (Figure 4.d). Together the data indicate that there is a synergistic interplay between simultaneous promotion of CO evolution and suppression of H_2 evolution that together, give rise to the dramatic improvement in overall CO_2-to-fuels selectivity. These results demonstrate that electrode mesostructuring is a powerful strategy for tuning CO_2-to-fuels selectivity and activity, independent of the surface structure and/or active site density of the catalyst.

4.2.3 The origin of CO_2 selectivity on mesostructured Ag electrodes

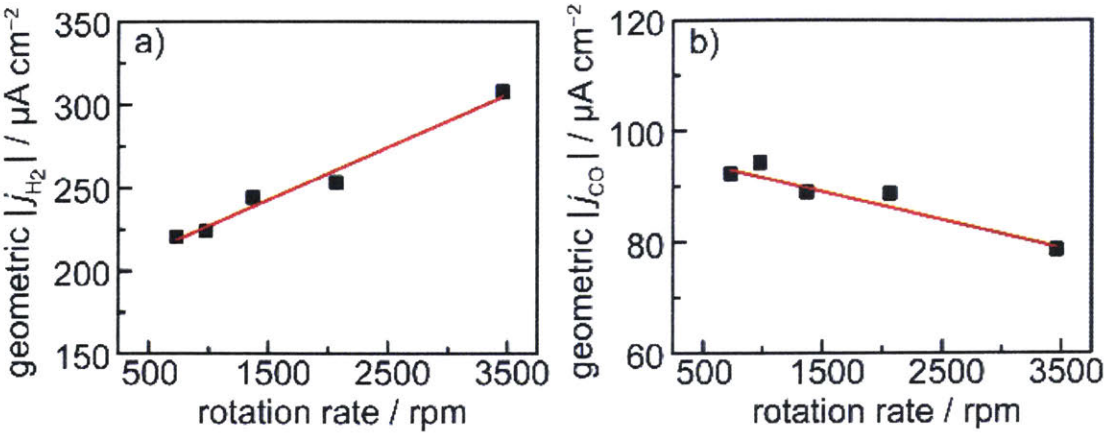

Figure 4.8. Geometric current density at −0.85 V for H_2 (a) and CO (b) evolution as a function of rotation rate for a Ag rotating cone electrode polarized in CO_2-saturated 0.1 M $KHCO_3$. Red lines serve as guides to the eye.

Whereas increasing the thickness and roughness of a Ag-IO serves to systematically amplify diffusional gradients at the catalyst surface, rotation of a planar Ag electrode achieves the opposite effect by inducing convective flow of electrolyte to the electrode. To amplify the diffusional gradients generated at the electrode surface, we conducted rotation rate dependent studies at a slightly more negative potential, −0.85 V, to induce a higher overall rate of catalysis. In line with the above results on Au-IO films, increasing the rotation rate of a polished polycrystalline Ag cone electrode serves to systematically increase the rate of H_2 production (Figure 4.a). We observe that the specific activity for H_2 production rises by ~40% by increasing the rotation rate from 700 to 3500 rpm. These results are similar to the behavior observed for Au-catalyzed H_2 production which is also enhanced with increasing rotation rate.[1] Mechanistic studies of Au electrodes indicate that the rate of H_2 evolution catalysis is highly sensitive to the local pH and buffer composition of the electrolyte that establish the proton donor environment at the electrode surface.[7] Thus, we postulate that the systematic suppression in H_2 evolution observed upon increasing electrode RF or decreasing rotation rate also results from an elevated local pH that serves to deplete the local concentration of proton donors at the

surface.

Increasing the rotation rate has the opposite effect on the rate of CO production. The specific activity for CO production declines by ~15% upon increasing the rotation rate from 700 to 3500 rpm (Figure 4.b). This observation is very unusual in heterogeneous electrocatalysis because it implies that accelerated mass transport serves, counter-intuitively, to impede the rate of CO production under these conditions. These results are also in contrast to observations on Au electrodes, for which the rate of CO production is largely independent of the electrode rotation rate.[1,7] Detailed mechanistic studies of Au-catalyzed CO production establish that CO_2 activation proceeds via rate limiting single electron transfer and adsorption of CO_2 rather than concerted electron-proton transfer,[7] making the reaction largely insensitive to the changes in the local proton donor environment. While an analogous mechanistic understanding of the activation-controlled kinetics of Ag-catalyzed CO production under these conditions does not exist and is the subject of ongoing investigations, we note that a strong dependence of CO production on the proton donor concentrations would give rise to the opposite of the effect observed here – systematic inhibition of CO production with increased RF. While we cannot rule out several competing effects,[8] we note that the local activity of K^+ and CO_3^{2-} must rise in tandem with elevated local pH and that these species may serve to promote CO production in this system.[9–12] Irrespective of the specific mechanism of promotion, these results highlight that electrode mesostructuring is a powerful tool for promoting the specific activity of the surface for CO_2-to-fuels catalysis.

4.2.4 Mesostructure induced CO_2 reduction selectivity is a general phenomenon

As demonstrated in Chapter 3 on Au surfaces and in this chapter on Ag surfaces, diffusion induced CO_2 selectivity appears to be a general phenomenon. This is due to the origin of diffusion limitations arising from the mesostructured morphology of the catalyst, rather than from some innate active site property for CO_2 activation. Since the publication of our observations of enhanced CO_2 selectivity on Au and Ag surfaces arising from mesostruture, the community has been receptive, and have shown similar results on Cu surfaces as well, demonstrating the general nature of this effect on Group 12 metals. In particular, Yang et. al. have shown that increasing diffusion limitations on ordered, porous Cu electrocatalysts systematically suppresses H_2 and CH_4 evolution, while also demonstrating surface area normalized promotion in C_2H_4 and C_2H_6 formation activity.[13] The suppression of H_2 evolution is in line with proton donor diffusion effects that are imposed by mesostructuring the catalyst. Likewise, the suppression of CH_4 with limited local proton availability is congruent with the mechanisms put forth by the community on the formation of CH_4, which is gated by a proton transfer step.[14,15] The increase in C_2H_4 and C_2H_6 formation activity may be attributed to increased local concentrations of critical intermediates, namely CO, which can more readily couple to form C_2 products in a locally high concentration environment.[16] In an applied sense, it appears that using mesostructured electrodes are more favorable in general for the purposes of suppressing H_2 evolution selectivity and maintaining or promoting CO_2 reduction activity.

It is important to note that the vast majority of CO_2 reduction electocatalysts reported in literature utilize high surface area catalysts comprised of complex, nanostructured surfaces or nanoparticles supported on porous networks,[17–24] often without reliable data on the real surface areas of the catalysts. In many cases, the activity and selectivity of these complex, nano/mesostructured catalysts are directly and sometimes solely attributed to the properties of

the surface active sites for substrate activation. While this may be true in some cases, our studies suggest that to accurately evaluate the performance of these catalysts, it is critical to also consider the impact of the catalyst morphology itself, as diffusion effects from mesostructured catalysts could very well be contributing to the observed selectivity and activity of the electrodes. Furthermore, we may expect diffusion limitations to have impacts on the activity of other electrocatalytic reactions as well, wherever competing pathways exist for selectivity.

4.3 Concluding remarks

By synthesizing a series of ordered mesostructured Ag electrodes, we have demonstrated that catalyst mesostructure induces both a dramatic suppression in the rate of the undesirable H_2 evolution reaction as well as a significant promotion in the rate of the desired CO_2-to-fuels reaction. This is in contrast to the results observed on Au in Chapter 3, where CO_2 reduction selecitivity is enhanced primarily by the suppression of H_2 evolution. As a result, we have shown that mesostructuring is in and of itself sufficient to tune the selectivity of CO_2-to-fuels catalysts from <5% to >80%. As any practical CO_2-to-fuels electrode must consist of a high degree of porosity, this work highlights that the local diffusional gradients that develop within these pores play a key role in defining CO_2-to-fuels conversion efficiency and selectivity. The work introduces electrode mesostructuring as powerful complementary strategy for promoting selective, efficient CO_2-to-fuels catalysis.

4.4 Experimental methods

Materials. Potassium bicarbonate (≥ 99.95% trace metals basis, Lot # MKBT3696V, Sigma-Aldrich), Techni Silver® Cyless® II RTU (Technic Inc.), IGEPAL® CO-520 (average M_n 441, Sigma Aldrich), Tl_2SO_4 (99.9995% metals basis, Puratronic, Alfa Aesar), perchloric acid (99.999%, Sigma Aldrich), sodium 3-Mercapto-1-propanesulfonate (technical grade, Sigma Aldrich), sodium hydroxide (99.99%, Sigma Aldrich), gold-coated (100 nm thick) glass slides (EMF corporation, 5 nm Ti adhesion layer), toluene (AR® ACS grade, Macron Fine Chemicals), titanium wire (99.99%, 1 mm dia., Alfa Aesar), and 200 nm Polybead® polystyrene spheres (Product# 07304, Polysciences Inc.) were used without modification or purification unless otherwise noted. CO_2-saturated 0.1 M $KHCO_3$, (pH 6.76) was prepared by sparging electrolyte solutions with CO_2 (Research Grade, Airgas) for 1 hour with rapid stirring. All electrolyte solutions were prepared with reagent grade water (Millipore Type 1, 18MΩ-cm resistivity) and purified of trace metal ion impurities by stirring in regenerated Chelex resin for at least 24 hours prior to use in electrolysis runs. Chelex® 100 Resin (Bio-Rad, Catalog # 210011676) was regenerated according to the manufacturer's protocol[25], with slight modifications. Specifically, Chelex was regenerated by stirring the as-received material for 12 hours in 1 M HCl (ACS Reagent Grade, EMD Chemicals) followed by rinsing with 9 L of reagent grade water. Subsequently, Chelex was placed in 1 M NaOH solution for 24 hours at 60°C with constant stirring. Chelex was then rinsed with 9 L of reagent grade water until the pH of the filtrate was 10.8.

General electrochemical methods. Experiments were conducted using a Biologic VSP 16-channel potentiostat or a Gamry Reference 600 potentiostat. With the exception of Ag electrodeposition, electrochemical measurements were performed in a 3-electrode setup with a high surface area Pt-mesh counter electrode (Alfa Aesar, 99.997%). Unless otherwise noted,

EDAQ leakless Ag/AgCl reference electrodes were used, and potentials are reported in V vs RHE using the following conversion: E(RHE) = E(Ag/AgCl) + 0.197 V + 0.059(pH). All experiments were performed at ambient temperature, (21 ± 1 °C).

Synthesis of Ag inverse opals. Silver inverse opals were prepared by electrodeposition of silver into the voids of a polystyrene colloidal crystal host template. Gold-coated glass slides were cleaned by immersion in freshly-prepared piranha (prepared by slowly adding one part 30 % hydrogen peroxide to three parts conc. sulfuric acid by volume; caution: **piranha solutions are potentially explosive if the peroxide fraction rises above 50%**) without additional heating for one hour. After rinsing with copious amounts of reagent grade water, the cleaned gold-coated glass slides were immersed in an aqueous solution of 10 mM sodium 3-mercapto-1-propanesulfonate overnight, followed by rinsing with copious amounts of reagent grade water. The slides were then fully immersed at a ~70° angle in a 10 mL aqueous bath containing 0.04 wt % polystyrene spheres. The solvent was allowed to evaporate completely by heating in a temperature-controlled oven at 55 °C for 4-5 days to yield a white film (the quality of the crystal was judged by the observation of green diffraction which can be seen at some angles) coating the gold-coated glass slide. The colloidal crystal films were then heated to and sintered at 99 °C for 75 minutes to provide pore connectivity in the inverse opal host template. The colloidal crystal films were then contacted to Ti wires and secured with Parafilm® (Heathrow Scientific) to fabricate working electrodes. The colloidal crystal films were then immersed into the silver electroplating bath prepared by adding 0.1 mL of CO-520 IGEPAL surfactant to 50 mL of commercial Technic Ag electrodeposition solution. The added surfactant is essential for ensuring good solution infiltration into the polystyrene film. Silver was electrodeposited galvanostatically using a 2-electrode setup with no reference electrode at a constant current of -2.5 mA/cm^2 until a total charge of between 0.5 and 2 C/cm^2 had passed.

A Ag foil (99.998%, metals basis, Puratronic, Alfa Aesar) was used as the counter electrode to replenish Ag^+ ions into the solution during deposition. The working and counter electrodes were held parallel to each other at a separation of between 0.5 and 1 cm to promote uniform deposition. The deposition bath was sparged with N_2 and stirred using a pea shaped stir bar at 1200 rpm. Samples of varying thickness (Figure 4.) and roughness factor (Figure 4.) were obtained by varying the deposition charge between 0.5 and 2 C/cm^2. The polystyrene spheres were subsequently dissolved by washing the thin films with copious amounts of toluene and by immersion in a toluene bath for 12 hours with constant shaking. The samples were then washed with copious amounts of toluene, dried, and then washed further with copious amounts of water. Nominally planar Ag samples were obtained by directly electrodepositing $1C/cm^2$ Ag onto planar gold substrates using the same electrodeposition conditions and bath composition, followed by identical water and toluene washing procedures.

Scanning electron microscopy (SEM). Following electrodeposition, Ag-IOs films were rinsed with copious amounts of milliQ water and allowed to dry in air. The glass slides were then cleaved and imaged in profile and top down using a Zeiss Merlin field emission-SEM with an acceleration voltage of 5 keV to produce the images shown in Figure 4.a and b.

X-ray diffraction (XRD). XRD patterns were collected for a flat Ag film and for Ag-IO's of 0.5, 1, and 2 C/cm^2 of Ag deposition to produce Figure 4.c. A Bruker D8 Advance diffractometer with a Cu source (λ = 1.504 Å) was used. The Scherrer equation[26] with a shape factor of K = 0.94 (Scherrer constant) was used to determine the average grain size in the Ag-IO at the [111] reflection (38.2°). The peaks were normalized in intensity to the [111] reflection.

Scherrer Equation: $D = \frac{K\lambda}{\Delta(2\theta)\cos(\theta[111])}$

Legend:

D = average diameter (nm)

K = Scherrer constant

λ = X-ray wavelength (nm)

$\Delta(2\theta)$ = full width at half max intensity value of [111] reflection peak in rads

θ[111] = peak center of [111] refection.

Surface area and roughness factor determination by double layer capacitance (DLC). The electroactive surface areas of the Ag-IO films were determined by analysis of the double layer capacitance of each electrode. Surface areas were determined at the end of each series of catalysis runs over a range of potentials. Non-faradaic double layer charging currents were sampled between 0.4 and 0.5 V vs RHE at scan rates of 5, 10, 20, 50, and 100 mV/s (Figure S2). The total charging current at a given scan rate was determined by subtracting the cathodic from the anodic capacitive current at 0.45 V. These capacitive currents were plotted vs scan rate and the slope of this plot was divided by 2 to obtain the electrode capacitance (F). The electrochemically active surface area (ECSA) was then determined by dividing the electrode capacitance by the known double layer capacitance, 25 $\mu F/cm^2$, of a planar silver Ag surface.[5] The electrode roughness factor values (plotted in Figure 4., Figure 4., and Figure 4.) were determined by dividing the ECSA values by the respective geometric surface area of each electrode.

Thallium underpotential deposition (UPD). Surface terminations of the Ag-IO films were determined by thallium underpotential deposition.[27] A Hg/Hg_2SO_4 (CH Instruments) reference electrode was used. The reference electrode was stored in saturated K_2SO_4 and periodically checked against a pristine reference to ensure again potential drift. The following

relation was used to report potentials in V vs RHE: E(RHE) = E(Hg/Hg_2SO_4) + 0.64 V + 0.059(pH). Experiments were conducted with N_2 sparging and with no stirring. The Ag-IO films were cycled from −0.65 V to −1.2 V vs Hg/Hg_2SO_4 (pH = 3, $HClO_4$) at a scan rate of 10 mV/s in N_2-saturated 0.5 M Na_2SO_4 containing 0.075 M Tl_2SO_4. The currents were normalized to the broad reductive wave at −0.03 V. This procedure was used to produce the data in Figure 4.d.

X-ray photoelectron spectroscopy (XPS). The XPS spectrum was taken with a PHI Versaprobe II XPS with a monochromated Al (1486.6 eV at 45.6 W) X-ray source and a beam diameter of 200.0 μm. The pass energy of the measurement was 187.85 eV. These parameters were used to generate the survey spectra in Figure 4..

Electrocatalytic CO_2 reduction. Electrode potentials were corrected for the uncompensated Ohmic loss (iR_u) in situ via the current interrupt method. R_u values were measured using the R_u test function in the Biologic software. In situ iR_u compensation levels were set to 85 – 90 % of the measured R_u values and the residual voltage loss was accounted for mathematically during data workup. All electrolyte solutions were used as both the catholyte and the anolyte, and the working electrode chamber was stirred at a constant rate of 800 rpm during all experiments using a grain sized stir bar. In all cases, experiments were conducted in an airtight H-cell with 17.5 mL catholyte and 7.5 mL anolyte separated by an anion exchange membrane (AGC Selemion membrane). All H-cells were cleaned by immersion in piranha solution without additional heating for one hour and rinsing with MilliQ water prior to each experiment. During all experiments, the catholyte was sparged continuously with research grade CO_2 at 10 sccm, whereas the anolyte was sparged continuously with N_2. Prior to the start of each experiment, the catholyte was sparged with CO_2 at 30 sccm for 1 hour to equilibrate the solution. During electrolysis, evolved gases were quantified using in-line gas

chromatography as described below. This protocol was used to collect all electrolysis data. All current values are reported as specific current density values, which are obtained by normalizing to the ECSA of the working electrodes as measured by double layer capacitance following the electrolysis run. This procedure was used to collect data in Figure 4. and Figure 4..

Product distribution analysis. Electrolysis product distributions were measured using an in-line gas chromatograph (SRI Instruments, Multi-Gas Analyzer #3) equipped with a thermal conductivity detector, methanizer, and flame ionization detector in series following Molsieve 13x and Hayesep D columns. Electrodes were polarized at various potentials sufficient for CO_2 reduction catalysis while CO_2 was continuously sparged at a flow rate of 10 sccm. GC traces were collected every 20 min. The partial specific current density (specific $j_{product}$) for each evolved gaseous product was calculated using the following relationship: $j = n_eF*[p]*\text{flow rate}*P/RT*1/A$, where [p] is the ppm value of the product measured via GC using an independent calibration standard gas mixture, P is the pressure in the electrochemical cell headspace (1.1 atm), T is the temperature, R is the gas constant, , n_e is the number of electrons transferred per equivalent of the given product, F is Faraday's constant, and A is the ECSA of the electrode as calculated using DLC (described above). Faradaic efficiency values were determined by dividing specific $j_{product}$ by specific j_{total}. This procedure was used to collect data in Figure 4., Figure 4., and Figure 4..

Rotating cone electrode measurements. A silver rotating cone (r = 0.25cm, 45°cone angle, custom milled) was employed as the working electrode. Electrode rotation was controlled using a Metrohm Autolab B.V. rotator that formed an air-tight seal with the working compartment of the H-cell. The electrodes were polished sequentially using 1 μm and 0.3 μm alumina and sonicated using a bath sonicator for 5 min prior to each experiment. Rotation rate

dependent product distributions were measured by conducting controlled potential electrolyses at −0.85 V in CO_2-saturated 0.1 M $KHCO_3$. Prior to each chronoamperometry run, the electrode was held at the open circuit potential for 10 seconds. For a given rotation rate, a GC trace was taken after steady state was reached and the generated gases were equilibrated in the headspace (after ~19 min). The rotation rate was varied in the following order, 2066, 976, 3460, 730, 1371 rpm to ensure against systematic errors due to electrode history. The rotation sequence was performed twice, and the reported data in Figure 4. is that of the second series, which displays stable electrode partial current behavior without systematic deactivation. Partial current densities for CO and H_2 production were determined by in-line gas chromatography as described above. As these rotation rate dependence studies utilize lower surface area electrodes and examine relatively small changes in electrode activity, we found that it was critical to eliminate trace contaminants by using Chelex-purified ultra-pure electrolyte.

4.5 References

(1) Hall, A. S.; Yoon, Y.; Wuttig, A.; Surendranath, Y. J. Am. Chem. Soc. **2015**, 137 (47), 14834.

(2) Ma, M.; Trześniewski, B. J.; Xie, J.; Smith, W. A. Angew. Chemie Int. Ed. **2016**, 9748.

(3) Shimmin, R. G.; DiMauro, A. J.; Braun, P. V. Langmuir **2006**, 22 (15), 6507.

(4) Hung, D.; Liu, Z.; Shah, N.; Hao, Y.; Searson, P. C. J. Phys. Chem. C **2007**, 111 (8), 3308.

(5) Motheo, A. J.; Machado, S. A. S.; Kampen, M. H. Van; Santos Jr., J. R. J. Braz. Chem. Soc. **1993**, 4 (3), 122.

(6) Bewick, A.; Thomas, B. J. Electroanal. Chem. Interfacial Electrochem. **1977**, 84 (1), 127.

(7) Wuttig, A.; Yaguchi, M.; Motobayashi, K.; Osawa, M.; Surendranath, Y. Proc. Natl. Acad. Sci. **2016**, 113 (32), E4585.

(8) Rosen, J.; Hutchings, G. S.; Lu, Q.; Rivera, S.; Zhou, Y.; Vlachos, D. G.; Jiao, F. ACS Catal. **2015**, 5 (7), 4293.

(9) Strmcnik, D.; Uchimura, M.; Wang, C.; Subbaraman, R.; Danilovic, N.; van der Vliet, D.; Paulikas, A. P.; Stamenkovic, V. R.; Markovic, N. M. Nat. Chem. **2013**, 5 (4), 300.

(10) Tong, Y. J. Chem. Soc. Rev. **2012**, 41 (24), 8195.

(11) Verma, S.; Lu, X.; Ma, S.; Masel, R. I.; Kenis, P. J. A. Phys. Chem. Chem. Phys. **2016**, 18 (10), 7075.

(12) Thorson, M. R.; Siil, K. I.; Kenis, P. J. a. J. Electrochem. Soc. **2012**, 160 (1), F69.

(13) Yang, K. D.; Ko, W. R.; Lee, J. H.; Kim, S. J.; Lee, H.; Lee, M. H.; Nam, K. T. Angew. Chemie Int. Ed. **2017**, 56 (3), 796.

(14) Kortlever, R.; Shen, J.; Schouten, K. J. P.; Calle-Vallejo, F.; Koper, M. T. M. J. Phys. Chem. Lett. **2015**, 6 (20), 4073.

(15) Gattrell, M.; Gupta, N.; Co, A. J. Electroanal. Chem. **2006**, 594 (1), 1.

(16) Cheng, T.; Xiao, H.; Goddard, W. A. Proc. Natl. Acad. Sci. **2017**, 114 (8), 1795.

(17) Li, C. W.; Kanan, M. W. J. Am. Chem. Soc. **2012**, 134 (17), 7231.

(18) Chen, Y.; Li, C. W.; Kanan, M. W. J. Am. Chem. Soc. **2012**, 134 (49), 19969.

(19) Lee, C. H.; Kanan, M. W. ACS Catal. **2015**, 5 (1), 465.

(20) Lu, Q.; Rosen, J.; Zhou, Y.; Hutchings, G. S.; Kimmel, Y. C.; Chen, J. G.; Jiao, F. Nat. Commun. **2014**, 5.

(21) Reske, R.; Mistry, H.; Behafarid, F.; Roldan Cuenya, B.; Strasser, P. J. Am. Chem. Soc. **2014**, 136 (19), 6978.

(22) Zhu, W.; Michalsky, R.; Metin, Ö.; Lv, H.; Guo, S.; Wright, C. J.; Sun, X.; Peterson, A. A.; Sun, S. J. Am. Chem. Soc. **2013**, 135 (45), 16833.

(23) Kim, D.; Resasco, J.; Yu, Y.; Asiri, A. M.; Yang, P. Nat. Commun. **2014**, 5, 4948.

(24) Zhu, W.; Zhang, Y.-J.; Zhang, H.; Lv, H.; Li, Q.; Michalsky, R.; Peterson, A. A.; Sun, S. J. Am. Chem. Soc. **2014**, 136 (46), 16132.

(25) Bio-Rad Laboratories. Chelex® 100 and Chelex 20 Chelating Ion Exchange Resin Instruction Manual http://www.bio-rad.com/webmaster/pdfs/9184_Chelex.PDF (accessed Jun 25, 2016).

(26) Langford, J. I.; Wilson, A. J. C. J. Appl. Crystallogr. **1978**, 11 (2), 102.

(27) Herrero, E.; Buller, L. J.; Abruña, H. D. Chem. Rev. **2001**, 101 (7), 1897.

Chapter 5 – Tuning hydrocarbon selectivity on Cu catalyzed CO_2 reduction: kinetic insights and electrodeposition to generate catalysts

This chapter contains text from the following unpublished article:

(1) Schreier, M; Yoon, Y; Jackson, M. N.; Surendranath, Y. Competition between H and CO for active sites governs Cu mediated electrosynthesis of hydrocarbon fuels. Angew. Chem. Int. Ed. **2018**. Submitted.

Publication contribution notes:

The author contributed to the design of the experiments, to the electrochemical measurements, and to the kinetic analysis.

5.1 Introduction

As described in earlier chapters, Cu electrodes stand out in catalyzing the electrochemical conversion of CO_2 to various hydrocarbons with relatively high selectivity. As such, Cu catalysts are an attractive candidate for designing direct CO_2 electroreduction systems. However, Cu catalysts generally suffer from poor selectivity, and generate a complex mixture of CH_4, C_2H_4, H_2, and various oxygenates.[1] While computational models offer insight into the pathway of CO_2 reduction to CO, and further to other hydrocarbons, there is a lack of experimental evidence describing the elementary steps in the pathway of CO intermediate reduction to the various hydrocarbons. Although experimental strategies such as imposing diffusion limitations on the proton donor and tuning the CO binding affinity of the catalyst has led to enhancements in the selectivity for C_2 and C_3 products while suppressing H_2 evolution, there remains much to be explored about the microkinetic steps that dictate the selectivity of CO_2 and CO reduction on Cu sites.[2–4] Thus, the systematic design of improved catalysts relies on understanding the key reaction steps that gate the formation of one product over another. In this chapter, kinetic studies on the origin of selectivity of H_2, CH_4, and C_2H_4 on Cu will be

discussed, followed by a discussion of attempts to directly engineer electroactive Cu defect sites with high CO affinity for selective CO_2 reduction.

5.2 Results and discussion

5.2.1 Pathways for CO intermediate reduction on Cu

On Cu, it is widely accepted that surface-bound carbon monoxide (CO_{ads}) serves as the key intermediate en route to hydrocarbons and oxygenates.[5–7] However, little is known experimentally about the reaction pathway of CO reduction via multiple proton and electron transfers. In particular, surface-bound CO can react with each other reaction species in two major pathways: by reacting with other surface-bound species in a "Langmuir-Hinshelwood" (LH) step or by reacting with a solution species in an "Eley-Rideal" (ER) step.[8] For the formation of methane, the rate-limiting hydrogen transfer to CO can proceed via either mechanism as shown in Figure 5..[9] Similarly, electron transfer coupled C-C bond formation between two CO molecules to make ethylene and other C_2 products may proceed via LH or ER steps.[9]

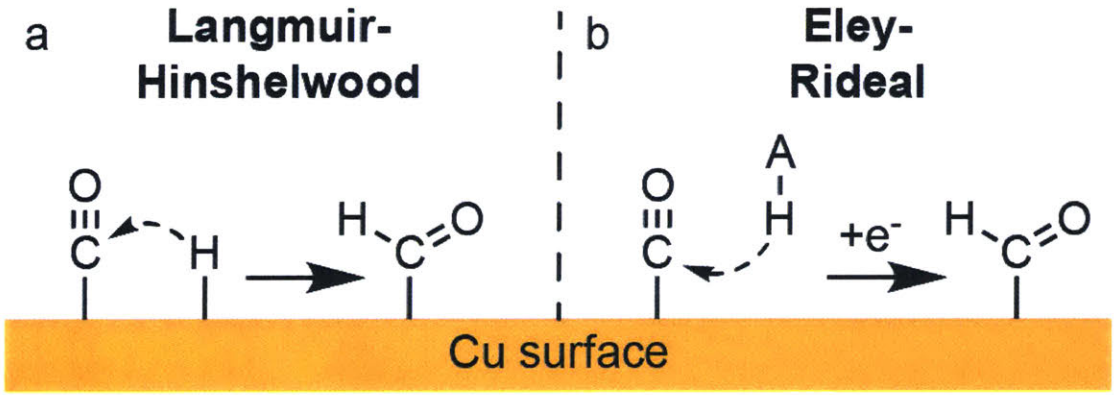

Figure 5.1. Schematic of Langmuir-Hinshelwood (a) and Eley-Rideal (b) mechanisms in the hydrogenation of surface-bound CO to a putative formyl intermediate toward the production of methane.

Insight into this mechanistic distinction is essential for the design of efficient CO_2 reduction catalysts. For example, in an ER mechanism leading to methane, simply increasing the surface concentration of CO at the expense of H adsorption is sufficient to promote higher-order product formation relative to H_2 evolution. In contrast, for an LH mechanism, both H and

CO affinity must be simultaneously optimized. In this case, the product distribution will invariably show a complex dependence on CO and H surface populations and competition for sites, as well as their reaction rates, requiring more nuanced catalyst design.

5.2.2 Competition between H and CO intermediates on the hydrocarbon selectivity on Cu

While direct measurement of the kinetic parameters gating CO_2 and CO reduction in aqueous bicarbonate electrolyte where CO_2 reduction is typically performed is preferred, this has been limited by the low solubility of CO in water (1.1 mM).[10] The low solubility of CO severely limits the range at which CO activation controlled kinetics can be observed without running into diffusion limitations. Therefore, electrochemical measurements were carried out in an analogous electrolyte environment with improved CO solubility.

The CO electroreduction measurements were carried out using electropolished Cu foil in ethanol solution containing 0.1 M lithium bis(trifluoromethanesulfonyl)imide (LiTFSI) at −35 °C, and products were analyzed by in-line gas chromatography (see Section 5.4 for details). In the absence of CO, H_2 evolution was observed with quantitative faradaic efficiency, indicating that the electrolyte is a suitable medium for reductive electrolysis.

Information about interfacial reaction kinetics was obtained by analysis of Tafel plots of log(j) versus E (Ag/AgCl (3 M NaCl)). Figure 5. shows data for CH_4, H_2 and C_2H_4 over partial CO pressures (p_{CO}) from 0.1 (red) to 1.0 atm (violet). The observed Tafel slope and transfer coefficient ($\alpha = 2.303RT/F * d\log(j)/dE$) provide information about the number of electrons transferred between the resting state and the rate-limiting step (RLS) of the catalytic cycle.[11] For clarity, Figure 5. excludes diffusion-limited data points observed at low p_{CO}. The reported Tafel slopes are the averages of four repeat measurements. Importantly, the observed changes upon varying the partial pressure of CO are reversible, indicating that the dependence on p_{CO} is not convoluted by irreversible changes to the electrode over the course of the measurement.

We begin by analysing CH_4 production (Figure 5.a) which exhibits linear Tafel

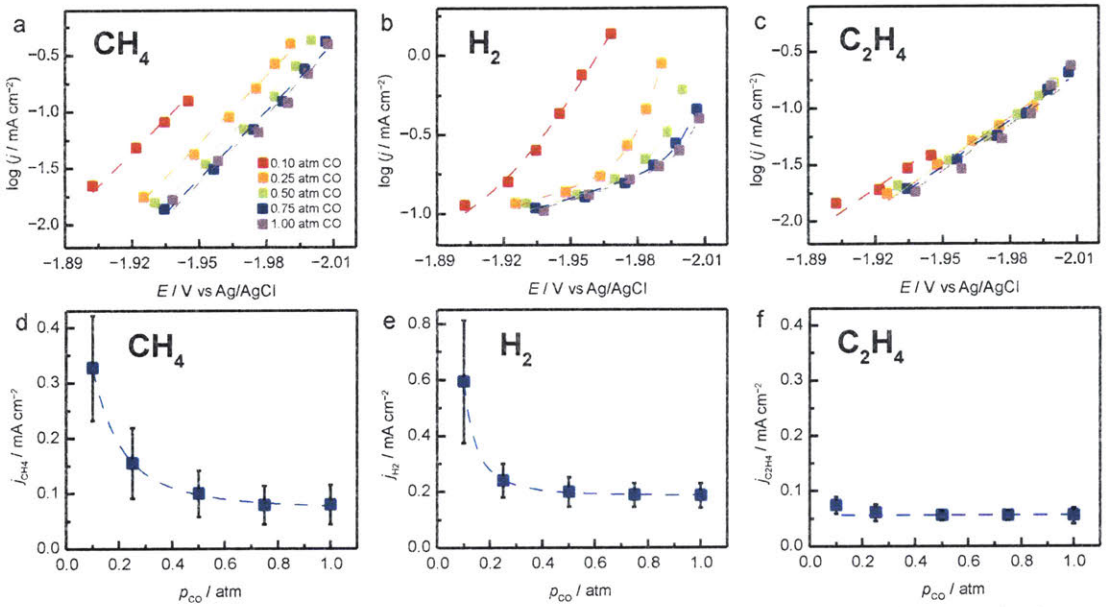

Figure 5.2. Tafel plots of the partial current density of methane production (a), hydrogen evolution (b) and ethylene production (c) under varying partial pressures of carbon monoxide in 0.1M LiTFSI / EtOH at -35 ℃. Dashed lines correspond to fitted data. Partial current densities vs CO pressure at -1.96 V from methane (d), hydrogen (e) and ethylene (f). Data correspond to the average and standard deviation of four independent measurements. Dotted lines in d, e, and f serve as guides to the eye.

behaviour. The Tafel curves remain parallel with changing CO pressure, showing a slope of 54 +/– 3 mV dec^{-1} with an empirical transfer coefficient of 0.9 at −35 °C.

CH_4 production is dramatically suppressed upon increasing CO partial pressure, with the Tafel curves shifting progressively to higher overpotentials (Figure 5.a), corresponding to a strong decline in j_{CH4} at constant bias (Figure 5.d). Considering that the rate determining step is considered to be the formation of a surface formyl (CHO_{ads}) from CO_{ads}, the observation of a negative order in p_{CO} and a transfer coefficient of 0.9 is strongly indicative of a LH type mechanism with pre-equilibirum electron transfer before the rate limiting step[7,9,12,13]. In this mechanism, CO_{ads} and H_{ads} competing for sites on the Cu surface would come together to form CHO_{ads} in a rate limiting step.

Similarly, the rate of H_2 formation is also suppressed by p_{CO}, with an observed transfer coefficient in the presence of CO of 2.1 from a 22 mV dec^{-1} Tafel slope, indicative of two pre-

equilibrium electron transfers to protons to form two surface H_{ads}. The data suggest a rate limiting combination of H_{ads} for the formation of H_2. Because H_{ads} must share sites with CO_{ads}, the negative order in p_{CO} is expected for H_2 evolution (Figure 5.3).

Remarkably, the formation of C_2H_4 has little dependence on p_{CO} within the probed range of partial pressure, with a transfer coefficient of 0.6, suggesting rate limiting single electron transfer. The single electron dependence is congruent with literature predictions of a rate limiting CO coupling step mediated by single electron transfer.[7] While both ER and LH mechanisms would predict rate limiting electron transfer, the lack of p_{CO} dependence over the measured range rules out an ER pathway, which would have positive order in CO. Instead, the data suggest a LH pathway in the limit of CO_{ads} saturation on the surface (Figure 5.3).

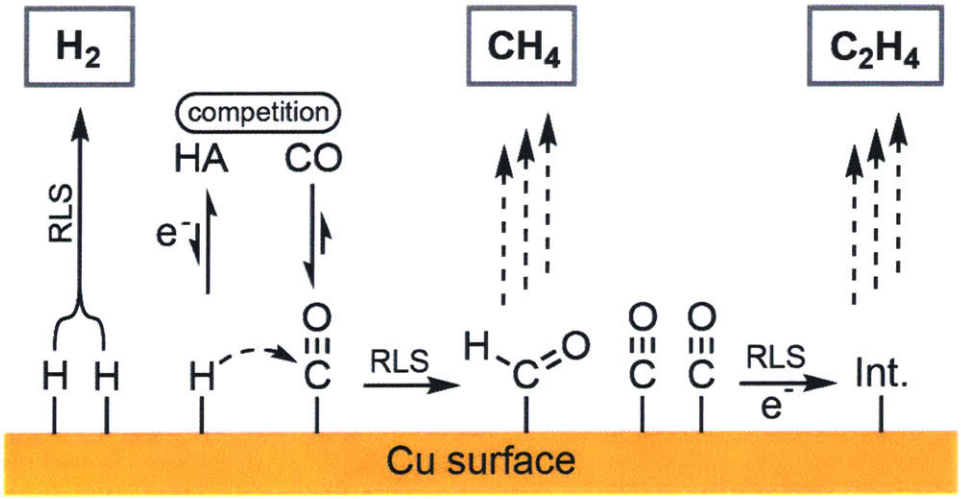

Figure 5.8. Proposed mechanistic model for methane, ethylene and hydrogen production duri ng the electrochemical reduction of CO

Combining these mechanistic insights, it is possible to speculate on strategies to improve product selectivity for CO_2 reduction. For improving the selectivity for C_2H_4, having a high concentration of both solution and surface CO appears to be beneficial in suppressing CH_4 and H_2 evolution. Such selectivity could be achieved by pressurizing the electrochemical cell with CO (or its precursor, CO_2), by having highly rough electrodes with locally concentrated CO, or by having an abundance of surface sites with a strong affinity for CO_{ads}

over H_{ads}. To increase the intrinsic activity of C_2H_4 formation, the cell would likely require surface sites that have both high CO_{ads} coverage and a low barrier to C-C coupling. In contrast, efficient CH_4 production requires high concentrations of both H_{ads} and CO_{ads} while suppressing H-H formation. This may be realized by designing catalyst materials which feature saturated CO regions adjacent to isolated H sources, such as single atom sites or oxide phases, which allow for H atom spillover but do not lead to rapid H_2 production themselves.

5.2.3 Cu defect sites for enhanced hydrocarbon selectivity during CO_2 reduction

As discussed previously, one strategy to improve CO_2 reduction selectivity to C_2 products on Cu, particularly with the goal of minimizing separation costs, is to increase the population of sites saturated with CO that suppress H_2 and CH_4 formation from competing LH pathways. To increase the population of sites with high CO saturation, it is important to consider the energetics of CO_{ads} on Cu. The ability of bulk Cu electrodes over other transition metals to produce a wide variety of CO_2 reduction and CO reduction products at moderate potentials is rationalized, in part, by Cu's optimal CO energy of adsorption; Cu binds CO strongly enough to maintain high surface coverage, but not strong enough to inhibit subsequent reaction.[6,14]

However, not all Cu surfaces behave the same in CO_2 and CO reduction in terms of the product distribution and the required overpotential (η), the potential required in excess of the thermodynamic value to drive the reaction at a desired rate. Unique to solid-state heterogeneous catalysts, studies have shown that different facets of the face-centered-cubic (FCC) Cu lattice have different electrocatalytic profiles for CO_2 and CO reduction. Notably, CO_2 and CO reduction on low index [100] facets produce more C_2 products such as ethylene over the [111] facet.[6,15,16]

The cause of such diverse reactivity in extended solids can be rationalized in part by the local atomic coordination environment of the surface Cu atom. A surface atom on the face-centered-cubic (FCC) Cu [111] facet is coordinated locally by 9 nearest neighboring Cu atoms, while atoms on [100] and [110] facets have 8 and 7 nearest Cu atoms, respectively (Figure 5.). Under-coordinated surface atoms exhibit a greater CO adsorption strength [111], [100], and [110] facets correspond to 47, 51, and 54 kJ/mol, respectively.[17] This can be rationalized due to the local decrease in d band spread for an under-coordinated surface Cu atom as a result of

decreased neighboring bonding interactions. Because the bulk Fermi level must be maintained at the surface, the Cu d-band must shift up in energy to the bulk Fermi level. In reaction to the rise in d band energy, the binding orbitals of the adsorbate CO are stabilized, leading to greater adsorption strength at under-coordinated Cu sites.[18]

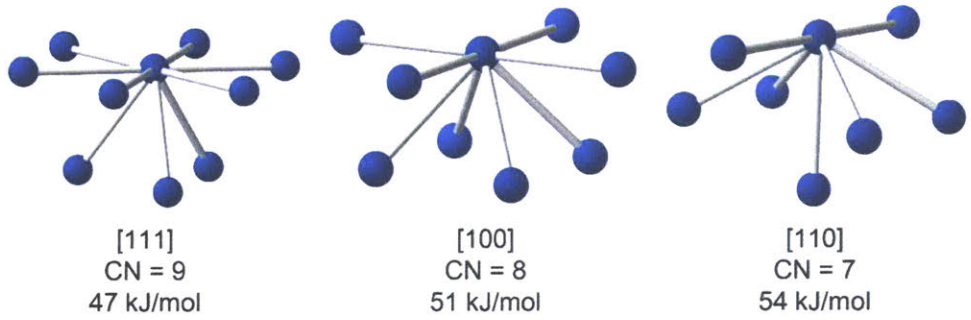

Figure 5.4. Atomic coordination of surface Cu atoms at [111], [100], and [110] facets, and their CO heats of adsorption.

While single crystal studies of Cu catalyzed CO_2 reduction offer great insight, typical electrode surfaces are polycrystalline systems that are rich in defects and grain boundaries exhibiting a wide range of electrocatalytic profiles.[5,12,19–24] In particular, reports on thick, oxide-derived (OD, oxidized and back-reduced) Cu films with complex, nano and mesostructured morphologies have shown exceptional activity for CO_2 and CO reduction, which is not explained by known facet reactivity alone.[5,23] CO_2 reduction on thick OD-Cu films at pH 6.7 with $NaHCO_3$ buffer produces CO at 45 % Faradaic efficiency (FE) as low as −0.3 V vs RHE and formate at 40 % at −0.55 V with no precedence in single crystal Cu studies[6,16]. Similarly, CO reduction on OD-Cu in pH 13 KOH electrolyte produces acetate and ethanol in high FE yields (20~50 %) between potentials as low as −0.25 to −0.5 V, whereas single crystal [111] and [100] Cu surfaces do not produce these products at significant amounts between 0 to −1.0 V.[15,16] The enhanced catalytic activity has been attributed to relatively stable bulk grain boundaries in these OD systems.[5,23,25,26] Grain boundaries occur between neighboring crystallite domains (grains) which are lattice misoriented to varying degrees with each other.

Therefore, generating Cu surfaces enriched with grain boundary defect sites may promote C_2 selectivity.

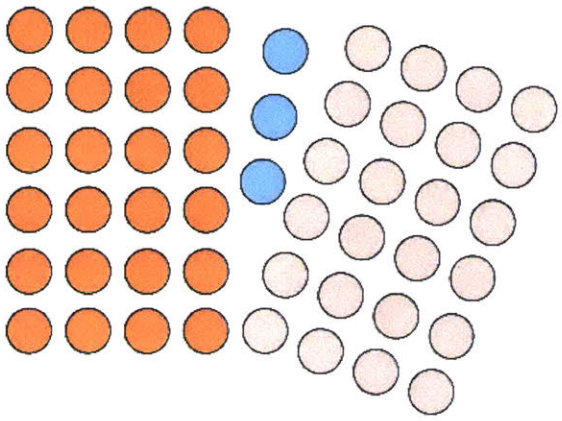

Figure 5.5. Grain boundary region (blue) between misaligned [100] facets.

As with facets, the thermodynamics of CO adsorption on putative grain boundary active sites is expected to differ from ordered facets due to differences in the strain and under-coordination of grain boundary Cu atoms. Unlike well-ordered Cu atoms on surface facets, the atoms in the boundary region are subject to a strained local lattice, with deviations in equilibrium bond lengths and local coordination environments[27] (Figure 5.). This is the result of lattice mismatch stresses that are exerted on the lattice of the grain boundary, which can vary depending on the extent of grain misorientation.[27–30] The existence of such under-coordinated atoms at grain boundariess and defect sites may explain the increased CO adsorption energy (58 kJ/mol) on polycrystalline Cu.[17]

5.2.4 Synthesis of grain boundary rich Cu electrodes

Despite the high activity of OD-Cu systems, the process of oxidation and back reduction of thick films offers only limited control in tuning the size of grains and their corresponding boundary density. While the thickness of OD films can be empirically modified by varying annealing conditions, there is little control over grain size, porosity, and other structural effects.[5,23] Therefore, a systematic study of grain sizes and corresponding boundary density on electrocatalysis may be achieved using a "bottom-up" strategy, where grains are grown with size selectivity. However, it is not necessarily clear how certain types of grain boundaries can be readily built into the catalyst.

Despite this synthetic limitation for building in specific grain boundary types, we chose electrodeposition due to its versatility in controlling nucleation and growth of small crystallites, allowing access to various grain sizes and grain boundary densities at the <50 nm regime.[31–33] Electrodeposition is also attractive because it can directly control the thickness of the catalyst films by monitoring the charge passed during film growth, giving increased structural control. Furthermore, electrodeposition is amenable to long range mesostructuring via the infilling of templates such as block co-polymers and inverse-opals, allowing for control of local molecular concentration gradients at the electrode.[34] In contrast, traditional methods of grain engineering in material science, which involve a series of stress-annealing of polycrystalline foils, have not been able to access the <50 nm grain regime with a good degree of grain monodispersity, and were thus unsuitable for this study.[27–30,35] Although colloidal nanoparticles of Cu can be synthesized with a great degree of size and morphology control, the fusing of individual Cu nanoparticles to make grain boundaries can present additional challenges, while the surface structure of these nanoparticles are further complicated by a large presence of strongly coordinated organic surfactants leftover from synthesis.[36] Given the deficiencies of these

methods, we sought to develop an electrochemical route that could control the rate of nucleation and growth of small crystallites, leading to controlled deposition of morphology and size tunable grains.

Initially, we varied the Cu deposition potential to control Cu nucleation rates towards obtaining different grain sizes. To access a wide range of Cu deposition potentials, a N_2 saturated acetonitrile electrolyte was employed because it exhibits a large solvent window. The anaerobic conditions prevent the formation of oxides, while the large solvent window minimizes parasitic side reactions such as solvent degradation.[37] In particular, we chose an electrolyte consisting of 100 mM tetrabutylammonium hexafluorophosphate (TBA-PF_6) electrolyte and 10 mM tetrakis-acetonitrile Cu hexafluorophosphate as the Cu source. This was to ensure solubility in acetonitrile and to limit strong coordinating interactions between the electrode and the electrolyte.

Constant potential deposition (CPD) of Cu on to 1 cm^2 Ti electrodes at different deposition potentials led to the depositions of grains with only a slight variability in size and large differences in morphology. Based on the linear sweep voltammogram of Cu deposition,

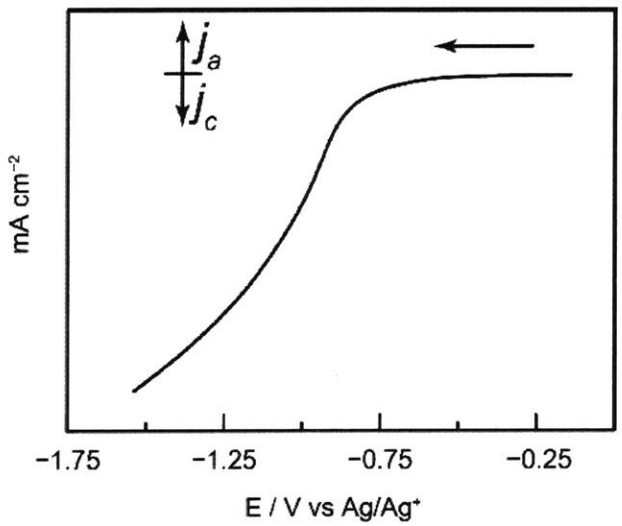

Figure 5.6. Linear sweep voltammogram of Cu deposition in acetonitrile solution showing the onset of deposition.

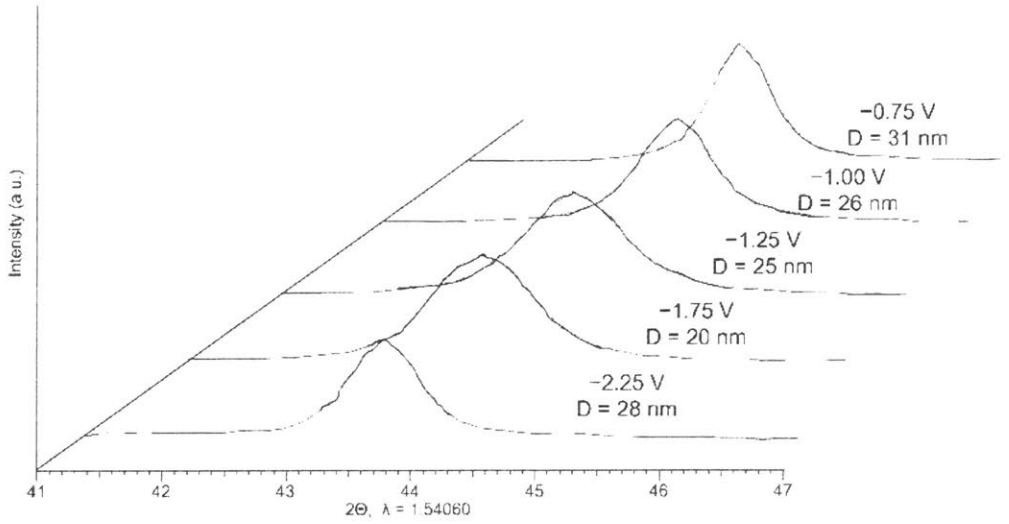

Figure 5.7. XRD patterns representing the [111] reflection of Cu deposited in acetonitrile electrolyte at different potentials with corresponding grain sizes calculated by the Scherrer equation.

the deposition potentials were selected incrementally from deposition onset to near the solvent degradation region (Figure 5.). The largest grains were obtained at potentials closer to onset (−0.75 V vs Ag/Ag^+) as determined by the full-width-half-max (FWHM) Scherrer analysis of the Cu [111] X-ray diffraction (XRD) pattern, while deposition at more reducing potentials (−1.75 V vs Ag/Ag^+) resulted in slightly smaller grains (Figure 5.). We rationalize the potential dependence of grain sizes through the larger potential requirements for nucleation over growth, which stems from increasing lattice mismatch defects during nucleation.[31–33] Thus higher deposition potentials will favor a greater frequency of nucleation events over growth, leading to smaller crystallites. However, further increasing the applied potential to beyond −1.75 V vs

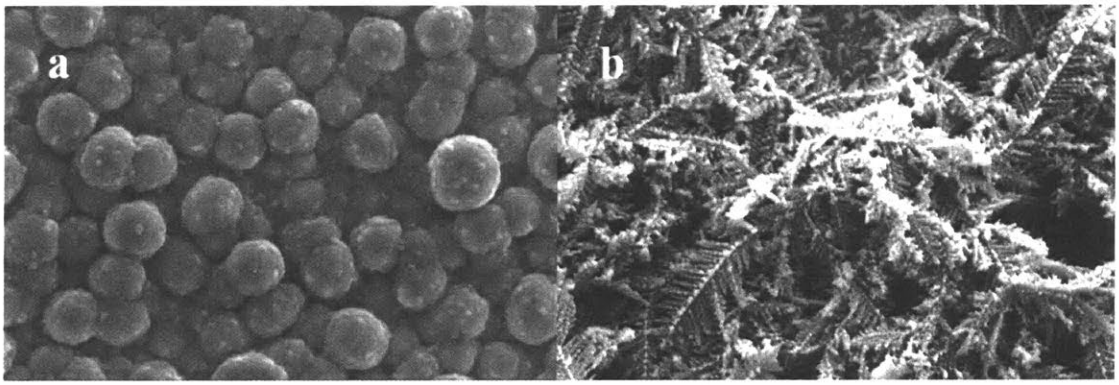

Figure 5.8. SEM micrograph of Cu CPD at a) -1.25 V, and b) -1.75 V.

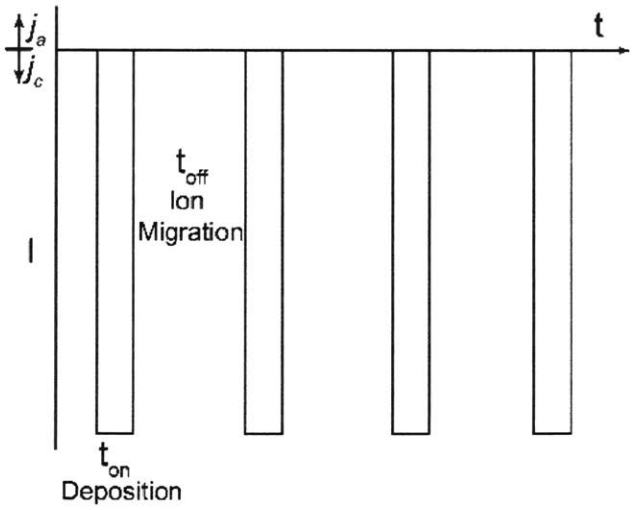

Figure 5.9. Pulsed electrodeposition scheme.

Ag/Ag^+ resulted in an enlargement of grains, perhaps due to excessive local depletion of Cu ions, leading to an inhomogeneous, pocketed distribution of Cu^+ near the electrode and around the electrochemical double layer. This has been known to induce grain growth at areas of high metal ion concentration.[31,32] Moreover, the morphology of the deposited grains become increasingly dendritic with applied potential, which is characteristic of Cu depositions at high potential and severe local depletion of Cu ion concentration[38] (Figure 5.). Due to the small range of accessible grain sizes and significant changes in morphology, CPD was deemed unfit to systematically tune grain sizes.

To address the limitations of CPD, we developed a specialized set of galvanostatic

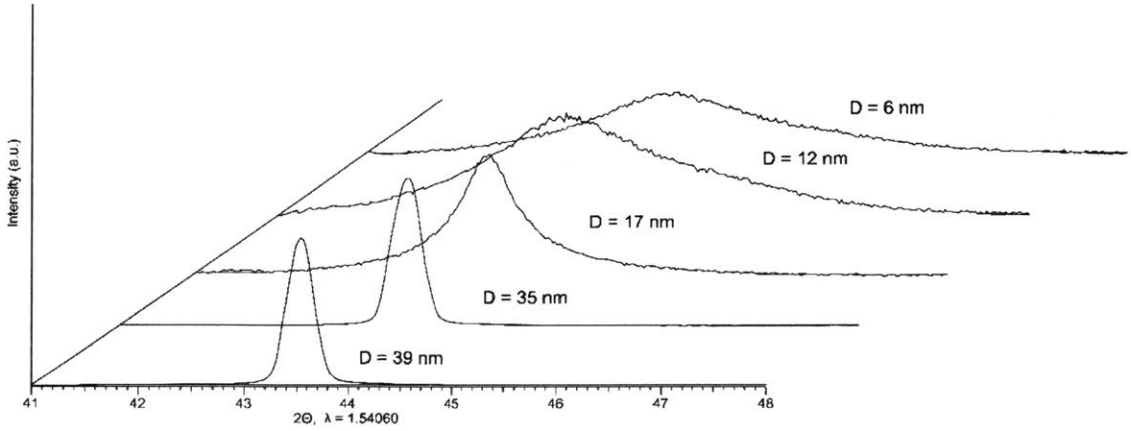

Figure 5.10. XRD patterns of grain size controlled Cu by PED.

pulsed electrodeposition (PED) sequences that operate by alternating and repeating a short period of high cathodic current (t_{on}) and a period of lesser, positive or no current (t_{off}) (Figure 5.). This allows high potential depositions favorable for nucleation while simultaneously avoiding the formation of concentrated Cu ion pockets that lead to grain growth. PED of Cu was carried out using a room temperature aqueous bath at pH 1 containing 100 mM $CuSO_4 \cdot 5H_2O$, 400 mM $(NH_4)_2SO_4$ as electrolyte, and differing concentrations of an inhibiting additive, citric acid.[32,33]

Modifying the pulse sequence and citrate concentration, we successfully synthesized size controlled Cu grains from 6 ~ 40 nm, with decreasing GB densities on Ti electrodes (Figure 5. and Figure 5.). scanning electron microscopy (SEM) reveals that the films consist of nanocrystalline grains composing larger aggregates.

By modifying the PED timing sequence through the decrease of toff from 99 ms to 5

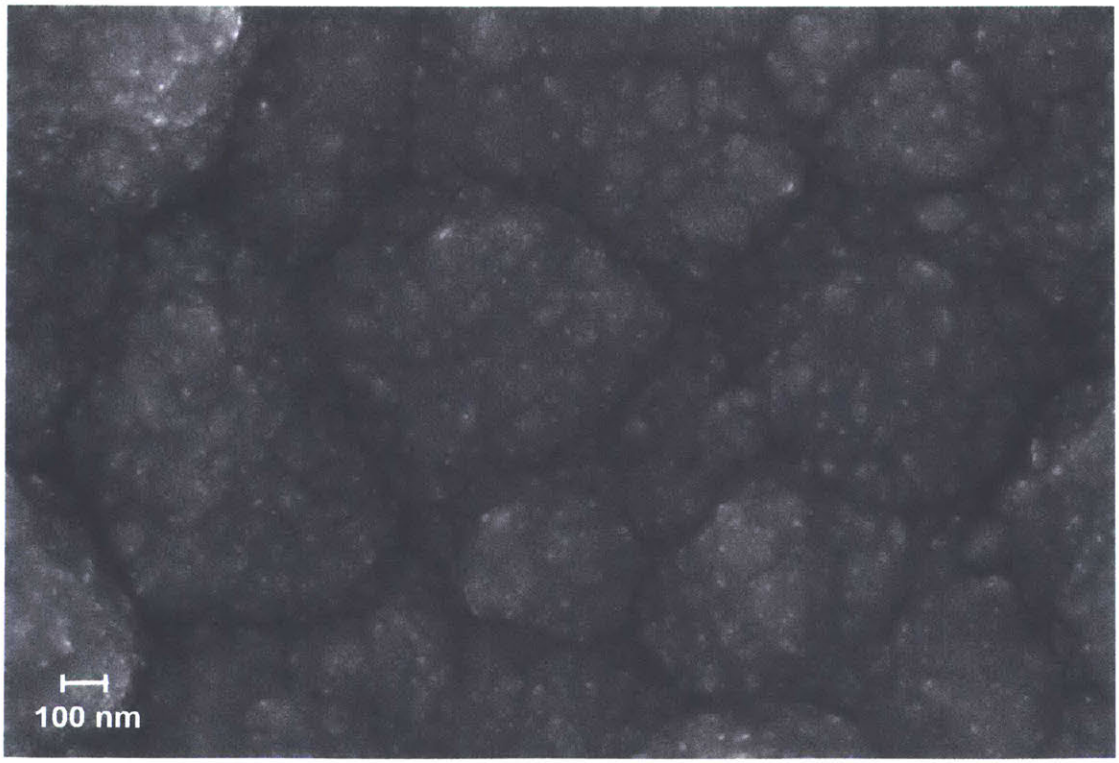

Figure 5.11. SEM micrograph of 6 nm grain Cu.

ms at fixed current density and bath conditions, we observed increased grain sizes by XRD (Table 5.). Modification of PED timing allows for grain size control by applying a very high η

t_{off} (ms)	FWHM (°2Θ)	Average grain diameter (nm)
99	0.33	35
24	0.31	38
5	0.25	46

Table 5.1. PED Cu grain size dependence with decreasing t_{off} at fixed 12.5 mA cm^{-2} average current density and t_{on} = 1 ms.

for Cu deposition during the ton period, providing enough driving force for rapid nucleation of Cu at the surface. Returning to open circuit (0 net current) following the short cathodic pulse allows the diffusion layer to equilibriate ion concentration to bulk solution levels, preventing the onset of water reduction and local ion concentration gradients. Prolonged toff also allows for growth-inhibiting citrate ions to repopulate the surface after electrostatic repulsion during polarization.[31–33] In contrast, CPD at such potentials would lead to the rapid depletion of Cu^{2+} ions in the diffusion layer and the electrode surface, leading to significant water reduction and grain growth.

Citric acid concentration (M)	FWHM (°2Θ)	Average grain diameter (nm)
0	0.32	36
0.03	0.95	12
0.3	1.61	7

Table 5.2. PED Cu grain size dependence on increasing citric acid concentration at fixed 12 mA cm^{-2} average current density with t_{on} = 1 ms and t_{off} = 49 ms.

Cu grain sizes also decreased as a function of citric acid inhibitor concentration from 0 to 0.3 M (Table 5.). This can be rationalized by citrate acting as a surface inhibitor, reversibly physisorbing to the Cu surface to physically prevent grain growth.[33] Additionally, Cu^{2+} complex formation in an acidic electrolyte ($[CuH_2C_6H_5O_7]^+$, $K_{dissociation} = 1.0 \times 10^{-6}$) can reduce

the concentration of Cu^{2+} ions during deposition, leading to a lower likelihood of grain growth at the surface while simultaneously having enough driving force to favor nucleation.[33] Thus by increasing the concentration of citric acid, we observe decreased grain sizes.

5.2.5 CO_2 reduction on grain boundary rich electrocatalysts

The electrocatalytic CO_2 reduction activity of the Cu samples at different grain sizes and grain boundary densities were tested in the low η range from −0.3 to −0.5 V vs. RHE over 0.1 V intervals in 0.1 M $KHCO_3$, where CO and formate were observed in OD-Cu.[23] Using a gas chromatograph (GC) in line with the electrochemical cell, the evolution of gaseous products was measured over 20 minute intervals at the different potentials. The electrodes were held at each potential for 1 hour against a [Ag/AgCl : 1 M KNO_3] reference in a 3-electrode cell with a Selemion anion exchange membrane separating the working and counter compartments. CO_2 was continuously sparged into solution.

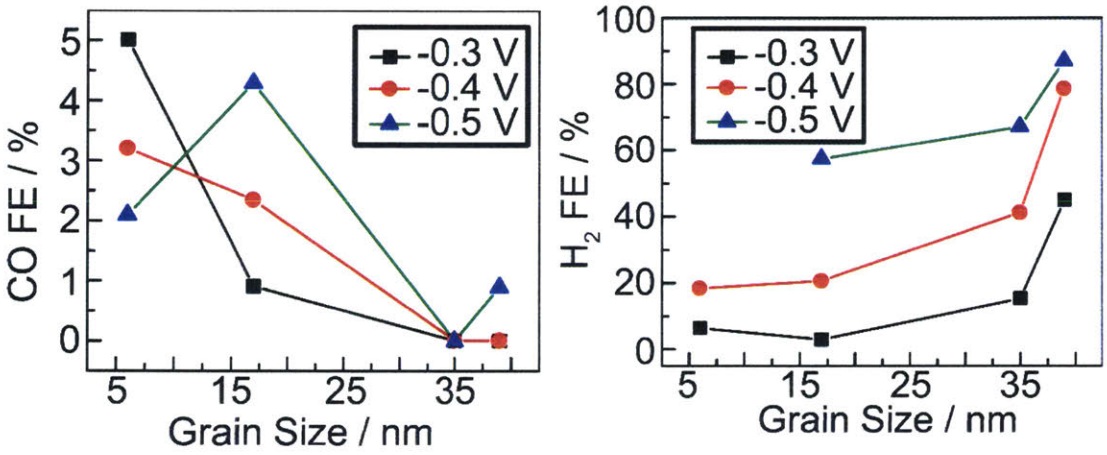

Figure 5.12. Faradaic efficiencies of CO and H_2 evolution at −0.3 to −0.5 V vs RHE as a function of grain size. Experiments were performed using a Ag/AgCl : 1 M KNO_3 reference electrode.

In this potential range, GC analysis reveals a slight degree of CO production with decreasing grain sizes, whereas the larger grain samples produce a significantly higher fraction of H_2 (Figure 5.). NMR analysis of the products indicates some minor production of formate. The observation of a large amount of solution phase product FE (~90% for 6 nm grain size Cu at −0.3 V) is incredibly high for CO_2 reduction selectivity on Cu. More careful analysis of this result revealed that the missing FE was likely to be coming from NO_3^- reduction, which appears to have leaked from the reference electrode solution. While smaller grains and larger grain

boundary density Cu catalysts appear to be more selective for NO_3^- reduction in this potential range, the usage of more robust Ag/AgCl : KCl (Edaq) electrodes for CO_2 reduction revealed about 5 % CO FE and 90 % H_2 FE from 6 nm grain Cu catalysts.

While attempts to make highly grain boundary rich Cu catalysts by direct electrodeposition were successful, the poor CO_2 reduction activity suggests that high grain boundary density alone does not equate to better performance. This is may suggest that certain types of grain boundaries, for example those generated by oxide-derivation, may be more relevant to tuning CO adsorption energies. In particular, temperature programmed desorption of CO experiments on these grain boundary enriched electrodes may reveal more information as to the nature of these grain boundaries.

5.3 Concluding remarks

Cu catalysts are attractive candidates for electrochemical CO_2 reduction due to the wide range of possible observed products, including CO, CH_4, C_2H_4, and other hydrocarbons. However, little is known about the mechanistic pathways leading to various product selectivity. To understand the selectivity of CO_2 reduction, a detailed kinetic study was performed in ethanolic electrolyte at −35 °C, where the impact of CO, a key intermediate to CH_4 and C_2H_4 production, can be studied without reaching diffusion limitations like in aqueous electrolytes. Kinetic analysis indicates that a LH pathway, whereby two surface adsorbed intermediates react, gates both the formation of CH_4 and C_2H_4. For CH_4 in particular, the C-H bond formation between a CO_{ads} and an H_{ads} appears to be rate limiting. This necessitates the need to have the appropriate balance of surface CO_{ads} and H_{ads} in order to have facile CH_4 formation. As such, a high CO partial pressure in the reaction cell would inhibit the formation and selectivity for CH_4. Likewise, as H_2 evolution is gated by H_{ads} reacting on surface sites, a high p_{CO} suppresses H_2 evolution activity. Meanwhile, the data suggest that the formation of C_2H_4 also proceeds through a LH step, where two CO_{ads} form C-C bonds mediated by electron transfer. However, there is little dependence on p_{CO} on the rate of C_2H_4 formation, indicating that the sites responsible for C_2H_4 formation are saturated in the probed range. Therefore, increasing C_2H_4 selectivity over H_2 and CH_4 selectivity may be accomplished by increasing the amount of surface sites that strongly bind CO_{ads} over H_{ads}.

Using this mechanistic understanding and literature reports on Cu grain boundary sites with high CO_{ads} energies leading to increased hydrocarbon selectivity, we synthesized Cu electrodes with high grain boundary density. The small Cu crystallite size and high grain boundary density were achieved by using pulsed electrodeposition of Cu from copper citrate electrolytes, maximizing the amount of Cu nucleation over Cu growth events. Although Cu

electrodes were synthesized with tunable and high grain boundary density, these electrodes did not achieve selective CO_2 reduction activity, suggesting that merely an increased number of grain boundaries is insufficient, but that the type of boundaries may also be extremely important.

5.4 Experimental methods

Materials. Phosphoric acid (≥85 wt.%, ≥99.999%, Sigma-Aldrich), LiTFSI (99.95%, Sigma-Aldrich), Ethanol (200 proof, anhydrous, ≥ 99.5%, Sigma-Aldrich), CO (Research Grade, Airgas), Argon (Research Grade, Airgas), HCl (36.5 – 38%, EMD Millipore), HNO_3 (68 - 70%, VWR), stabilized H_2O_2 (35% w/w, VWR/BDH), H_2SO_4 (95 – 98%, EMD Millipore) were used without purification. All electrolyte components were stored in a glovebox under inert atmosphere. In all cases, ultrapure water was used (Millipore Type 1, 18.2 MΩ cm). Pt mesh counter electrodes were obtained from Alfa Aesar (Platinum gauze, 52 mesh woven from 0.1 mm dia. wire, 99.9% metals basis). They were washed by brief dipping in aqua regia solutions (2/3 HCl, 1/3 HNO_3), followed by copious rinsing with ultrapure water and drying in an oven at 105 °C.

Nafion 117 (Sigma-Aldrich) was treated as follows. The Nafion sheet was cut into 3.2 x 3.2 cm^2 squares. Subsequently, the pieces were transferred into a beaker and washed copiously with ultrapure water. The membranes were then boiled in 3% (v/v) H_2O_2/water for 10 minutes to remove organic impurities, followed by copious washing with ultrapure water and boiling in water for 10 minutes. After this, the membranes were boiled in 0.5 M sulfuric acid for 10 minutes, and washed again with copious amounts of ultrapure water. Lastly, the films were boiled for 45 minutes in DI water, followed by copious washing with ultrapure water. The films were then dried in an oven for 48 hours at 105 °C, and stored at the same temperature.

All electrochemical tests were carried out using a Gamry Reference 600 potentiostat.

Sample preparation. Cu foil (99.9999%) was obtained from Goodfellow and cut into flag-shaped pieces of roughly 2 cm^2, which had a thin slice extending from them, used for electrical connection. A picture was taken of the sample and the surface area subsequently

determined using the sofware ImageJ. Before each test, the Cu piece was immersed in ultrapure phosphoric acid and electropolished for 2 min at 160 mA cm^{-2} using a similar Cu foil as the counter electrode. After copious rinsing with ultrapure H_2O (MilliQ, 18.2 MOhm), the sheet was dried in a stream of air and stored in air prior to use.

Electrochemical testing. Electrochemical tests were carried out in a gastight two-compartment H-cell in a three-electrode configuration. All cell components were cleaned by immersion in freshly prepared Aqua Regia (2/3 HCl, 1/3 HNO_3) for at least 1 h, followed by copious rinsing with ultrapure water and drying at 140 °C. The anode and cathode compartment were separated by a dry piece of Nafion 117 membrane. The Cu piece was attached to a Ti wire (99.99%, 1 mm diameter, Alfa Aesar) protruding from a septum (Suba-Seal, Chemglass Life Sciences) and inserted with the Cu sheet oriented parallel to the axis of the cell. A Pt mesh (99.997%, Alfa Aesar), heated to white glow by a butane torch before each test, was used as counter electrode. The reference electrode was Ag/AgCl (3 M NaCl) (RE-4, BAS Inc.), placed behind a double-junction filled with the same electrolyte as the cell. Potentials are reported with respect to this reference electrode. All electrolyte solutions were prepared in a N_2-filled glovebox with an internal atmosphere maintained at less than 10 ppm O_2 and less than 4 ppm H_2O. After assembly, the test cell was transferred into the glovebox and filled with electrolyte. The cell was subsequently closed, taken out of the glovebox and attached to the analysis setup.

During experiments, the catholyte, which amounted to ca. 20 mL, was continuously stirred at 500 rpm using a magnetic stirbar. Two mass flow controllers (Aalborg DFC, 0 – 50 mLn min^{-1}) provided a constant flow of 30 mL min^{-1} of substrate gas, consisting of variable ratios of CO and Ar. After sparging through the electrolyte, the effluent from the cell headspace was directed through a cold trap maintained at -78 ℃ by immersion in a dry ice – acetonitrile cold bath. Part of the gas was subsequently passed into a gas chromatograph (SRI Instruments,

Multi-Gas Analyzer #3) and analyzed as described below, while the other part was purged through a backpressure regulator (Alicat Scientific) providing a constant overpressure of 0.1 psi in the test cell. The entire electrochemical cell was immersed into an ethanol (200 proof, anhydrous, Koptec) cold bath which was stirred at 500 rpm and maintained at −35 ℃ using a Thermo EK-1 immersion chiller. The temperature of both the bath and the interior of the cell were measured using low noise miniature thermocouples (Omega Engineering).

Measurement sequence. The gas composition of the CO-containing reactant stream was controlled by software (Aalborg DFC communication utility). CO-Ar mixtures containing 10, 25, 50, 75 and 100% CO were sequentially flown into the cell. After stepping to a new gas composition, the system was allowed to equilibrate for 34 minutes. Subsequently electrochemical tests were carried out in galvanostatic mode between −0.19 and −1.90 mA cm^{-2} in 4 or 6 logarithmically spaced steps, which each step lasting 20 minutes. Evolved products were quantified at the end of each polarization step by injection of the effluent stream into the in-line GC.

Product quantification. Periodic analysis of the effluent gas by gas chromatography allowed for the quantification of reaction products. The chromatograph employed series-connected Molsieve 13x and Hayesep D columns and was equipped with a thermal conductivity detector and a flame ionization detector. It was calibrated using a NIST traceable gas standard (Airgas). GC traces were recorded every 20 minutes. Taking into account the constant gas flow rate of 30 mL min^{-1}, the partial current density for each product was calculated using the following formula:

$$j_i = c_i * n_i * F * \dot{V}_{gas} * \frac{p}{R*T} * \frac{1}{A}$$

with C_i denoting the GC detected product concentration in ppm, n_i denoting the electron

stoichiometry for product i, F being Faraday's constant (96485 C mol^{-1}), $\dot{V}_{gas}$ corresponding to the substrate gas flow rate (30 mL min^{-1}), p denoting the pressure in the cell (14.8 psi) and A denoting the sample surface area. To calculate faradaic efficiencies, the partial current densities for each product were divided by the applied current density.

The observed H_2, CH_4 and C_2H_4 did not account for the full Faradaic balance of the reaction and we attribute the remainder to the production of liquid products. Previous reports in water found the production of predominantly EtOH and smaller amounts of n-PrOH, MeCHO and EtCHO.[12] Indeed, the formation rate of the solution-phase products scaled uniformly with the rate of ethylene production, and therefore has no impact on the mechanistic conclusions reached regarding H_2, CH_4 and C_2H_4 production.

The recorded chronopotentiograms for each applied current were averaged between 3.3 and 20 minutes of the run and this average value was taken as the steady-state potential in all further analysis. Before each partial pressure segment, the ohmic loss between the working and reference electrode was determined using AC-Impedance spectroscopy at −1.5 V vs. Ag/AgCl (3 M NaCl) between 100 kHz and 50 Hz with an amplitude of 10 mV. Ohmic loss values were determined at minimum phase angle and were corrected for during data workup. At the end of each measurement series, a spatula tip of ferrocene was added to the electrolyte and a cyclic voltammogram recorded between 0 and +0.7 V vs. Ag/AgCl (3 M NaCl) at 50 mV sec^{-1} using a glassy carbon electrode (CH Instruments). The ferrocene half wave potential served as potential reference. In all cases, the Fc^+/Fc half wave potential was observed between 0.42 and 0.44 V vs the Ag/AgCl reference electrode. All current densities are reported relative to the geometric surface area of the sample.

X-ray diffraction (XRD). XRD patterns were collected for flat, electrodeposited Cu films calculate the average grain size. A Bruker D8 Advance diffractometer with a Cu source

(λ = 1.504 Å) was used. The Scherrer equation[39] with a shape factor of K = 0.94 (Scherrer constant) was used to determine the average grain size in the electrodeposited Cu at the [111] reflection (43.4°).

Scherrer Equation: $D = \frac{K\lambda}{\Delta(2\theta)\cos(\theta[111])}$

Legend:

D = average diameter (nm)

K = Scherrer constant

λ = X-ray wavelength (nm)

$\Delta(2\theta)$ = full width at half max intensity value of [111] reflection peak in rads

$\theta[111]$ = peak center of [111] refection.

5.5 References

(1) Hori, Y. In Handbook of Fuel Cells; John Wiley & Sons, Ltd, 2010.

(2) Yoon, Y.; Hall, A. S.; Surendranath, Y. Angew. Chemie Int. Ed. **2016**, 55 (49), 15282.

(3) Yang, K. D.; Ko, W. R.; Lee, J. H.; Kim, S. J.; Lee, H.; Lee, M. H.; Nam, K. T. Angew. Chemie Int. Ed. **2017**, 56 (3), 796.

(4) Hall, A. S.; Yoon, Y.; Wuttig, A.; Surendranath, Y. J. Am. Chem. Soc. **2015**, 137 (47), 14834.

(5) Li, C. W.; Ciston, J.; Kanan, M. W. Nature **2014**, 508 (7497), 504.

(6) Gattrell, M.; Gupta, N.; Co, A. J. Electroanal. Chem. **2006**, 594 (1), 1.

(7) Kortlever, R.; Shen, J.; Schouten, K. J. P.; Calle-Vallejo, F.; Koper, M. T. M. J. Phys. Chem. Lett. **2015**, 6 (20), 4073.

(8) Davis, M. E. D. and R. J. McGraw-Hill Higher Education: New York, NY, 2003; p 384.

(9) Cheng, T.; Xiao, H.; Goddard, W. A. Proc. Natl. Acad. Sci. **2017**, 114 (8), 1795.

(10) In Solubility Data Series - Carbon Monoxide; Cargill, R. W., Ed.; IUPAC Solubility Data Series; Pergamon: Amsterdam, 1990; p ii.

(11) Bockris, J. O.; Nagy, Z. J. Chem. Educ. **1973**, 50 (12), 839.

(12) Hori, Y.; Takahashi, R.; Yoshinami, Y.; Murata, A. J. Phys. Chem. B **1997**, 101 (36), 7075.

(13) Fletcher, S. **2009**, 537.

(14) Hori, Y.; Murata, A.; Yoshinami, Y. J. Chem. Soc. Faraday Trans. **1991**, 87 (1), 125.

(15) Schouten, K. J. P.; Qin, Z.; Gallent, E. P.; Koper, M. T. M. J. Am. Chem. Soc. **2012**, 134 (24), 9864.

(16) Schouten, K. J. P.; Pérez Gallent, E.; Koper, M. T. M. J. Electroanal. Chem. **2014**, 716, 53.

(17) Vollmer, S.; Witte, G.; Wöll, C. Catal. Letters **2001**, 77 (1), 97.

(18) Hammer, B.; Nørskov, J. K. In Advances in Catalysis; 2000; Vol. 45, pp 71–129.

(19) Chen, Y.; Li, C. W.; Kanan, M. W. J. Am. Chem. Soc. **2012**, 134 (49), 19969.

(20) Hori, Y.; Kikuchi, K.; Suzuki, S. Chemistry Letters. Chemical Society of Japan 1985, pp 1695–1698.

(21) Sen, S.; Liu, D.; Palmore, G. T. R. ACS Catal. **2014**, 4 (9), 3091.

(22) Kas, R.; Kortlever, R.; Milbrat, A.; Koper, M. T. M.; Mul, G.; Baltrusaitis, J. Phys. Chem. Chem. Phys. **2014**, 16 (24), 12194.

(23) Li, C. W.; Kanan, M. W. J. Am. Chem. Soc. **2012**, 134 (17), 7231.

(24) Chen, C. S.; Handoko, A. D.; Wan, J. H.; Ma, L.; Ren, D.; Yeo, B. S. Catal. Sci. Technol.

2015, 5, 161.

(25) Mariano, R. G.; McKelvey, K.; White, H. S.; Kanan, M. W. Science (80-.). **2017**, 358 (6367), 1187.

(26) Feng, X.; Jiang, K.; Fan, S.; Kanan, M. W. ACS Cent. Sci. **2016**, 2 (3), 169.

(27) Gottstein, G.; Shvindlerman, L. S. Grain Boundary Migration in Metals; 1999.

(28) Bober, D. B.; Kumar, M.; Rupert, T. J. ACTA Mater. **2015**, 86, 1.

(29) Palumbo, G.; Lehockey, E. M.; Lin, P. JOM **1998**, 50 (2), 40.

(30) Randle, V.; Rohrer, G. S.; Miller, H. M.; Coleman, M.; Owen, G. T. Acta Mater. **2008**, 56, 2363.

(31) Chandrasekar, M. S.; Pushpavanam, M. Electrochim. Acta **2008**, 53 (8), 3313.

(32) Bicelli, L.; Bozzini, B.; Mele, C.; D'Urzo, L. Int. J. Electrochem. Sci **2008**, 3, 356.

(33) Natter, H.; Hempelmann, R. J. Phys. Chem. **1996**, 100 (50), 19525.

(34) Hung, D.; Liu, Z.; Shah, N.; Hao, Y.; Searson, P. C. J. Phys. Chem. C **2007**, 111, 3308.

(35) Thomson, C. B.; Randle, V. J. Mater. Sci. **1997**, 32, 1909.

(36) Yang, H. J.; He, S. Y.; Tuan, H. Y. Langmuir **2014**, 30, 602.

(37) Grujicic, D.; Pesic, B. Electrochim. Acta **2002**, 47 (18), 2901.

(38) Shao, W.; Zangari, G. J. Phys. Chem. C **2009**, 113, 10097.

(39) Langford, J. I.; Wilson, A. J. C. J. Appl. Crystallogr. **1978**, 11 (2), 102.

Acknowledgements

I would like to acknowledge my supervisor, Yogesh Surendranath, for giving me the opportunity to learn about electrochemistry and science as a whole in a rigorous yet supportive environment. His passion for chemistry and communicating science is contagious, and truly inspiring. It has been a great honor and challenge to work with him on the ground floor of establishing the Surendranath lab, and to watch the lab grow.

I would also like to thank past and present members of my thesis committee, Professor Mircea Dincă, Professor Daniel Nocera, and Professor Stephen Lippard for helpful discussions and support throughout this effort. It has also been a privilege to take classes taught by these professors, as well as with Professor Richard Schrock and Professor Christopher Cummins, who have passionately shared their perspectives on inorganic chemistry with students.

I have also learned so much about chemistry and about life in general from the excellent post-doctoral associates who have been a part of the Surendranath lab. In particular, I would like to thank Dr. Joseph Falkowski for being a great mentor and leader in our nascent lab, and continuing to be a great friend. Professor A. Shoji Hall has also been a great collaborator, mentor, and friend. His positivity and approach to research has been personally inspiring, and I strongly approve of his musical and coffee taste. Dr. Sahr Khan has also been a great collaborator and friend, who has the ability to command the room with her mere presence. Dr. Marcel Schreier has also been a great collaborator and friend. His drive, scientific insight, and collaborative spirit is truly wonderful, and I am certain that he will do well in academia and other pursuits.

Of course, from a day-to-day perspective, graduate school was made much more interesting due to some amazing lab mates who I am honored to call friends and colleagues.

Megan Jackson and Sterling Chu in particular, have been great companions throughout this process, as we share so many experiences. Megan is a great collaborator with a big and inspiring heart for science. Sterling is truly a stable genius, whose open mind and outlook are admirable. Anna Wuttig, whom I share many scientific achievements with, has also been a key starting member and a force of dedication in the Surendranath lab, and has been a joy to work and interact with on a daily basis. I would also like to thank Corey Kaminsky for being a gracious organizer and participant in lab activities. Additionally, I would like to thank the support of all the other past and present members of the Surendranath lab, who have brought valuable scientific contributions and have made been great to work and interact with on a daily basis.

Also, the scientists who operate and maintain the instrument facilities at MIT have been invaluable, and I would like to thank them for their expertise and openness to help. In particular, Dr. Charles Settens, Dr. Libby Shaw, and Dr. Yong Yang at the CMSE have been great resources. Kurt Broderick of the MTL has also been a joy to work with, and has been invaluable in many materials syntheses. Much of my work would not have been possible without the custom glassware provided by Ed Mitchell, whose expertise, skill, and flexibility despite multiple last minute requests, is truly admirable.